

UNIVERSITY OF NAPLES “FEDERICO II”



Department of Chemical, Materials and Industrial Process Engineering

PhD Thesis in

Industrial Product and Process Engineering

CHARACTERIZATION OF ELECTRIFIED WATER SPRAYS

Supervisor

Prof. Amedeo Lancia

Prof. Francesco Di Natale

Candidate

Lucia Manna

XXXI Cycle-2018

Summary

List of Figures.....	I
List of Tables.....	III
Nomenclature.....	IV
Abstract.....	VIII
Chapter 1. Introduction.....	1
1.1 Aim of the work.....	1
1.2 General physics.....	2
1.3 Charging Mechanism.....	7
1.3.1 High flow rate electrified spray.....	8
1.3.2 Low flow rate electrified spray.....	10
1.4 References.....	16
Chapter 2. Critical Literature Review.....	20
2.1 Atomization models.....	20
2.2 LISA model.....	21
2.2.1 Mathematical analysis.....	21
2.2.2 Inviscid liquid sheet.....	24
2.2.3 Viscous liquid sheet.....	27
2.2.4 Primary atomization.....	28
2.2.5 Secondary atomization.....	32
2.3 Theory of Electrohydrodynamic.....	34
2.4 Simplified model of induction charging.....	37
2.5 Literature review.....	41
2.6 References.....	45
Chapter 3. Induction Charging and Breakup of Water Sprays.....	50
3.1 Introduction.....	51
3.2 Material and methods.....	53
3.3 Results.....	55
3.4 Discussion.....	56
3.5 Summary.....	62
3.6 References.....	62
Chapter 4. Primary atomization of electrified water sprays.....	64
4.1 Introduction.....	65
4.2 Materials and methods.....	67
4.3 Results and discussion.....	69
4.4 Summary.....	76

4.5	References	77
Chapter 5.	Electrohydrodynamic Atomization of water in the simple-jet mode with whipping breakup	80
5.1	Introduction	81
5.2	Materials and Methods	82
5.2.1	Materials	82
5.2.2	Experimental methods	83
5.2.3	Imaging data post-processing.....	85
5.3	Results and discussion	86
5.3.1	Experimental results	86
5.3.2	Influence of whipping breakup on droplet's population.....	89
5.3.3	Influence of whipping breakup on liquid jet stresses.....	90
5.3.4	Transition of the simple-jet mode from the varicose breakup to the whipping breakup.....	91
5.3.5	Improved spray properties with the whipping breakup mechanism	92
5.4	Summary.....	93
5.5	References	94
Chapter 6.	Secondary Atomization of Electrified Water Sprays	96
6.1	Introduction	97
6.2	Materials and Methods	97
6.2.1	Experimental methods	98
6.3	Experimental results.....	101
6.4	Summary.....	106
6.5	References	107
Chapter 7.	Conclusion	110
	List of publications.....	113
	Conference Proceedings.....	114

List of Figures

Figure 1-1 Relationship between cone angle and nozzle geometry [16]	5
Figure 1-2- Schematic representation of charging mechanisms. A) corona charging; B) contact charging and C) induction charging.....	7
Figure 1-3 Electric circuit as schematization of induction charging system.....	9
Figure 1-4- Electrical circuit with a toroidal electrode and a pressure hollow cone nozzle [I]	9
Figure 1-5- Inner Wetting (left) and outer wetting (right) of the nozzle [44]	11
Figure 1-6- Electro spray modes. A) enhanced dripping mode. B) microdripping. C) spindle mode [33]	12
Figure 1-7- Cone jet mode with varicose breakup (left) and whipping breakup (right) [47]	13
Figure 1-8 Simple jet mode with varicose breakup (A), whipping breakup (B) and ramified breakup (C). The picture C) was taken from [49].....	14
Figure 1-9- Electro spray mode map as function of electric potential and liquid flow rate [25]	15
Figure 2-1 One dimensional representation of symmetric(a) and antisymmetric instabilities (b)	22
Figure 2-2- Varicose wave (left) and sinusoidal wave (right) [3].....	22
Figure 2-3-Critical Weber number for sinuous long and short waves	25
Figure 2-4- Sinuous and varicose waves for inviscid liquid sheet at Weber number = 0.5.....	26
Figure 2-5-- Sinuous and varicose waves for inviscid liquid sheet s at Weber number = 5	27
Figure 2-6--Sinuous long and short waves for viscous liquid sheet at We= 5	28
Figure 2-7- Sinuous long and short waves for viscous liquid sheet at We= 0.5	28
Figure 2-8- Wavy sheet scheme and coordinate system.....	29
Figure 2-9-Lisa model of sheet primary atomization [61]	31
Figure 2-10- Different secondary atomization breakup modes at different Weber numbers [63]	33
Figure 2-11- Secondary atomization modes as function of Weber and Ohnesorge numbers [63]	33
Figure 2-12- Representation of induction charging system as an electrical circuit. Left: model, right: experimental setup.....	38
Figure 2-13-Leonardo Da Vinci scheme of liquid jet breakup [70].....	42
Figure 3-1- Experimental Rig. 1: water tank, 2: pump, 3: inverter, 4: flow meter, 5: pressure gauge, 6: HV power supply, 7: droplet charge unit (DCU), 8: Faraday pail, 9: water collector, 10: electrometer, 11: computer to elaborate experimental results. The red line indicates the high-tension connection, while the blue line is the liquid flow path.	53
Figure 3-2- Breakup length and spray angle. In the pictures the nozzle 216.364 at P=3 bar is reported at 0 kV (left) and at V= 10 kV (right). The dotted line divides the primary and secondary atomization zones.....	54
Figure 3-3- Breakup Length L_b (left), droplets current I_{drop} and D-CMR (right) as function of applied voltages at different pressures.	55
Figure 3-4- Comparison of breakup length ((left) and Droplet charge to mass ratio/droplets current (right) at different voltages for nozzles LC Nozzle.....	55
Figure 3-5- Breakup mechanism for tested nozzle.....	57
Figure 3-6 Electrical surface tension as function of applied electric potentials at different liquid pressure for the nozzle SS-BD5.	58
Figure 3-7- Comparison of experimental and theoretical Droplet Charge to Mass Ratio for SS-BD5.	61
Figure 3-8- Comparison of experimental and theoretical Droplet Charge to Mass Ratio for LC-nozzles.	61
Figure 4-1- Liquid jet breakup mechanism for the nozzle BD5 at P=3 bar [32].	68
Figure 4-2- Breakup length as a function of the theoretical prediction for all tested nozzles.....	70
Figure 4-3- Experimental breakup length (left graphs) and spray angle (right graphs) as a function of charging potential at different pressures for BD5, BD8 and BD10.....	72
Figure 4-4-Breakup length variation trend with voltage and global curve regression.....	73

Figure 4-5-. Wave profile on liquid surface for nozzle BD5 at P= 2 bar and rising charging potential V= 0 kV (a), V= 4 kV (b), V= 8 kV (c), V= 12 kV (d), V=16 kV (e) and V=20 kV (f).....	75
Figure 5-1- Experimental set-up 1: Electrospray unit; 2: High Voltage (HV) power supply; 3: Syringe pump; 4: Back light; 5: High-Speed Camera; 6: Water tank. Solid line: water; dash dot-line: Electric circuit	83
Figure 5-2-1) Jet parameters as jet diameter and breakup length; 2) major and minor axes of a droplet	85
Figure 5-3- Sampling of droplets' images for nozzle N2 at We=7.11 and different Bond numbers	86
Figure 5-4- Superimposition of 100 frames (A) and 500 frames (B) at We=7.11 and B= 5295.8 for N1.....	87
Figure 5-5- Probability Density Functions for N2 at We= 7.11 and at six different Bond numbers.....	87
Figure 5-6- Cumulative Density Functions (CDFs) at different Bond numbers and at We= 7.11 for N1.....	88
Figure 5-7- Electric current versus Bond number for nozzle N1, N2 and N3.	89
Figure 5-8- Diameter d_{50} versus Bond number for the three nozzles at different Weber numbers. Whipping line for We=3.16: Dash-dot-dot line; Whipping line for We=4.93: dot line: Whipping line for We=7.11: dot-dash line.....	89
Figure 5-9- Ratio between the electrical and surface tension stresses, R, for different Weber and Bond numbers for the three nozzles N1, N2 and N3. Whipping line for We=3.16: Dash-dot-dot line; Whipping line for We=4.93: dot line: Whipping line for We=7.11: dot-dash line.....	90
Figure 5-10- Liquid jet whipping breakup (left) and corona fluorescence (right) for N2 and We3.....	91
Figure 5-11- Number of droplets produced per second n, interface area of droplets A_i , circularity C, at different Bond and Weber numbers. Whipping line for We1: Dash-dot-dot line; Whipping line for We2: dot line: Whipping line for We3: dot-dash line.	92
Figure 6-1- Atomization process of an hydraulic water spray (left) and secondary atomization droplets (right)	98
Figure 6-2. Representation of liquid cone parameters as cone radius, r, breakup length, L_b , and half spray angle, $\theta/2$	100
Figure 6-3- PDFs at different electric potentials for nozzle BD8 at P=3 bar.....	101
Figure 6-4- Cumulative Density Functions at different electric potentials for nozzle BD8 at P=3bar and $Q_L= 6.3$ L/min.	102
Figure 6-5- Diameter d_{70} versus electric potential for nozzle BD8 at P=3bar	103
Figure 6-6 Droplets electric current, I_{drop} , and diameter d_{70} at different electric potentials for nozzle BD8 at P=3 bar.....	103
Figure 6-7- Ratio R and I_{drop} versus the electric potential for the nozzle BD8 at P=3 bar.	105
Figure 6-8. I_{drop} , R and d_{70} versus the electric potential for nozzle BD8 at P=3 bar.....	106

List of Tables

Table 3-1- Summary of fluid-dynamic properties of tested nozzle. SS: Spraying System; LC: Lechler	54
Table 4-1- Chemical speciation of tap water	67
Table 4-2-- Experimental results in uncharged conditions.....	69
Table 4-3-Values of the asymptotic values of the liquid jet breakup, $L_{V\infty}$, the asymptotic potential, V_{∞} , and of the characteristic charging potential, Φ for all tested nozzles together with the corresponding values of the standard error and the coefficients of correlation.....	74
Table 5-1- Lower and higher values of Bond numbers for whipping transition observed from electrical and optical tests.	91
Table 6-1- 70th percentile at $V=0kV$ and $V=V_{min}$, percentage of reduction for all tested nozzles. *Discharge occurring during the test	104

Nomenclature

Latin

a	Major axe of droplet (mm)
a _b	Half sheet thickness at breakup (mm)
a ₀	initial sheet thickness (mm)
A _a	air core area; $A_a = \frac{\pi}{4} (d_o - 2a_0)^2$ (m ²)
A _o	orifice area; $A_o = \frac{\pi}{4} d_o^2$ (m ²)
A _p	total inlet port area (m ²)
A _j	area of liquid jet (m ²)
A _i	Interface area of droplets (m ² /s)
B'	inlet of grounded electrode (m)
B	jet breakup point (m)
B _e	Electrical Bond number (-)
B _{e,L}	Lower value of Bond number at whipping breakup inception from electrical results (-)
B _{e,H}	Upper value of Bond number at whipping breakup inception from electrical results (-)
B _{i,L}	Lower value of Bond number at whipping breakup inception from imaging results (-)
B _{i,H}	Upper value of Bond number at whipping breakup inception from imaging results (-)
CDF	Cumulative Density Function (-)
C	condenser capacitor (C/V)
C _i	Droplet Circularity (-)
C _t	Constant (-)
C _D	discharge coefficient (-)
d ₅₀	50 th percentile of droplets' size distribution (m)
d ₇₀	70 th percentile of droplets' size distribution (m)
d ₉₀	90 th percentile of droplets' size distributions (m)
d ₁₀	10 th percentile of droplets' size distributions (m)
d _L	ligament diameter (mm)
d _D	droplet diameter (mm)
d _{jet}	diameter of liquid jet (m)
d _w	Diameter of droplets with whipping breakup (m)
d _v	Diameter of droplets with varicose breakup (m)
D ₃₂	Sauter mean diameter (m)
D _s	swirl chamber diameter, coincident with D _n (m)
d ₀	orifice diameter of nozzle (m)
D _{po}	entry port nozzle diameter (m)
D _n	diameter of nozzle narrowest section (m)
D-CMR	droplet charge to mass ratio (μC/kg)
D	electric displacement vector (C/m ²)
E	electric field (V/m)
f _e	volumetric electric force (N/m ³)
f	breakup parameter (-)
F _p	total air pressure force (N)
F	pump frequency (Hz)
F _{I,}	inertial force (N)

F_s	surface tension force (N)
F_μ	viscosity force (N)
F_G	gravity force (N)
F_{el}	electric force (N)
F_E	electric force/Coulomb force (N)
F_{Im}	image force (N)
F_{int}	air-liquid interaction force (N)
h	wave amplitude (-)
h_0	initial wave amplitude
\mathbf{H}	magnetic vector (A/m)
\mathbf{H}_m	magnetic field (A/m)
H_j	liquid jet height (m)
i	current intensity (A)
I_{drop}	Droplets' current (A)
I_{gen}	HV power supply current (A)
I_{nozzle}	Nozzle current (A)
\mathbf{I}	identity tensor (N/m)
J_c	current density (A/m ²)
k	wave number (m ⁻¹)
K	Conductivity (K)
K_v	velocity coefficient (-)
K_L	Constant (-)
K_S	wave number corresponding at $\Omega_S (k_{max})$ (m ⁻¹)
L_b	breakup length (m)
$L_{b, \infty}$	Breakup length at asymptote (m)
$L_{b, th}$	Theoretical breakup length (m)
L	distance from the beginning of electric fiend to breakup point (m)
L_o	length of orifice (m)
m	Rosin-Rammler coefficient (-)
m_L	mass of a liquid ligament (Kg)
p	perimeter of liquid jet (m)
PDF	Probability Density Function (-)
P_{80}	Rosin-Rammler distribution coefficient (-)
P	Pressure (atm)
q	electric charge (C)
q_v	droplet specific charge (C/m ³)
q_D	droplet charge (C)
q_{sat1}	Parameter (-)
q_{sat2}	Parameter (-)
Q_L	liquid flow rate (L/min)
Q_R	Rayleigh charge (C)
Q_E	charge of electrode (C)
Q	total electric charge (C)
r_c	cone radius (m)
r_p	Euclidian distance between nozzle and electrode (m)
R	Ratio between electrical and surface tension stresses (-)

R_j	liquid jet radius (m)
R_c	circuit resistance (Ohm)
t	Time (s)
\mathbf{T}^m	mechanical stress tensor (N/m)
\mathbf{T}^e	electric stress tensor (N/m)
u	axial component of liquid velocity (m/s)
\bar{u}	mean axial component of liquid velocity (m/s)
u'	fluctuating axial component of liquid velocity (m/s)
u'_I	irrotational component of fluctuating axial liquid velocity (m/s)
u'_R	solenoidal component of fluctuating axial liquid velocity (m/s)
U_b	liquid velocity at breakup point (m/s)
U	liquid velocity (m/s)
U_0	liquid-gas relative velocity, equal to U (m/s)
U_G	air velocity (m/s)
v_s	liquid sheet velocity (m/s)
v'_I	irrotational component of fluctuating radial liquid velocity (m/s)
v'_R	solenoidal component of fluctuating radial liquid velocity (m/s)
\bar{v}	mean radial component of liquid velocity (m/s)
v'	fluctuating radial component of liquid velocity (m/s)
v_L	radial component of relative velocity U (it is indicated as v) (m/s)
v_{jet}	Liquid jet velocity (m/s)
v_{a0}	initial air velocity (m/s)
v_{L0}	initial liquid velocity (m/s)
v_r	air-liquid relative velocity (m/s)
V	Electric potential (kV)
V_∞	Electric potential at asymptote of breakup length (kV)
V_{min}	Electric potential at which the droplets current has its minimum value (kV)
V_{opt}	electric potential corresponding at maximum value of D-CMR (kV)
V_d	volume of a detached liquid ligament (m ³)
V_w	Whipping electric potential (kV)
w_s	liquid cone width (m)
x	distance between electrode and liquid surface for a plate electrode (m)
X	ratio of air core area to air of final discharge orifice, $X = \frac{A_a}{A_o}$ (-)
Z	distance between nozzle exit and centre of electrode (m)
We_e	Weber number, $We_e = \frac{\rho_G U_L^2 D_0}{\gamma}$ (-)
Re_{ei}	inlet Reynolds number, $Re_{ei} = \frac{\rho_L Q_L D_{po}}{\mu_L A_p}$ (-)
Re_e	Reynolds number, $Re_e = \frac{\rho_L U D_0}{\mu_L}$ (-)
Oh	Ohnesorge number, $Oh = \frac{\mu_L}{\sqrt{\rho_L d_a \gamma}}$ (-)
Greek	
α	Parameter (-)
β	phase angle (°)
β'	Corrective factor (-)
γ	Surface tension (N/m)

γ_e	Electrical surface tension (N/m)
ϵ_a	relative air permittivity (-)
ϵ_L	relative liquid permittivity (-)
ϵ_0	dielectric permittivity of vacuum (F/m)
ϵ_r	relative permittivity (F/m)
ξ	Ratio between gas and liquid densities (-)
ξ_{Lb}	Variation of breakup length (m/m)
η	disturbance on liquid sheet (-)
η_0	initial disturbance on liquid sheet (-)
θ	half spray angle ($^\circ$)
λ	Wavelength (-)
λ'	length of disintegrated volume (m)
σ	Surface charge density ($C \cdot m^{-2}$)
σ_{vol}	Volumetric density charge (C/m^3)
μ_g	gas viscosity (Pa·s)
μ_m	magnetic permittivity (H/m)
μ_L	liquid viscosity (Pa·s)
ρ_L	liquid density (Kg/m^3)
ρ_G	gas density (Kg/m^3)
ρ_s	superficial charge density (C/m^2)
ρ_e	volume charge density (C/m^3)
τ_b	Breakup time (s)
τ	relaxation time (s)
\varkappa_1	Parameter (-)
\varkappa_2	Parameter (-)
ϕ	Charging characteristic potential (kV)
ϕ_L	velocity potential function (-)
ϕ_V	volumetric drop fraction (-)
$\Psi(d)$	Volumetric diameter size distribution (-)
$\Psi(d_s)$	Surface diameter size distribution (-)
ω_c	complex wave growth rate (m/s)
ω_r	real wave growth rate (m/s)
ω_i	imaginary wave growth rate (m/s)
Ω_S	maximum value of real wave growth rate (ω_{max}) (m/s)
Ω	dimensionless number (-)

Abstract

The research is focused on water sprays electrified by induction charging through an external electric field. The aim of this work is to verify and understand how the breakup mechanism of a liquid jet and the droplets' size population are influenced by the electric field.

Two experimental rigs were tested, and they will be named in the text as high-flow rate electrified spray (\approx L/min) and low-flow rate electrified spray (\approx mL/h). The choice to carry experiments on different scaled setup is due to the geometrical simplicity that the low-flow rate water spray system displays, which helped to better understand the physics beyond the electrification of a liquid jet.

In both systems, the liquid was water pumped in a grounded nozzle. The liquid jet crossed an electric field generated by a toroidal ring connected to the HV power supply and placed around the jet itself. The experiments were conducted to estimate: i) the electric current (or the specific charge) acquired by the droplets, ii) the droplets' size population at different electric potentials.

For what concerns the high-flow rate electrified spray, hollow cone hydraulic nozzles were used. We found that the droplets current had a non-monotonic trend with the applied electric voltage: it increased linearly until to reach the optimum value and, after that point, it started to decrease fast. At same time, the breakup mechanism was influenced by the electric field. Indeed, for the primary breakup parameters, we observed that the breakup length reduced with the potential of about 20 % compared with the uncharged value until to reach an asymptotic value, while the spray angle enlarged due to the repulsion between equally charged droplets. In the secondary atomization, the droplets' size distribution shifted toward smaller diameters as the electric potential increased. The percentile diameter, d_{70} , chosen to represent the distribution, was quite constant for all the potentials from 0 kV until the potential at which the electric current was maximum. As soon as the current overcome the optimum point, the d_{70} started to reduce swiftly. In these conditions, the dimensionless ratio between the electrical stress and the surface tension stress, R , rise and become larger than 1, as confirmation of the effective influence of the electric field on liquid jet dynamics. We envisage that the insurgence of corona discharge on liquid jet surface could explain these phenomena.

This hypothesis was confirmed by the experiments made on the low-flow rate electrified sprays or electrospray. In fact, this experimental rig was used to carry studied on the simple jet mode with whipping breakup, where the whipping is an off-axis instability that generates droplets much smaller than the nozzle inner diameter. The tests revealed that as soon as the electric current increased with the potential and the whipping instability took place on the liquid jet surface, the droplets' size population were composed by droplets of size smaller than 0.5 mm. When it happens, the electrical stress overcomes the surface tension, as observed for the high-flow rate spray, and the corona discharge glow took place. It was confirmed by ad-hoc experiments made in a black-room.

The results confirmed that the presence of the electric field modifies significantly the liquid jet atomization dynamic. It could be used to manipulate the droplets' distribution accordingly to the require application.



pic by L. Manna

1.1 Aim of the work

Electrified sprays are adopted in a large number of industrial and medical applications and are present in several natural processes, as, for example, in waterfalls [1]. Water electrification is not so common, but the large use water in chemical engineering processes trigger our attention on this special application. It was proved, for example, the electrified water can be proficiently used to improve the efficiency of gas absorption and submicron particle capture [2], [3] and that electrification can be used to promote water treatments or desalinization processes [4].

All of these processes require treatment of high-water flow rates, which can be achieved either by using conventional spray nozzles, with typical flow rates of several L/min, or arrays of small nozzles. In the first case, the atomization technology is already available at commercial level, but the electrification process was scarcely analysed. In the second case, the electrification of a single nozzle is well known, but the use of multiple sprays has several limitations and is still the subject of explorative studies so far.

The main aim of this research is to better understand the fundamental processes involved in the generation of electrically charged sprays from large flow rate conventional hydraulic nozzles as well as to investigate the mechanisms involved in the transition of varicose and whipping atomization mode in low flow rate EHDA.

In this study, we explored the electrified water sprays for conventional hydraulic nozzles (flow rates between 3 and 10 L/min) and single nozzles operated at high flow rates (up to 1000 mL/h). The main objectives of this work were 1) to evaluate how the presence of an electric field influences the atomization mechanism and 2) to investigate how the morphology and parameters of sprayed droplets change with electric voltage.

For hydraulic sprays, at the best of our knowledge, some authors carried experiments on electrified water sprays observing a reduction of the breakup length and an enlargement of the spray angle with the electric field [5], while another paper indicated a reduction of about 4% of droplets' diameter [6]. However, the most of studies conducted on high flow rate electrified water sprays assumed that the atomization mechanism is not influenced by the electric field [7].

On the contrary, the electrified sprays at low-flow rate have been widely described over the years and semi-empirical correlations that connect electrification and atomization have been developed. However, some phenomena as the whipping breakup establishment are still partially unknown.

The research investigated the primary and secondary atomization mechanisms as a function of electrification, coupling dedicated electrical measures to determine the spray electric charge and optical analyses to investigate the morphology of the liquid lamina and of the sprayed droplets.

Tests with hydraulic sprays were carried out with different kinds of swirl hollow cone nozzles. Tests with nozzles were focused on high flow rates applications, which can be obtained by operating in the so-called whipping mode. This mode is scarcely studied in the literature and, but we envisage that, for its many analogies with the large sprays, its study may provide valuable information to improve our understanding of the underpinning physics of water electrification of hydraulic sprays.

The thesis is organized in six chapters. In this chapter, the basic physics of both spray technology and induction charging mechanism is described, while the models at which the study referred to and a critical literature review are discussed in Chapter 2.

The experimental results are showed and described in Chapter 3-6, which are based on publications or paper on submission, listed at the end of the work. In particular, Chapter 3 is focused on the induction charging and on the primary atomization of electrified water spray at high flow rates of nozzles produced by different companies. Chapter 4 and 6 are based on exploring the effect of electric field on both primary and secondary atomization of hydraulic nozzles made by a single manufacturer, respectively, while chapter 5 shows the results of experimental campaign carried on low-flow rate electrified spray. The choice to interpose Chapter 5 in between the results on atomization process of high-flow rate electrified sprays (e.g. Chapters 4 and 6) is due to the fact that the observations made in Chapter 6 on secondary atomization of hydraulic nozzles are consequence of experimental evidences found and showed in Chapter 5.

Each Chapter from 3 to 6 is organized in i) an introduction section to the specific issue faced in the chapter itself, ii) the description of experimental campaign, iii) discussion of experimental results, iv) summary of the chapter. At last, the conclusion of the research is discussed.

1.2 General physics

A spray is a two phases system of liquid droplets in a gaseous stream and the droplets can be accelerated, decelerated, deformed or broken by interactions with the gaseous phase. The spray is characterized by a wide spectrum of droplets' size that represent the quality of an atomization process. The process of atomization is the disintegration of a liquid jet or a cone in a wide spectrum of droplets. It can be induced by the kinetic energy of the liquid itself, or by a fast air stream or by a mechanical energy applied externally through a rotating or vibrating device. It is a keystone of many chemical and mechanical engineering applications that involve a two phase system of liquids as dispersed phase in a gaseous stream: surface coating, fuel injections, water

scrubbing, drug delivery in medical therapy, synthesis of nanoparticles are some of the possible field of application [7], [8].

Generally, the liquids atomization process has been widely studied over the years and the droplets' distribution, $\psi(d_D)$, depends on the way the liquid cone generates, and it means that it is related to the liquid flow rate and surrounding air pressure and to nozzle geometrical parameters. Indeed, the spraying performances turn upon orifice diameter d_o , length of orifice L_o and half spray angle $\theta/2$, specially for pressure-swirl atomizers, which have been tested in this work [8]–[11].

The efficiency of a spray generated by a pressure swirl hollow cone nozzle is evaluated by the discharge coefficient C_D . It defines the actual flow rate when a fluid crosses a nozzle or a generic constriction. In fact, it is the ratio between the actual flow rate to the theoretical one. Several relations have been written for the discharge coefficient and they differ for the nozzle. For a swirl nozzle, it is calculated as:

$$C_D = \left[\frac{(1-X)^3}{1+X} \right]^{0.5} \quad (1.1)$$

where X is the ratio of air core area A_a and the orifice area A_o , which are strictly dependent on type of used nozzle.

Generally, it is low because of the presence of air core. It was noted a dependence of discharge coefficient from Reynolds number [12]. For low Reynolds number, the liquid viscosity thickens the sheet and the discharge coefficient increases; for large Reynolds number (from 3000 on), the C_D is independent of Reynolds number. It was evaluated a gap between the theoretical discharge coefficient and the experimental one [13]. To reduce this difference, a correcting factor was added at the Equation (1.1):

$$C_D = 1.17 \left[\frac{(1-X)^3}{1+X} \right]^{0.5} \quad (1.2)$$

For pressure swirl nozzles, the discharge coefficient can be expressed as dependent on both nozzle geometry and pressure gauge:

$$C_D = \frac{Q_L}{A_o (\Delta P / \rho_L)^{0.5}} \quad (1.3)$$

where Q_L is the liquid flow rate, ΔP is the difference between the injection pressure and the ambient pressure and ρ_L is the liquid density.

The air core, A_a , develops only above a critical Reynolds inlet number, defined as

$$Re_i = \frac{\rho_L Q_L d_{po}}{\mu_L A_p} \quad (1.4)$$

where A_p is the total port inlet area, entry port diameter d_{po} and μ_L is liquid viscosity.

In fact, for Reynolds numbers lower than the critical one, a full jet exits from the nozzle and a solid cone spray is formed. The air core diameter and its turbulence characteristics influence the droplets size distribution in terms of mean diameter and number of droplets. The larger the air core diameter, the thinner the liquid sheet

thickness, the finer drops. For a given pressure drop, the air core reduces the effective flow area causing a reduction in discharge coefficient. For large Re_i values, the discharge coefficient is not dependent on it [12].

Giffen and Muraszew [13] developed a correlation between the nozzle geometry (d_s diameter of a swirl chamber when it is present) and the air core:

$$\left(\frac{A_p}{d_s \cdot d_0}\right)^2 = \frac{\pi^2}{32} \cdot \frac{(1-X)^3}{X^2} \quad (1.5)$$

where d_s is the diameter of swirl chamber in pressure swirl nozzles.

Once the nozzle geometry was known, the relation (1.5) was used to evaluate the value of ratio X. The thickness of the liquid sheet, a_0 , was calculated from equation (1.6):

$$X = \frac{(d_0 - 2a_0)^2}{d_0^2} \quad (1.6)$$

As relation (1.6) indicates, the area of air core influences strictly the liquid sheet thickness a_0 . Rizk and Lefebvre [14] studied the influence of nozzle geometry (d_0), liquid physical properties and operative conditions (P and Q_L) on liquid sheet thickness a_0 :

$$a_0^2 = \frac{1560 \cdot Q_L \cdot \mu_L}{d_0 \cdot \Delta P_L} \cdot \frac{1+X}{(1-X)^2} \quad (1.7)$$

Higher pressure provides thinner liquid sheets. Indeed, the atomization quality, in terms of droplets' size distributions' spread, improves by increasing the nozzle pressure or rather the liquid discharge velocity and so the liquid film thickness reduces. A thicker film is obtained by a larger orifice diameter due to lower discharge coefficients. At last, the smaller the nozzle diameter, the larger the film thickness, because the air core diameter is smaller, and the nozzle swirl action is reduced. Regarding the fluid physical properties, liquid viscosity influences the sheet thickness. Viscous forces resist the disruption and consequently the film thickness increases. The relation (1.7) was confirmed by experimental results [14]. When $a_0/d_0 \ll 1$, the relation (1.7) can be simplified in

$$a_0 = 3.66 \left(\frac{d_0 Q_L \mu_L}{\rho_L \Delta P} \right)^{0.25} \quad (1.8)$$

The Equation (1.8) shows that the thickness a_0 has not a linear dependence on these parameters, but it depends on them through a coefficient 0.25.

The corresponding of discharge coefficient in terms of liquid velocity is the velocity coefficient K_v . It is defined as the ratio of actual discharge velocity to the theoretical one:

$$K_v = \frac{U}{(2\Delta P/\rho_L)^{0.5}} \quad (1.9)$$

where U is the liquid velocity.

The discharge and the velocity coefficients are correlated as:

$$K_v = \frac{C_D}{(1-X) \cos \theta} \quad (1.10)$$

A reduction of both discharge velocity and of velocity coefficient is achieved by a large orifice diameter and consequently a thinner sheet. On the contrary, an improvement of velocity coefficient at higher pressure levels leads to a reduction in liquid film thickness.

Schmidt et al. [15] proposed different relations to evaluate the velocity coefficient. They assumed that the exit velocity profile was uniform, and the velocity U was given by Equation 1.9. The velocity coefficient ranged between two values:

$$K_v = \max \left[0.7, \frac{4Q_L}{\pi d_0^2 \cdot \cos \theta} \sqrt{\frac{\rho_L}{2\Delta P}} \right] \quad (1.11)$$

The spray angle is influenced by nozzle geometry. According to Taylor's theory [16], it is a function of ratio of inlet port area and the product between the nozzle chamber diameter and orifice diameter. Figure 1-1 reports the theoretical prediction of spray angle in comparison to the experimental one. It was obtained for a non-viscous liquid, and indeed, the experimental data show a difference of 3° for cone angle of 60° due to liquid viscosity.

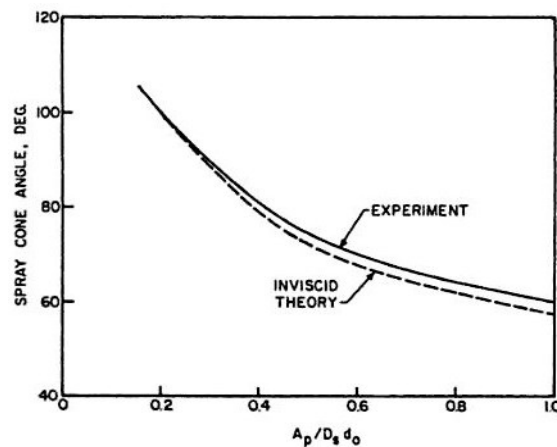


Figure 1-1 Relationship between cone angle and nozzle geometry [16]

Giffen e Muraszew [13] found a relation for a non-viscous liquid between the spray angle and the nozzle geometry:

$$\sin \theta = \frac{\pi/2 \cdot C_D}{\text{const} \cdot (1+\sqrt{X})} \quad (1.12)$$

The relation (1.12) correlated the spray angle with the air core (X), and both the type of liquid and operative conditions (C_D).

The spray parameters here described for a hollow cone could be modified and improved by applying external forces to the spray, as an electrical force. When an electric field is applied, the electric charge acquired by liquid droplets is spread on external surface: the spray delivers inside positive and negative charge, but it is globally electrically neutral. The combination of aerodynamic and electrostatic forces improves the dispersion

of liquids in gas, generates smaller droplets and supports the exploitation of electrified sprays in many research fields as drug delivery, agricultural spray, industrial and food processes or air pollution control [17].

The charging efficiency is strictly related to droplets size: the smaller the droplets size, the higher the charge. Anyway, if the droplets are too small, they become fluid-dynamically uncontrollable and, in a hot system, they evaporate causing a loss of droplet charge.

A liquid droplet in an electric field exerts an electric force, which is opposite to cohesive forces in the liquid as the surface tension force. When the electric force overcomes the surface force, the droplet goes off. The ratio between the two main forces acting on a liquid jet is expressed as [18]–[20]:

$$R = \frac{\sigma^2/4\epsilon_0}{\gamma/L} \quad (1.13)$$

Where σ is the surface density charge, γ is the surface tension, ϵ_0 is the vacuum permittivity and L is the characteristic length on which the stresses are applied, and it can be the liquid jet diameter or the mean droplet diameter. This relation has been developed for low-flow rate liquid jets ($\approx \mu\text{L}/\text{min}$) and for dielectric liquids but it could be generalized by specified the liquid physical properties and the characteristic length, L .

Once an electrical field is applied, a droplet cannot acquire a number of charges indefinitely, but it exists a limit charge level called Rayleigh limit, Q_R . For a droplet of a diameter d_D , it is expressed as:

$$Q_R = \sqrt{8\pi^2\gamma\epsilon_0 d_D^3} \quad (1.14)$$

Actually, the liquid charge on sprays is complicated to measure and this is the reason why the charging level on droplets is expressed as ratio of spray current, I_{drop} , and liquid flow rate, Q_L . This ratio is the droplets specific charge or Droplet Charge to Mass ratio (D-CMR):

$$D - CMR = \frac{I_{\text{drop}}}{Q_L} \quad (1.15)$$

The D-CMR is dependent on electric field strength (applied potential), liquid flow rate, liquid physical properties and droplets diameter. The D-CMR can be increased by changing one of former parameters. Ha et al. [21] employed sea water as liquid spraying in induction charging atomization to capture particles emitted by marine engines. The measured droplets specific charge was higher than the same calculated with tap water. The result was explained by the greater seawater conductivity due to salts presence (3.21 S/m instead of 0.75 S/m): in water, the salts released ions, and these enhanced the charging phenomenon. Indeed, the liquid conductivity, which represents the property of a liquid to transport charges when an electric field or a potential difference is applied, increases in presence of aqueous impurities. Some experimental tests that we are carrying by changing the liquid conductivity confirm that the droplets current increases proportionally to liquid conductivity. The same trend is observed if the electric field is more intense or if the liquid flow rate is increased due to the larger number of droplets that carry an electric charge

1.3 Charging Mechanism

There are three main technological approaches to spray charging, as shown in Figure 1-2: exposure to corona ions (A), contact charging (B) and induction charging (C).

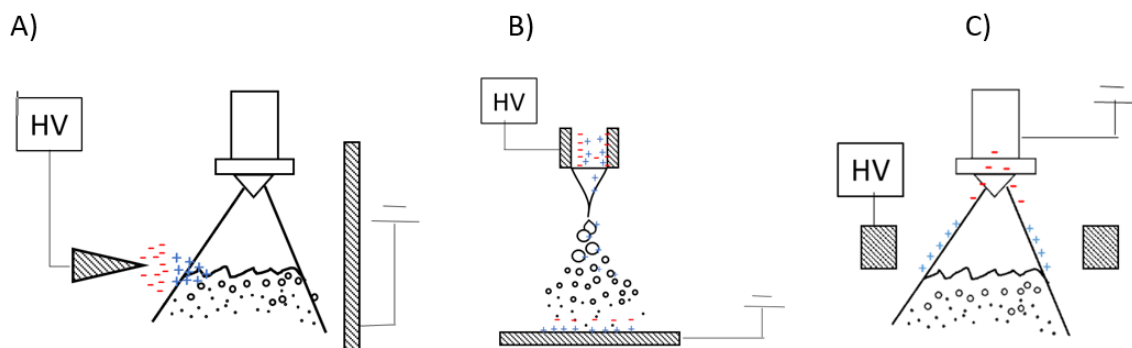


Figure 1-2- Schematic representation of charging mechanisms. A) corona charging; B) contact charging and C) induction charging

In corona charging (A), the liquid droplets are charged by bombardment of fast moving ions, generated from a nozzle connected to high potentials, on the surface of the droplets and it is also denoted as ion attachment. Via corona charging, the charge acquired by the droplets has the same polarity of the applied voltage. The level of charge is dependent on the dielectric constant of the medium, its surface area, the electrical characteristics of the corona discharge and the residence time within the ionized field. In corona charging, the Rayleigh percentage is about 5% and it is usually used at very low liquid flow rate (\approx mL/min). In contact charging (B), the liquid is emitted from a nozzle and it is exposed to a strong electric field. In this type of mechanism, the liquid flow rate is relatively low (\approx μ L/min), charging of liquid droplets is strictly correlated to atomization process or electrospray modes [22]. Therefore, the electric charge is directly transferred to the liquid surface and it is trapped into droplets while these are forming. In the induction charging (C), a positively or negatively charged HV electrode is held near a grounded spray nozzle. The liquid cone is polarized: the liquid exiting from the nozzle breaks up due to natural surface instability phenomena and the formed droplets trap a charge opposite to electrode one, while the free charges with same polarity of electrode move towards the ground via the nozzle [23]. Highest charging level is reached by means contact charging: the ratio between the droplet charge, Q_D , and the Rayleigh charge limit, Q_R , is about 30- 40%. If the liquid flow rate is about L/min, the induction charging is the reasonable mechanism, but the Rayleigh percentage is low and about the 10%.

Generally, the contact charge mechanism used for low-flow rate sprays and it is denoted as electrospray [24]. Actually, the electrospray refers to any electrified spray at liquid flow rates about few μ L/h or mL/h in nozzles with inner diameters of hundreds of micrometers. It means that an electrospray can be performed even with a nozzle grounded and a counter-electrode connected to a HV power supply [25].

In this work, two different experimental rigs of electrified sprays were tested, and both were charged by induction charging. In the first one, pressure swirl atomizers were used, and the liquid flow rate was about L/min, while in the second one smooth nozzle were tested at liquid flow rate of few mL/h. The two experimental rigs will be referred in this work as high-flowrate and low-flowrate spray from here on.

1.3.1 High flow rate electrified spray

As discussed, the induction charging is the best compromise between water flow rate and charging level. When the induction charging is applied on a high flow rate water spray, the induction charging is effective if the fluid is sufficiently conductive to allow an efficient charge transfer to droplets during spray formation [23], [26]. It means that the charge relaxation time, τ , has to be much smaller than droplets formation time, τ_b . The former time indicates how fast the charges are transferred to a liquid, while the latter one describes how fast the liquid disrupts in droplets.

If the liquid is tap water with electrical conductivity K of 0.0715 S/m, the relaxation time can be evaluated:

$$\tau = \frac{\epsilon_0 \cdot \epsilon_r}{K} = \frac{8.85 \cdot 10^{-12} \cdot 78.5}{0.0715} = 9.71 \cdot 10^{-8} \text{ s} \quad (1.16)$$

where ϵ_r is the relative permittivity. The droplets formation time is expressed as:

$$\tau_b = \frac{L_b}{U} \quad (1.17)$$

where L_b is the breakup length and U is the liquid jet velocity. It means that the induction charging depends on liquid physical properties. It is indicated that the minimum liquid conductivity required for induction charging is 10^{-10} S/m [27]. Thanks to its high conductivity, water is an appropriate candidate to electrified spray, but electrification of water sprays is more unstable than that of dielectric and/or organic liquids [28] because of ionic composition and because its physical properties are subject to substantial change in presence of electric field [29].

Considering that the liquid cone surface and the electrode are held at different electric potentials, the system can be schematized as a condenser. The driving force is the Coulombian interaction between negative and positive charges:

$$F_E = \frac{Q_D Q_E}{4\pi\epsilon_0 r_p^2} \quad (1.18)$$

where r_p is the Euclidian distance between the electrode and the nozzle, Q_E is the electrode charge. It is a function of the potential V and the condenser capacitor C :

$$Q_E = CV \quad (1.19)$$

The system electrode-sprayed liquid surface as a condenser is represented in Figure 1-3:

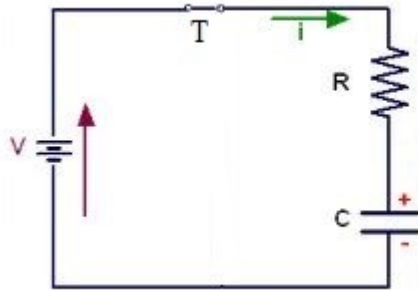


Figure 1-3 Electric circuit as schematization of induction charging system

Where V is the potential difference, T is the switch, C represents the condenser and R is the whole system resistance. The negative side of condenser represents the electrode, and the positive one is the liquid surface. Once the switch is on, the electric current starts flowing from the electrode to the spray. The condenser capacity changes with electrode geometry. The electrode can be formed by two parallel and flat plates, or by a toroidal ring. For a toroidal ring, the electric circuit is schematized as in Figure 1.4 where the electrode has a negative polarity and the liquid cone is positively charged.

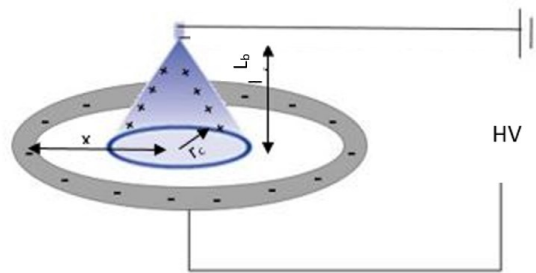


Figure 1-4- Electrical circuit with a toroidal electrode and a pressure hollow cone nozzle [1]

For this system, the condenser capacity is defined as:

$$C = \frac{2\pi\epsilon_0\epsilon_r L_b}{\ln\left(\frac{x}{r_c}\right)} \quad (1.20)$$

where r_c is the cone radius and it can be easily estimated once the breakup length, L_b , and the spray angle, θ , are known. It is assumed to be constant, but it should be expressed as a function of liquid jet height $r=r(H_j)$.

The electrode surface charge density is given by:

$$\sigma = \frac{Q_E}{4\pi(x-r_c)^2} \quad (1.21)$$

The spray current is:

$$i = 2\pi r_c U \sigma \quad (1.22)$$

The atomization mechanism of this type of spray is described in paragraph 2.1, even though atomization models that gather the electrification of the liquid cone are missing.

1.3.2 Low flow rate electrified spray

The electrification of sprays at low flow rate is denoted as ElectroHydroDynamic Atomization (EHDA) or electro-spraying. It is the deformation of liquid meniscus by the presence of electric field that overcomes the surface tension and disrupts the liquid in droplets [30]. If it is charged by contact, the liquid flows from a nozzle connected to a high voltage supply and it is collected on a grounded counter-electrode. Otherwise, the nozzle is grounded, and the counter-electrode is connected to high voltage power supply (induction charging). The EHD atomization can be performed with liquids whose surface tension and conductivity are at least higher than 50 mN/m and 10^{-11} S/m, respectively [24]. The surface tension and conductivity with the dielectric permittivity are the liquid properties that mostly influence the atomization process because they denote the tendency of liquid to be influenced from the electric field. The electro-sprayed droplets acquire a level charge about 50-70% of Rayleigh limit [24].

The interest in this atomization and charging mechanism has swiftly rose in recent years, encouraged mainly by its new applications [31], [32]. The scientific and industrial applications of electro-spraying can be roughly categorized into small-output and large-output processes [33]. The first category comprises ink-jet printing, micro- or nanopatterning in electronics (non-contact alternative to photolithography), fuel injection, microparticle manufacturing for drug delivery [34], [35], thin film deposition[36], micromachining, nanoparticle sprays (e.g. in electrospray ionization for mass spectrometry of highly charged biological macromolecules [37]–[39]), ingredients dosage in the cosmetic and food industries. The second category gathers fire extinguishing, wet scrubbers (precipitation of dust or smoke)[40], [41], agriculture sprays crop protection (pesticides), spray coating [42] and painting, or ceramic films fabrication[43]. Moreover, the development of new detecting technologies (as high-speed camera or lasers) improved significantly the study of EHD atomization and the description of the phenomenology.

The behaviour and properties of the EHD spray depend on many different parameters, i.e. the liquid properties, nozzle geometry, wetting properties etc. Regarding the nozzle geometry, different nozzles designs can be employed, but the conventional cylindrical nozzle is the most common nozzle design [44] with inner diameters ranging from few micrometres to 1 mm [44]. The tip of the nozzle could be smooth or sharpened but the second one is the less used to avoid electric discharges because of a too intense electric field nearby.

Two different wetting modes has been observed. They depend mainly on both type of nozzle geometry and material and on liquid physical properties [44]. In the first wetting mode, called inner wetting mode, the liquid generates a meniscus at the base of the nozzle equal to the inner diameter of the capillary. The second type is denoted outer wetting, and, in this case, the liquid meniscus covers the outer edge of the capillary. The two wetting types are shown in Figure 1-5.

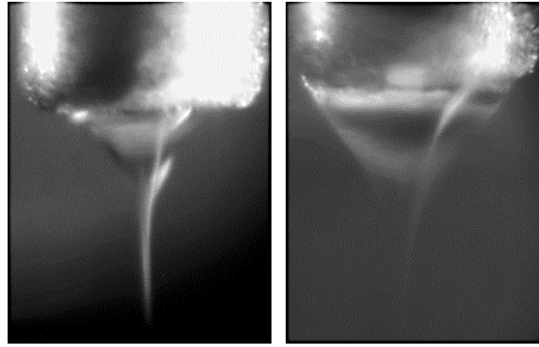


Figure 1-5- Inner Wetting (left) and outer wetting (right) of the nozzle [44]

The setup used for electro spray is normally composed of a nozzle where a liquid is pumped through and a metallic counter-electrode (ring or plate) placed at a certain distance from it. Between them, a potential difference is applied to generate a strong electric field. In case of a ring-nozzle electro spray unit, two types of configurations are available: nozzle-ring up or nozzle-ring down. The difference between them is the direction and the strength of the electric field exerted on the liquid jet and consequently the atomization mechanisms. For a defined set-up geometry, liquid type and operating conditions (flow rate and electric potential), different “spraying modes” can be created [31]. Those modes are based on the shape of liquid meniscus at nozzle outlet and on type of liquid behaviour in its disintegration into droplets [30], [31]. They are generally classified on Weber number, which is the the ratio between the aerodynamic force and the surface tension force:

$$We = \frac{\rho_G d_D U^2}{\gamma} \quad (1.23)$$

The modes are divided into “low- flow rate” modes (at Weber number lower than 1) in which the liquid is atomized directly at nozzle exit producing droplets (*enhanced dripping mode*, *cone-jet mode*) and into “high-flow rate” modes ($We > 4$) that gathers the regimes in which the liquid elongates from the nozzle forming a continuous jet that breaks into droplets (*simple-jet mode*) [19], [45], [46]. In between, the spray is in *transition regime*, which has not been deeply investigated.

In *the enhanced dripping mode*, as showed in Figure 1-6-A, a train of droplets with equal size and reproducibility is produced. In this mode, the droplet size distribution is monodispersed, the droplet diameter is bigger than nozzle outer diameter.

Compared with the uncharged spray or dripping regime, the frequency of droplet emission in the enhanced dripping mode is increased. It is still valid the Rayleigh relation that the droplet diameter is about six times the nozzle inner diameter [47].

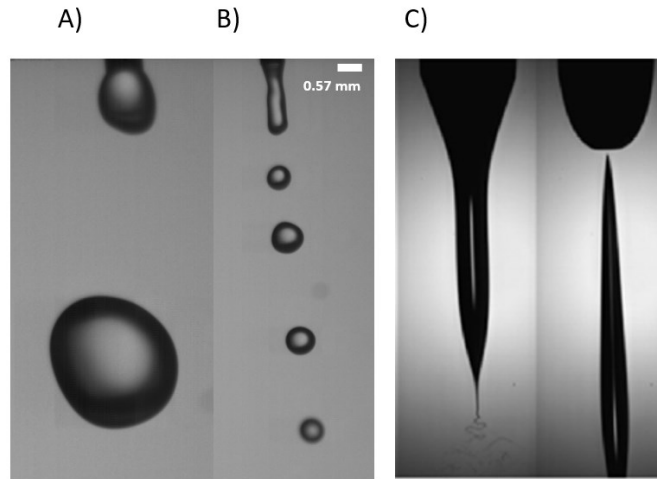


Figure 1-6- Electrospray modes. A) enhanced dripping mode. B) microdripping. C) spindle mode [33]

For distilled water, the droplet diameter decreases from 1000 μm (uncharged spray) to 300 μm (charged spray) with potential increase for a nozzle with inner diameter of 0.65 mm [30]. For liquids with conductivity lower than 10^{-6} S/m [22], as the electric potential increases, the droplets become smaller than those emitted in *dripping mode* and their diameters are much smaller than nozzle inner diameter [31]: this mode is the *micro-dripping mode* (Figure 1-6-B). The *micro-dripping* and the *dripping mode* establish in a narrow window of flow rates and voltages. As the flow rate and/or the potential are increased a bit, the liquid emerges as *spindles* in the direction of electric field and the mode turns into the *spindle mode* (Figure 1-6-C). The spindles disrupt in main and sibling droplets whose diameters range from 300 μm to 500 μm for the former and from 100 μm to 80 μm for the latter. For distilled water, this mode is observed at voltage about 9-11 kV [31]. As the electric potential increases, the number of points of spindles emission on nozzle surface becomes higher. In *multi-spindle mode*, the droplets are produced in the same way of *spindle mode*, but the multi-spindles are not observed simultaneously but they are emitted periodically from the nozzle surface and in opposite directions because of electrical repulsion [31].

At same potentials of *spindle-mode* but at higher flow rates, the *cone-jet mode* is observed. Generally, the electrostatic force opposes the surface tension force acting on liquid meniscus that is deformed generating the several spraying modes. When the electric stress and surface tension stress acting on the liquid surface are

balanced to form a conical-like surface, called Taylor cone, with a semi- vertical angle of 49.3° sprays out from the nozzle tip, as represented in Figure 1-7 [48]–[50].



Figure 1-7- Cone jet mode with varicose breakup (left) and whipping breakup (right) [47]

From the cone tip, a filament elongates that breaks into the droplet distribution. Once the *cone-jet mode* is established, it is stable and let producing a continuous droplet flow. Different authors noted that the operating window in which it can be found is quite narrow [31], [34], [46], [51]. As observed by Cloupeau and Prunet-Foch [22], for liquids with low conductivity it is quite impossible to produce spontaneously fine jets in *the cone-jet mode*.

The *cone-jet mode* appears when a minimum liquid flow rate is pumped through the nozzle. It is a function of liquid physical properties as dielectric permittivity, surface tension, density and conductivity [51]. The advantage of this mechanism is related to droplets size that are smaller than 1 mm in some case even though the liquid flow rate is order of $\mu\text{L}/\text{min}$. This is the reason why it has been the most electro-spray mode studied and used in industrial applications. Indeed, the droplet size and the current emitted in this mode could be predicted by scaling laws developed by studies conducted on dielectric liquids as ethanol, ethylene glycol and ethyl alcohol [30], [46], [51].

The droplet diameter, d_D , is related to the liquid flow rate Q_L and physical properties as surface tension γ and conductivity K in a generic form as [24], [44], [52]:

$$d_D = \text{const} \cdot (Q_L)^a \cdot (\gamma \cdot K)^{-b} \quad (1.24)$$

Hartman et al. [53] investigated the cone-jet mode breakup mechanism for different liquids. It was observed that the liquid jet elongated by the tip of the Taylor cone could assume two different breakup mechanisms: the varicose breakup and the whipping breakup. The dependence of droplet diameter on liquid flow rate depended on breakup mechanism and two correlations were found for the varicose breakup, d_v , and whipping breakup, d_w , which are respectively:

$$d_v \approx \left(\frac{\rho \varepsilon_0 Q_L^3}{\gamma K} \right)^{1/6} \quad (1.25)$$

$$d_w \approx \left(\frac{\varepsilon_0 Q_L}{\gamma K} \right)^{1/3} \quad (1.26)$$

When the liquid inertia (e.g. the flow rate) is high enough to produce a stable jet and the electric potential is the same of the *cone-jet mode*, the mode is called *simple-jet mode*. The main difference between the *cone-jet mode* and the *simple-jet mode* is the production of droplets. In the former, the jet emerges from the cone formed at nozzle exit, in the latter the jet is emitted directly from the nozzle [45]. Agostinho et al. [45] observed that the *simple-jet mode* has three main breakup mechanisms: varicose breakup, whipping breakup and ramified breakup, showed in Figure 1-8.

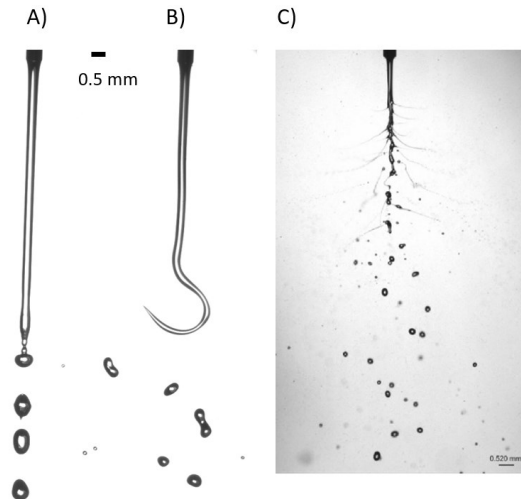


Figure 1-8 Simple jet mode with varicose breakup (A), whipping breakup (B) and ramified breakup (C). The picture C) was taken from [49]

The former is comparable with the breakup mechanism of an uncharged jet in the jetting regime, but the presence of the electrical stresses can reduce the liquid jet radius, thus the droplet size as well [45]. The whipping breakup takes place when the electric stresses are high enough to create off-axis instabilities of the jet. The droplets size produced in the *simple-jet mode* is lower than nozzle diameter, but the high liquid flow rates make this electro spray mode suitable for application that need high flow rates, as observed by Agostinho et al. [45].

The liquid jet established at $We > 4$ for an uncharged spray has a diameter d_j almost equal to the nozzle inner diameter or outer diameter if the nozzle wetting is inner or outer, respectively. The diameter of droplets detached from the liquid jet is 1.8 time the jet diameter [25], [45], [54], [55]. When the electric field is applied, the liquid jet diameter keeps preserving the same correlation with nozzle dimension, but the droplet diameter is deeply influenced by the electrification process. Indeed, in the simple jet mode with whipping breakup multi-modal distributions of droplets' size were observed, as reported in Chapter 5.

Agostinho [25] resumed in a regime map how the liquid flow rate and the electric potential could influence the electro spray mode. The map is showed in Figure 1-9 and it is divided in three zone. The dripping regime zone at Weber lower than 4, the jetting regime at Weber larger than 4 and the transition regime zone in between. The *dripping* and *jetting regimes* include the electro spray modes that take place at low-flow rate and high flow rate, already described.

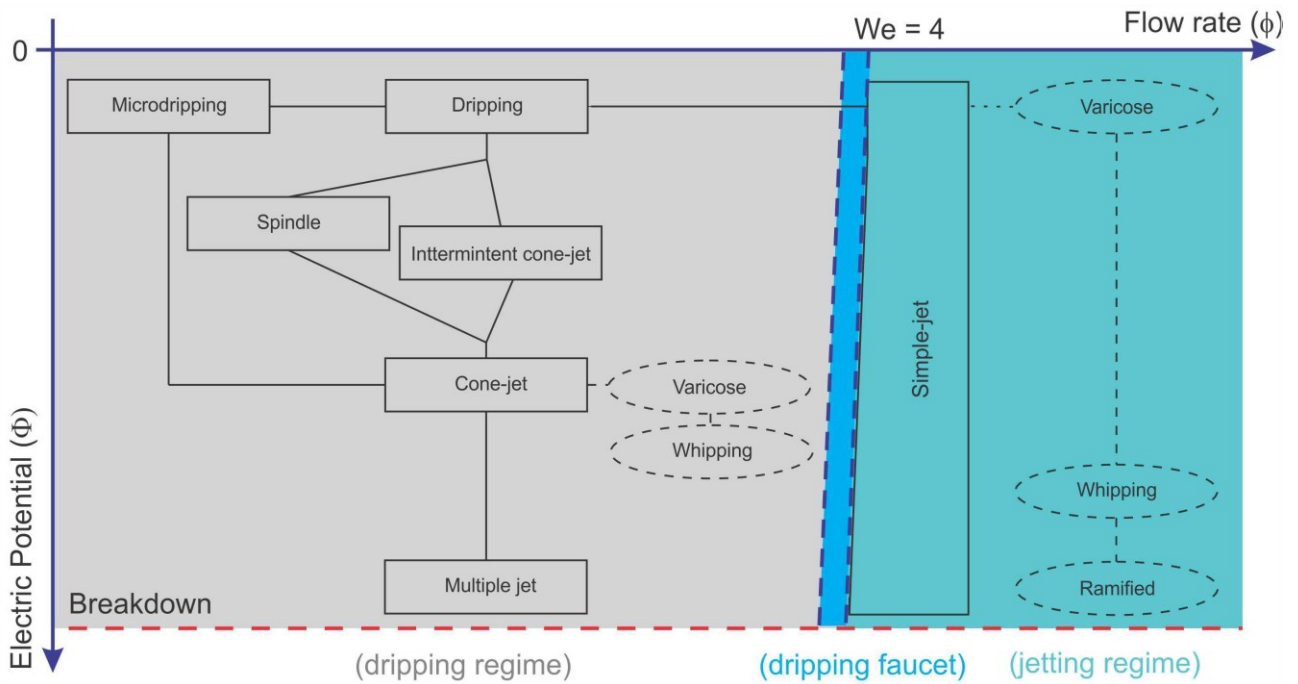


Figure 1-9- Electrospray mode map as function of electric potential and liquid flow rate [25]

The same author [19] suggested to correlate the electric potential with the nozzle geometry by a dimensionless number, the electric Bond number, express as:

$$B_e = \frac{\varepsilon \cdot V^2}{\gamma \cdot d_i} \quad (1.27)$$

Where d_i is the nozzle inner diameter. It is a comparison between the electric force and the surface tension and, most of all, it allows to compare experimental results made with the same liquid but different nozzles.

1.4 References

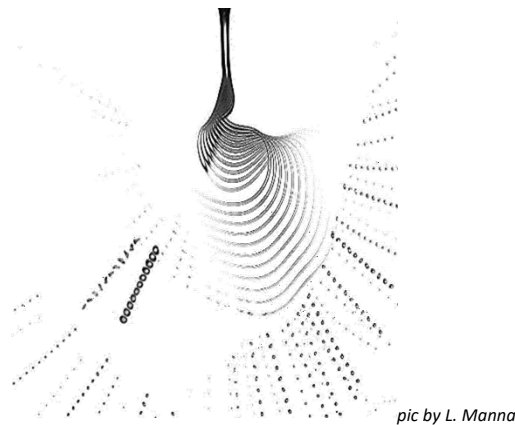
- [1] E. T. Pierce and A. L. Whitson, "Atmospheric Electricity and the Waterfalls of Yosemite Valley," *J. Atmos. Sci.*, vol. 22, pp. 314–319, 1964.
- [2] L. D'Addio, C. Carotenuto, W. Balachandran, A. Lancia, and F. Di Natale, "Experimental analysis on the capture of submicron particles (PM0.5) by wet electrostatic scrubbing," *Chem. Eng. Sci.*, vol. 106, pp. 222–230, 2014.
- [3] C. Carotenuto, F. Di Natale, and A. Lancia, "Wet electrostatic scrubbers for the abatement of submicronic particulate," *Chem. Eng. J.*, vol. 165, no. 1, pp. 35–45, Nov. 2010.
- [4] F. Di Natale, C. Carotenuto, L. Manna, and A. Lancia, "Chemi-electro-hydrodynamic of sulphur dioxide absorption by electrified water drops," *Chem. Eng. Trans.*, vol. 69, 2018.
- [5] G. N. Laryea and S. Y. No, "Spray angle and breakup length of charge-injected electrostatic pressure-swirl nozzle," *J. Electrostat.*, vol. 60, no. 1, pp. 37–47, 2004.
- [6] J. A. Marchant and R. Green, "An electrostatic charging system for hydraulic spray nozzles," *J. Agric. Eng. Res.*, vol. 27, no. 4, pp. 309–319, 1982.
- [7] A. Jaworek and A. Krupa, "Charged Sprays Generation," in *Sprays: Types, Technology and Modeling*, Maria C. Vella, Ed. Nova Science Publishers, Inc., 2011, pp. 1–100.
- [8] C. Dumouchel, "On the experimental investigation on primary atomization of liquid streams," *Exp. Fluids*, vol. 45, no. 3, pp. 371–422, 2008.
- [9] N. Ashgriz, *Handbook of atomization and sprays: theory and applications*, vol. 1. 2011.
- [10] C. J. Clark and N. Dombrowski, "Aerodynamic Instability and Disintegration of Inviscid Liquid Sheets," *Proc. Roy. Soc. Lond. A*, vol. 329, p. 467, 1972.
- [11] P. K. Senecal, D. P. Schmidt, I. Nouar, C. J. Rutland, R. D. Reitz, and M. L. Corradini, "Modeling high-speed viscous liquid sheet atomization," *Int. J. Multiph. Flow*, vol. 25, no. 6–7, pp. 1073–1097, 1999.
- [12] A. Radcliffe, "The performance of a type of swirl atomizer," in *Proceedings of the Institution of Mechanical Engineers*, 1955.
- [13] Edmund Giffen and A. Muraszew, *Atomization of Liquid Fuels*. Chapman & Hall, 1953.
- [14] Levebvre, *Atomization and Sprays*. .
- [15] D. P. Schmidt *et al.*, "Pressure-Swirl Atomization in the Near Field," *SAE Tech. Pap.*, vol. 1999, no. 1999-1–496, 1999.

- [16] G. I. Taylor, “No The mechanics of Swirl Atomizers,” in *Seventh International Congress of Applied Mechanics*, 1948, pp. 280–285.
- [17] K. Tang, “The Electrospray: Fundamentals and Feasibility of its Application to Targeted Drug Delivery by Inhalation.” 1994.
- [18] D. Camelot, J. C. M. Marijnissen, and B. Scarlett, “Bipolar coagulation process for the production of powders,” *Ind. Eng. Chem. Res.*, vol. 38, no. 3, pp. 631–638, 1999.
- [19] K. B. Geers, “Application to Electrospray: from people to plants,” TU Delft, 2003.
- [20] R. P. A. Hartman, “Electrohydrodynamic Atomization in the Cone Jet Mode,” *Thesis*. p. 177, 1998.
- [21] T. H. Ha, O. Nishida, H. Fujita, and H. Wataru, “Enhancement of diesel particulate matter collection in an electrostatic water-spraying scrubber,” *J. Mar. Sci. Technol.*, vol. 15, no. 3, pp. 271–279, Sep. 2010.
- [22] M. Cloupeau and B. Prunet-Foch, “Electrohydrodynamic Spraying Functioning Modes A Critical Review,” *J. Aerosol Sci.*, 1994.
- [23] J. L. Hensley, X. Feng, and J. E. Bryan, “Induction charging nozzle for flat fan sprays,” *J. Electrostat.*, vol. 66, no. 5–6, pp. 300–311, 2008.
- [24] A. Jaworek and A. T. Sobczyk, “Electrospraying route to nanotechnology: An overview,” *J. Electrostat.*, vol. 66, no. 3–4, pp. 197–219, 2008.
- [25] L. L. F. Agostinho, “Electrohydrodynamic Atomization in the Simple-Jet Mode: Out-scaling and Application,” 2013.
- [26] S. E. Law, “Embedded- Electrode Electrostatic-Induction Spray-Charging Nozzle: Theoretical and Engineering Design,” *Trans. ASAE*, vol. 21, no. 6, pp. 1096–1104, 1978.
- [27] S. E. Law, “Agricultural electrostatic spray application: a review of significant research and development during the 20th century,” *J. Electrostat.*, vol. 6, pp. 25–42, 2001.
- [28] O. Lastow and W. Balachandran, “Novel low voltage EHD spray nozzle for atomization of water in the cone jet mode,” *J. Electrostat.*, vol. 65, no. 8, pp. 490–499, 2007.
- [29] M. Chaplin, “Theory vs Experiment: What is the Surface Charge of Water?,” *Water J.*, 2008.
- [30] A. Jaworek and A. Krupa, “Jet and drops formation in electrohydrodynamic spraying of liquids. A systematic approach,” *Exp. Fluids*, vol. 27, no. 1, pp. 43–52, 1999.
- [31] A. Jaworek and A. Krupa, “Classification of the Modes of Ehd Spraying,” *J. Aerosol Sci.*, vol. 30, no. 7, pp. 873–893, 1999.

- [32] M. Cloupeau and B. Prunet-Foch, "Electrostatic spraying of liquids: Main functioning modes," *J. Electrostat.*, vol. 25, no. 2, pp. 165–184, 1990.
- [33] J. Majewski, "Measurement methods for size and charge distributions of electrosprayed water droplets."
- [34] K. Tang and A. Gomez, "Generation of Monodisperse Water Droplets from Electrosprays in a Corona-Assisted Cone-Jet Mode," *J Colloid Interface Sci*, vol. 175, no. 2, pp. 326–332, 1995.
- [35] K. Tang and A. Gomez, "Generation by electrospray of monodisperse water droplets for targeted drug delivery by inhalation," *J. Aerosol Sci.*, 1994.
- [36] J. L. Castillo, S. Martin, D. Rodriguez-Perez, F. J. Higuera, and P. L. Garcia-Ybarra, "Nanostructured porous coatings via electrospray atomization and deposition of nanoparticle suspensions," *J. Aerosol Sci.*, no. March, pp. 0–1, 2018.
- [37] F. Carbone and A. Gomez, "High-Resolution DMA Measurements of Nascent Soot in a Moderately Sooting Laminar C₂H₄/air Premixed Flame," *Aerosol Sci. Technol.*, 2015.
- [38] E. Bodnár, J. Grifoll, and J. Rosell-Llompart, "Polymer solution electrospraying: A tool for engineering particles and films with controlled morphology," *J. Aerosol Sci.*, 2018.
- [39] J. Rosell-Llompart, J. Grifoll, and I. G. Loscertales, "Electrosprays in the cone-jet mode: From Taylor cone formation to spray development," *J. Aerosol Sci.*, no. November 2017, pp. 1–30, 2018.
- [40] F. Di Natale *et al.*, "Capture of fine and ultrafine particles in a wet electrostatic scrubber," *J. Environ. Chem. Eng.*, vol. 3, no. 1, pp. 349–356, Mar. 2015.
- [41] L. D'Addio, F. Di Natale, C. Carotenuto, W. Balachandran, and A. Lancia, "A lab-scale system to study submicron particles removal in wet electrostatic scrubbers," *Chem. Eng. Sci.*, vol. 97, pp. 176–185, Jun. 2013.
- [42] A. Jaworek, A. T. Sobczyk, and A. Krupa, "Electrospray application to powder production and surface coating," *J. Aerosol Sci.*, no. October 2017, pp. 1–36, 2018.
- [43] W. Balachandran, P. Miao, and P. Xiao, "Electrospray of fine droplets of ceramic suspensions for thin-film preparation," *J. Electrostat.*, vol. 50, no. 4, pp. 249–263, Mar. 2001.
- [44] O. Lastow, "Numerical and Experimental Study of Electrohydrodynamic Atomisation of Aqueous Liquids," no. June, 2007.
- [45] L. L. F. Agostinho, G. Tamminga, C. U. Yurteri, S. P. Brouwer, E. C. Fuchs, and J. C. M. Marijnissen, "Morphology of water electrosprays in the simple-jet mode," *Phys. Rev. E - Stat. Nonlinear, Soft Matter Phys.*, vol. 86, no. 6, pp. 1–9, 2012.

- [46] J. M. Grace and J. C. M. Marijnissen, “A review of liquid atomization by electrical means,” *J. Aerosol Sci.*, vol. 25, no. 6, pp. 1005–1019, 1994.
- [47] L. R. F.R.S., “On the equilibrium of liquid conducting masses charged with electricity,” *London, Edinburgh, Dublin Philos. Mag. J. Sci.*, vol. 14, pp. 184–186, 1882.
- [48] J. F. De La Mora and I. G. Loscertales, “The current emitted by highly conducting Taylor cones,” *J. Fluid Mech.*, 1994.
- [49] J. F. De La Mora, “The effect of charge emission from electrified liquid cones,” *J. Fluid Mech.*, vol. 243, no. 1, p. 561, 1992.
- [50] M. Cloupeau and B. Prunet-Foch, “Electrostatic spraying of liquids in cone-jet mode,” *J. Electrostat.*, 1989.
- [51] A. M. Gañán-Calvo, J. Davila, and A. Barrero, “Current and Droplet Size in The Electro spraying of Liquids. Scaling Laws,” *J. Aerosol Sci.*, 1997.
- [52] J. F. De La Mora, J. Navascues, F. Fernandez, and J. Rosell-Llompert, “Generation of Submicron Monodisperse Aerosols in Electro sprays,” *J. Aerosol Sci.*, 1990.
- [53] R. P. A. Hartman, D. J. Brunner, D. M. A. Camelot, J. C. M. Marijnissen, and B. Scarlett, “Jet break-up in electrohydrodynamic atomization in the cone-jet mode,” *J. Aerosol Sci.*, vol. 31, no. 1, pp. 65–95, 2000.
- [54] L. L. F. Agostinho, C. U. Yurteri, E. C. Fuchs, and J. C. M. Marijnissen, “Monodisperse water microdroplets generated by electrohydrodynamic atomization in the simple-jet mode,” *Appl. Phys. Lett.*, vol. 100, no. 24, pp. 1–5, 2012.
- [55] L. L. F. Agostinho, B. Bos, A. Kamau, S. P. Brouwer, and J. C. M. Marijnissen, “Simple-jet mode electro sprays with water . Description , characterization and application in a single effect evaporation chamber .”

Chapter 2. Critical Literature Review



In this chapter, the models supporting the research are discussed. Firstly, the atomization models for conventional large flow rate nozzles are reported, followed by the EHDA theory applied on low flow rate atomization mechanisms. At last, the charging of electrified sprays is described by means of both the theory of electrohydrodynamic atomization and the induction charging models.

2.1 Atomization models

One of the main issues of spray dynamics is predicting the properties of the sprayed droplets starting from the geometric parameters and the overall fluid dynamic features of the spray nozzle. In fact, in every application the spray efficiency depends on drop-size distribution, drop-velocity distribution, density (defined as number of droplets per unit volume), spatial distribution (defined as local volume fraction) and drop temperature [2]. The pertinent literature presented several diagnostic or theoretical models to describe the spray properties.

Models for conventional sprays are good enough to predict the average properties of hydraulic sprays and clarify the importance of the jet breakup mechanisms in determining the droplet size and velocity [3]. The breakup of liquid sheet into droplets is a complex process and two factors mainly influence the mechanism: i) the initial disturbance on liquid-gas interface and ii) its growth rate, which leads to liquid breakup [2]. Three modes of disintegration can be considered [57]: rim mode, perforated-sheet mode, wavy mode. In the first one, the surface tension causes a contraction on liquid sheet until to a thick rim is formed and then it breaks into droplets. In the second mechanism, some holes form in the sheet. These grow and coalesce producing liquid ligaments of irregular shape. The ligaments, then, break into droplets. The last mode is the wavy one and it is the one occurring in this research. In literature, many studies have been conducted on these mechanisms and the main parameter that they consider is the breakup length that is the distance between the orifice and the position where the jet breaks.

For a given flow rate and nozzle geometry, the break up length determines the properties of the ligaments and the primary droplets and defines the secondary atomization pattern. The models that have been extrapolated to

estimate the breakup length were based on studies with fuels or hydrocarbons. Dombrowski and Clark [4] conducted a one-dimensional and linear analysis on viscous liquids. In their studies, the authors considered an asymmetric disturbance acting on liquid sheets as a long sinuous wave. Senecal [5] extended the Dombrowski and Clark investigation in a two-dimensional analysis and pointed out that the perturbation was dependent on wave type (long or short). Han [58] applied the breakup length relations of previous studies at a pressure swirl fuel injector and simulated the atomization process to obtain details hard to estimate experimentally. It is worthy to say that all these models are based on a linear stability theory: the wavy disturbance acting in liquid grows only in time until to reach the critical value at breakup. Recent studies have started to consider a space-temporal stability: the perturbation grow in time as well as in space [2], [59]. For pressure swirl atomizer, the wavy mechanism is well described by Linearized Instability Sheet Atomization (LISA) model.

2.2 LISA model

The LISA model or Linearized Instability Sheet Atomization model takes into account the breakup mechanism of a liquid sheet. Firstly, the equations of disturbance that acts on liquid sheet are presented and then, the breakup parameters are discussed.

2.2.1 Mathematical analysis

The LISA model was developed from an accurate study about the liquid dynamic. The bulk liquid is transformed into a liquid sheet before the atomization process. The sheet is subjected to a spatial and temporal instability due to the aerodynamic interaction with the surrounding gas. When a liquid/gas interface is perturbed, the surface tension forces tend to bring it back to its unperturbed form. The instability has the form of a wave disturbance. The model takes into account two modes of oscillations: symmetric and antisymmetric. In the first case, the sheet middle plane is undisturbed by the wave, the waves at upper and lower interfaces are in phase; in the second mode, instead, the free surfaces move with the same velocity of liquid jet, the waves are π radians out of phase. The two modes are caused by dilatational or varicose waves for the antisymmetric instability and by sinuous waves for the symmetric one. Figure 2-1 is a one-dimensional scheme. It does not regard a variation of sheet thickness in y-direction.

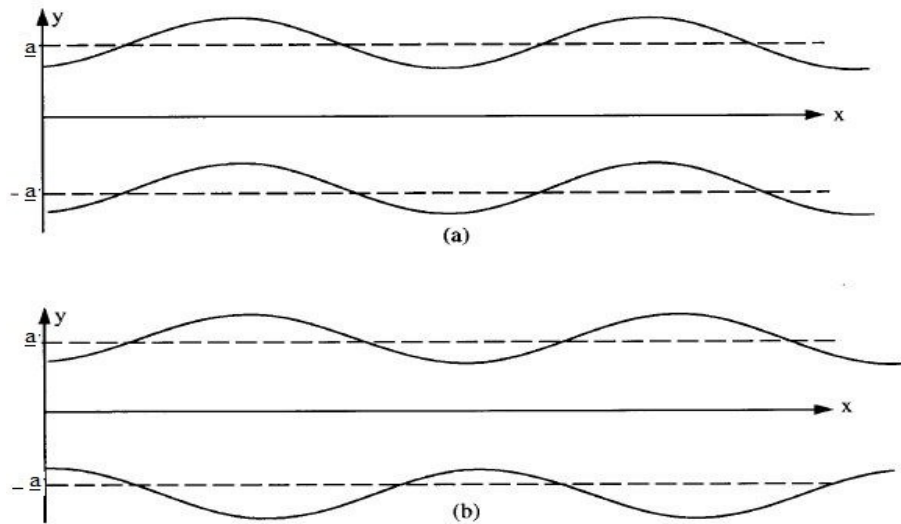


Figure 2-1 One dimensional representation of symmetric(a) and antisymmetric instabilities (b)

A two-dimensional, viscous, incompressible liquid sheet of thickness $2a$, moving with velocity U in a gaseous medium with velocity U_G is considered. The surrounding gas is modelled as inviscid and incompressible.

The schematized liquid sheet is shown in the Figures 2-2.

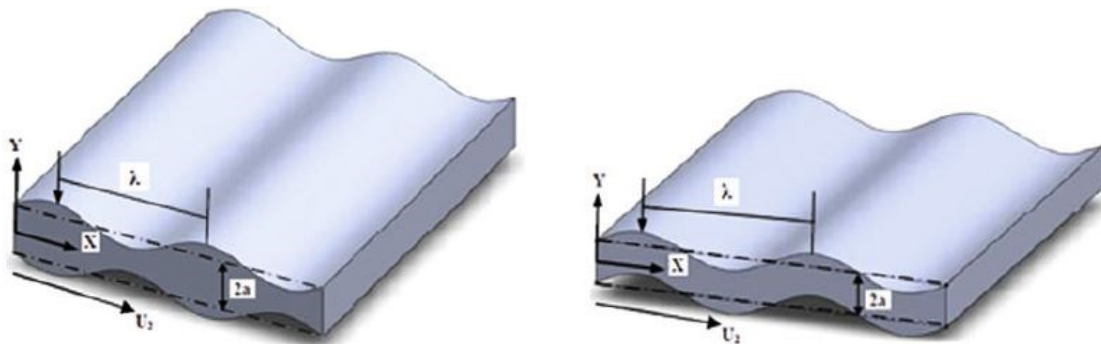


Figure 2-2- Varicose wave (left) and sinusoidal wave (right) [3]

The coordinate system is set up so that the x-axis is parallel to the direction of the sheet relative velocity U_0 , the y-axis is perpendicular to the x one and the origin of the system is located at the mid-plane of the sheet.

A spectrum of infinitesimal disturbances is imposed on the initially steady motion of the sheet [5]. The disturbance is written as:

$$\eta = \Re[\eta_0 * e^{(i*k*x + \omega*t)}] \quad (2.1)$$

where η_0 is the initial wave amplitude, ω is the complex wave growth rate, and k is the wave number. This is the sum of a real component and an imaginary one:

$$\omega = \omega_r + i\omega_i \quad (2.2)$$

The real part represents the growth rate of wave perturbation while the imaginary part denotes the wave velocity.

The most unstable disturbance, responsible of the breakup, occurs when the growth rate reaches its highest value, Ω_s , at the corresponding wave number K_s . The mathematical dissertation finds a dispersion relation $\omega = \omega(k)$, necessary to evaluate the maximum growth rate at the breakup time. The linearized liquid continuity and momentum equations have to be resolved. In order to simplify them, cylindrical coordinates are used. According to capillary instability of free liquid jets theory, small perturbation in velocity, pressure and radius of jet can be considered.

Therefore, these quantities are written as:

$$u = \bar{u} + u' \quad (2.3)$$

$$v = \bar{v} + v' \quad (2.4)$$

$$p = \bar{p} + p_L' \quad (2.5)$$

$$R_j = R_{un} + \xi \quad (2.6)$$

where, \bar{u}, \bar{v} , and \bar{p} are the mean axial velocity, radial velocity and pressure; R_{un} is the unperturbed radius and ξ is the small surface perturbation; u', v' and p' are the fluctuating components of respective quantities. All of them are referred to the liquid, assuming the gas effects can be neglected. For this system, the linearized liquid continuity and momentum equations are:

$$\nabla \cdot \underline{u}' = 0 \quad (2.7)$$

$$\frac{\partial u'}{\partial t} = -\frac{1}{\rho} \frac{\partial p'}{\partial x} \quad (2.8)$$

$$\frac{\partial v'}{\partial t} = -\frac{1}{\rho} \frac{\partial p'}{\partial r} \quad (2.9)$$

$$\frac{1}{r} \frac{\partial r v'}{\partial r} + \frac{\partial u'}{\partial x} = 0 \quad (2.10)$$

The boundary conditions are imposed at the interface between the liquid and the gas. They are the kinematic free surface condition, continuity of shear stress and continuity of normal stress, and are respectively written as:

$$v'_L = \frac{\partial \eta}{\partial t} \quad (2.11)$$

$$\frac{\partial v'_{L}}{\partial x} = -\frac{\partial u'_{L}}{\partial r} \quad (2.12)$$

$$-p'_L + 2\mu_L \frac{\partial v'_{L}}{\partial r} + p'_G = \sigma \frac{\partial^2 \eta}{\partial x^2} \quad (2.13)$$

where σ_L is liquid surface tension, p'_G is the fluctuating pressure for gas.

In order to resolve these Equations, the velocities are written as sum of two components, according to the Helmholtz decomposition. It is also known as the fundamental theorem of vector calculus and states that a

three-dimensional vector field can be resolved as an irrotational vector field plus a solenoidal one. Therefore, the velocity components became:

$$u'_L = u'_I + u'_R = \frac{\partial \phi_L}{\partial x} - \frac{\partial \psi_L}{\partial y} \quad (2.14)$$

$$v'_L = v'_I + v'_R = \frac{\partial \phi_L}{\partial y} + \frac{\partial \psi_L}{\partial x} \quad (2.15)$$

The subscript I indicates the irrotational components; at the same way, R indicates the solenoidal parts which include the effect of viscosity. Φ_L and ψ_L are the velocity potential and the stream functions, respectively. Both depend on wave number and disturbance growth rate.

$$\phi_L = \varphi(y) \exp(ikx + \omega t) \quad (2.16)$$

$$\psi_L = \chi(y) \exp(ikx + \omega t) \quad (2.17)$$

2.2.2 Inviscid liquid sheet

The solution of Navier Stokes equations for an inviscid sheet and sinuous mode the solution is:

$$\omega^2 (\tanh(ka) + \xi) + \omega 2ikU - \xi U^2 k^2 + \frac{\sigma_L k^3}{\rho_L} = 0 \quad (2.18)$$

And for the varicose mode is:

$$\omega^2 (\coth(ka) + \xi) + \omega 2ikU - \xi U^2 k^2 + \frac{\sigma_L k^3}{\rho_L} = 0 \quad (2.19)$$

Where $\xi = \rho_g / \rho_L$.

Therefore, the wave growth rate for both modes are, respectively:

$$\omega_r = \frac{\sqrt{\tanh(ka) \xi U^2 k^2 - \sigma_L k^3 / \rho_L (\tanh(ka) + \xi)}}{\tanh(ka) + \xi} \quad (2.20)$$

$$\omega_r = \frac{\sqrt{\coth(ka) \xi U^2 k^2 - \sigma_L k^3 / \rho_L (\coth(ka) + \xi)}}{\coth(ka) + \xi} \quad (2.21)$$

It is recognized that for ξ values significantly less than one, the sinuous mode is dominant [5], [60].

A critical Weber number is derived from observation of wave growth rate. It represents the transition from long to short waves. The long waves are dominant at low sheet velocity, differently from the short ones. The critical Weber is estimated equal to 27/16. For lower Weber values, long waves have to be regarded, for higher values short waves are dominant. This differentiation is used to simplify the wave growth rate Equation. This is shown in the diagram in Figure 2-3.

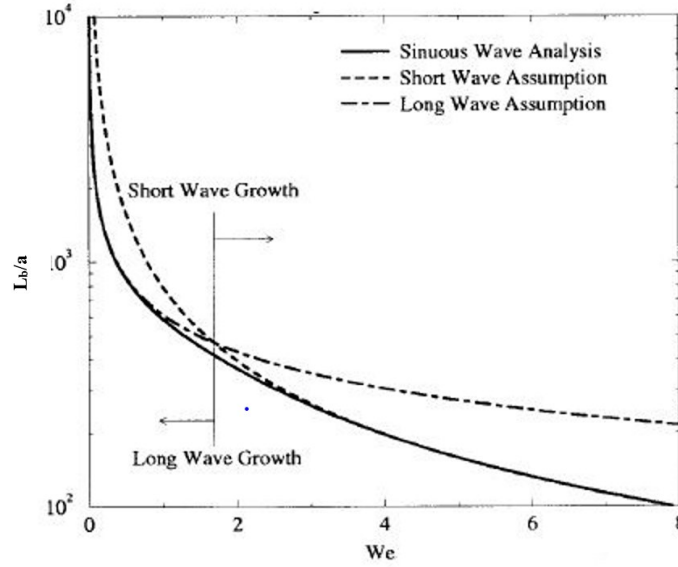


Figure 2-3-Critical Weber number for sinuous long and short waves

On the ordinate axis there is a dimensionless length evaluated by the ratio of breakup length, L_b , to sheet thickness, a . It is plotted against the Weber number for sinuous long and short waves. The point at which the breakup length is the same for short and long waves represents the critical or cut-off Weber number. For Weber numbers above this value, the short waves approximation is in good agreement with the sinuous general Equation. This agreement is respected by the long waves for weber values lower than the critical one. Indeed, if the maximum dimensionless wave growth rate for long waves, calculated as:

$$\left(\frac{\Omega_s a}{U}\right)_{long} = \frac{1}{2} \sqrt{\xi W_e} \quad (2.22)$$

It is matched with the same value calculated for short waves

$$\left(\frac{\Omega_s a}{U}\right)_{short} = \frac{2}{3} W_e \sqrt{\frac{\xi}{3}} \quad (2.23)$$

the critical value of Weber number is found to be 27/16 [5].

If long waves are assumed, then the quantity $\tanh(ka)$ is approximately equal to the product ka and the Equation (2.21) becomes:

$$\omega_r = \frac{\sqrt{a\xi U^2 k^3 - \sigma_L k^3 / \rho_L (ka + \xi)}}{ka + \xi} \quad (2.24)$$

A further simplification is available, if $\xi \ll kh$. In that case, it is allowed to write:

$$\omega_r = \sqrt{\frac{\xi U^2 k^2 - \xi \sigma_L k^3 / \rho_L}{ka}} \quad (2.25)$$

If short waves are assumed, then $\tanh(ka) = \coth(ka) = 1$, both Equations (2.23) and (2.24) can be written as:

$$\omega_r = \frac{\sqrt{\xi U^2 k^2 - \sigma_L k^3 / \rho_L (1 + \xi)}}{1 + \xi} \quad (2.26)$$

If $\xi \ll 1$:

$$\omega_r = \sqrt{\xi U^2 k^2 - \sigma_L k^3 / \rho_L} \quad (2.27)$$

By comparison of Equations (2.26) and (2.27), it can be deduced that a relation exists among the maximum wave growth rate of long and short waves. Indeed, $\omega_{r,short} = \sqrt{k a} \omega_{r,long}$: short waves dominate only if the product ka is less than 1. It coincides with the ratio $\lambda/a < 2\pi$, where λ is the wavelength. In Figures 2-4 and 2-5, this proportion is evident. On the y-axis is plotted the ratio between the product of wave growth rate and sheet thickness to relative velocity: on x-axis is reported the product between wave number and sheet thickness.

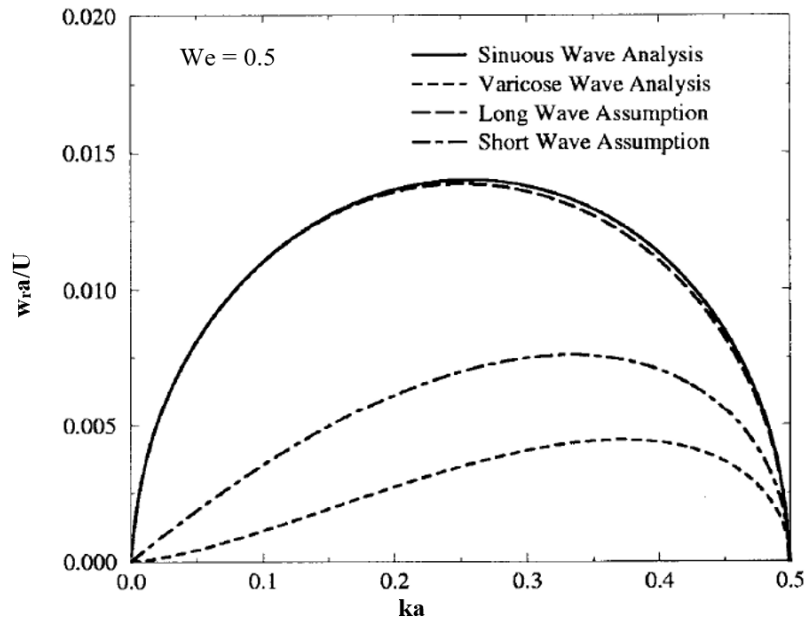


Figure 2-4- Sinuous and varicose waves for inviscid liquid sheet at Weber number = 0.5

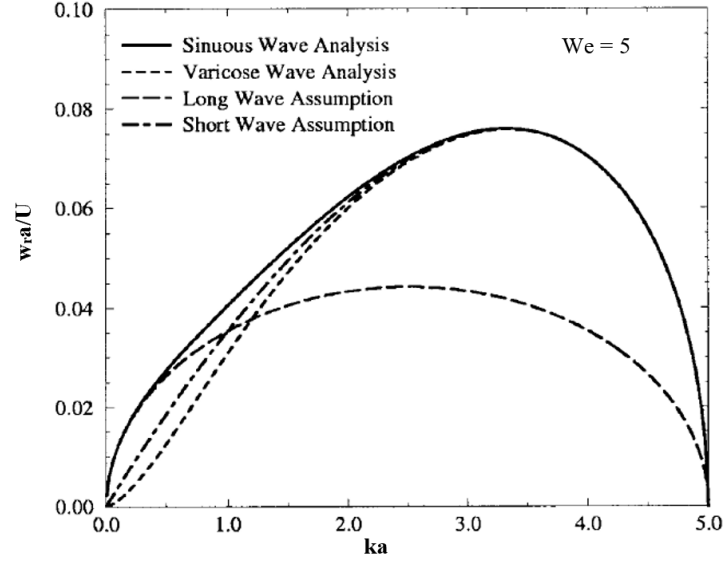


Figure 2-5-- Sinuous and varicose waves for inviscid liquid sheet s at Weber number = 5

For higher Weber numbers, the gap between the maximum wave rate for sinuous mode and the equivalent for varicose mode becomes larger.

2.2.3 Viscous liquid sheet

In the previous dispersion relation, the effect of viscosity is not considered. It is assumed the stress is one-dimensional, in other words there is no variation in y -direction [5]. The shear stress is given by:

$$\tau_{xy} = \mu_L \left(\frac{\partial v}{\partial x} \right) \quad (2.28)$$

The assumption of an inviscid system implies that the shear stress is zero at gas/liquid interfaces. Thus, the Equations (2.23) and (2.24) are inconsistent when viscosity effect is included.

For the sinuous mode, the dispersion relation found is:

$$\omega_r = -\frac{2v_L k^2 \tanh(ka)}{\tanh(ka) + \xi} + \frac{\sqrt{4v_L^2 k^2 \tanh^2(ka) - \xi^2 U^2 k^2 - [\tanh(ka) + \xi](-\xi U^2 k^2 + \sigma_L k^3 / \rho_L)}}{\tanh(ka) + \xi} \quad (2.29)$$

where v_L is the axial component of the velocity U :

$$v_L = U \cos \theta \quad (2.30)$$

For long waves and assuming that $\xi \ll ka$, the Equation (2.28) becomes:

$$\omega_r = -2v_L k^2 + \sqrt{4v_L^2 k^2 + \frac{\xi U^2 k}{a} - \frac{\sigma_L k^2}{\rho_L a}} \quad (2.31)$$

For short waves, the Equation (2.55) is simplified:

$$\omega_r = -2v_L k^2 + \sqrt{4v_L^2 k^4 + \xi U^2 k^2 - \frac{\sigma_L k^2}{\rho_L}} \quad (2.32)$$

The same Equations can be written for the varicose mode by substituting $\tanh(ka)$ with $\coth(ka)$. It is evident from the Figures 2-6 and 2-7 that the inclusion of viscosity in the dispersion model reduced both the maximum value of wave growth rate and the corresponding wave number.

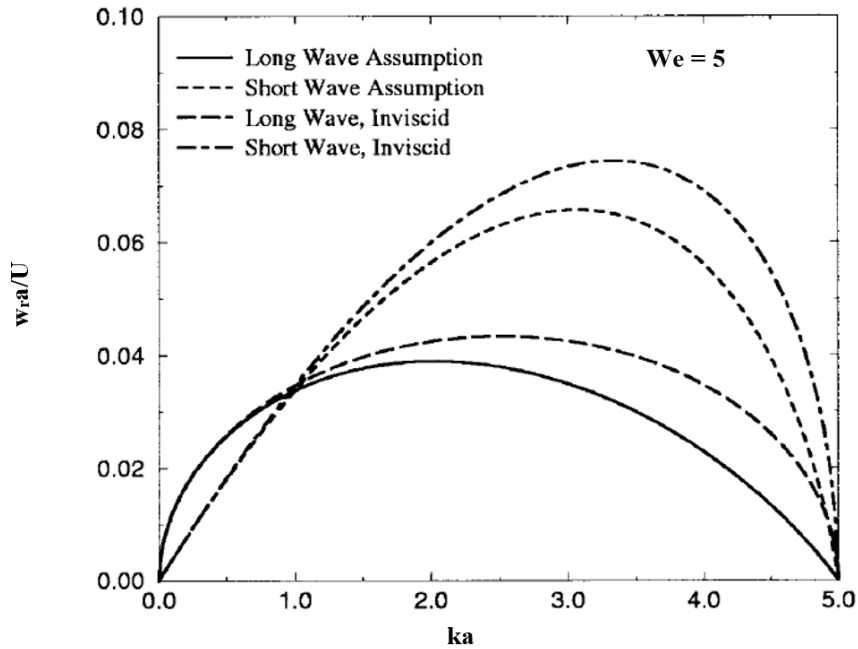


Figure 2-6--Sinuous long and short waves for viscous liquid sheet at $We= 5$

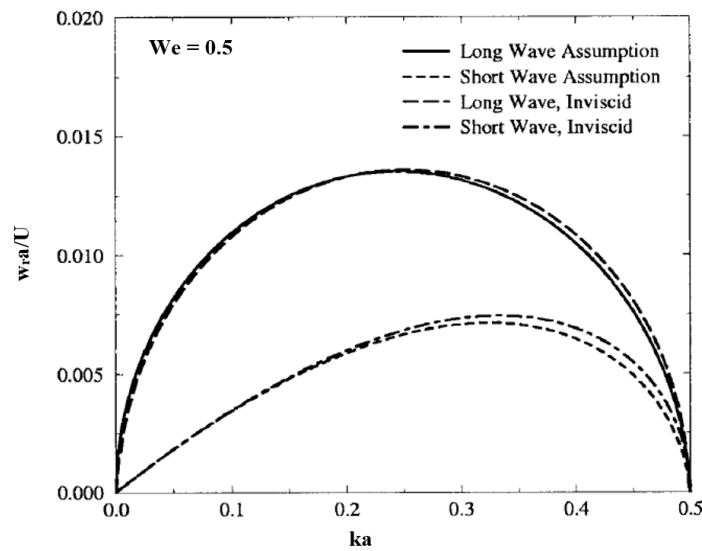


Figure 2-7- Sinuous long and short waves for viscous liquid sheet at $We= 0.5$

2.2.4 Primary atomization

The wave growth rate Equation (2.19) or (2.20) or (2.29) represents the initial instability. The wave grows until to reach a critical wavelength at which the sheet breaks at half wavelength intervals into ligaments; these break in large droplets, according to Weber 's theory of cylindrical liquid column. This first phase is called

primary atomization. The relations employed to evaluate the diameter of primary droplets are obtained starting from a force balance on an element of wavy sheet. The element is given by:

$$dV=2a(x) \cdot z \cdot dx \quad (2.33)$$

The schematic sheet which these balances are based on is in Figure 2-8.

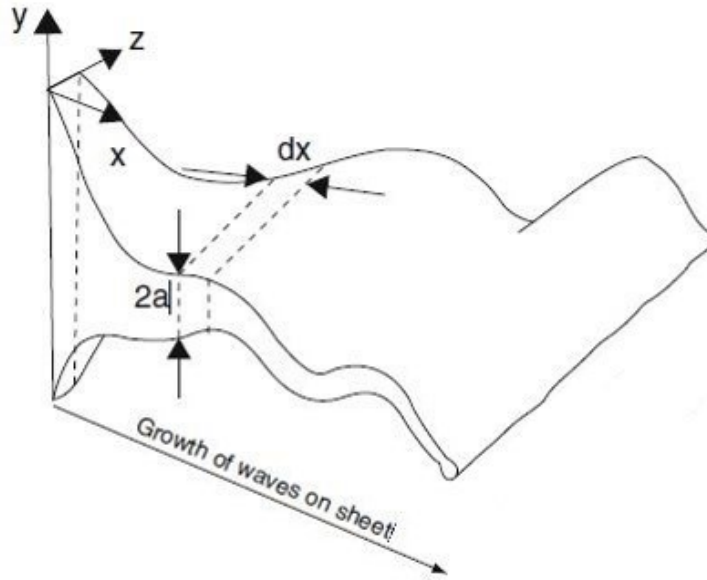


Figure 2-8- Wavy sheet scheme and coordinate system

The forces acting on wavy sheet are the total air pressure force, the one caused by the surface tension, the inertial force and the viscous force [61]. They are written as:

$$F_p = 2\rho_L k U_0^2 y z dx \quad (2.34)$$

$$F_s = 2\sigma_L z \frac{\partial^2 y}{\partial x^2} \quad (2.35)$$

$$F_I = -\frac{\partial}{\partial z} \left(\rho_L z (2a) dx \frac{\partial y}{\partial t} \right) = -\rho_L \left(2a \frac{\partial^2 y}{\partial t^2} + \frac{\partial(2a)}{\partial t} \frac{\partial y}{\partial t} \right) z dx \quad (2.36)$$

$$F_\mu = \mu_L (2a) k^2 \frac{\partial h}{\partial t} \sin(kx + \beta) - \frac{\mu_L k}{U} \frac{\partial(2a)}{\partial t} \frac{\partial h}{\partial t} \cos(kx + \beta) \quad (2.37)$$

where β is the phase angle, U_0 is the relative velocity between the sheet and the gas and it is assumed to be equal to the liquid velocity near the injection exit U ; h is the wave amplitude and it is given by:

$$h = a + v \quad (2.38)$$

For a constant velocity thinning sheet, the product $2a$ can be written as:

$$2a = C_t * t^{-1} \quad (2.39)$$

where C_t is a constant

The force F_p is regarded as the sum of the pressure forces acting on the upper and the lower surfaces of the sheet. The same criterion is applied for the surface force. The ratio of the maximum value of the first term in viscosity force Equation (2.36) to the maximum value of the second term in the same Equation is the wave number k . For high enough k values, the second term may be neglected.

The total force operating on dx is:

$$F_p + F_s + F_l + F_\mu = 2\rho_L k U_0^2 y z dx + 2\sigma_L z \frac{\partial^2 y}{\partial x^2} - \rho_L \left(2a \frac{\partial^2 y}{\partial t^2} + \frac{\partial(2a)}{\partial t} \frac{\partial y}{\partial t} \right) z dx + \mu_L (2a) \frac{\partial^3 y}{\partial x^2 \partial t} z dx = 0 \quad (2.40)$$

It can be rewritten as:

$$2\rho_G k U^2 y + 2\sigma_L \frac{\partial^2 y}{\partial x^2} - \rho_L \left(2a \frac{\partial^2 y}{\partial t^2} + \frac{\partial 2a}{\partial t} \frac{\partial y}{\partial t} \right) z dx + \frac{\mu_L 2a \partial^3 y}{\partial t \partial^2 x} x dz = 0 \quad (2.41)$$

Or in terms of h :

$$2\rho_G k U^2 h + 2\sigma_L k^2 h - \rho_L \left(2a \frac{\partial^2 h}{\partial t^2} + \frac{\partial 2a}{\partial t} \frac{\partial h}{\partial t} \right) - \mu_L 2a k^2 \frac{\partial h}{\partial t} = 0 \quad (2.42)$$

A further substitution is undertaken. In fact, h is expressed as a function of a parameter f , defined as the breakup parameter, since it determines when it occurs.

$$h = h_0 \exp(f) \quad (2.43)$$

or, in the same way:

$$f = \ln \left(\frac{h}{h_0} \right) \quad (2.44)$$

where h_0 is the initial value of h .

A deep investigation made by Weber in 1931, has revealed that in the greatest majority of investigation, the mean value of f is 12 [3], [62]. It may be estimated by a correlation based on Reynolds and Weber number, expressed as function of injection velocity from the nozzle, nozzle diameter and liquid properties

$$f = R_e^{0.07} W_e^{0.37} \quad (2.45)$$

Once the wave growth rate reaches its critical amplitude, the sheet breaks into cylindrical ligaments of liquid, the surface tension forces them to become unstable and then to breaks into droplets, as its showed in the Figure 2-9. It has long been recognized that the thickness of the annular liquid film has a strong influence on the mean drop size of the spray. Therefore, it is possible to consider this parameter to analyse sprays performances.

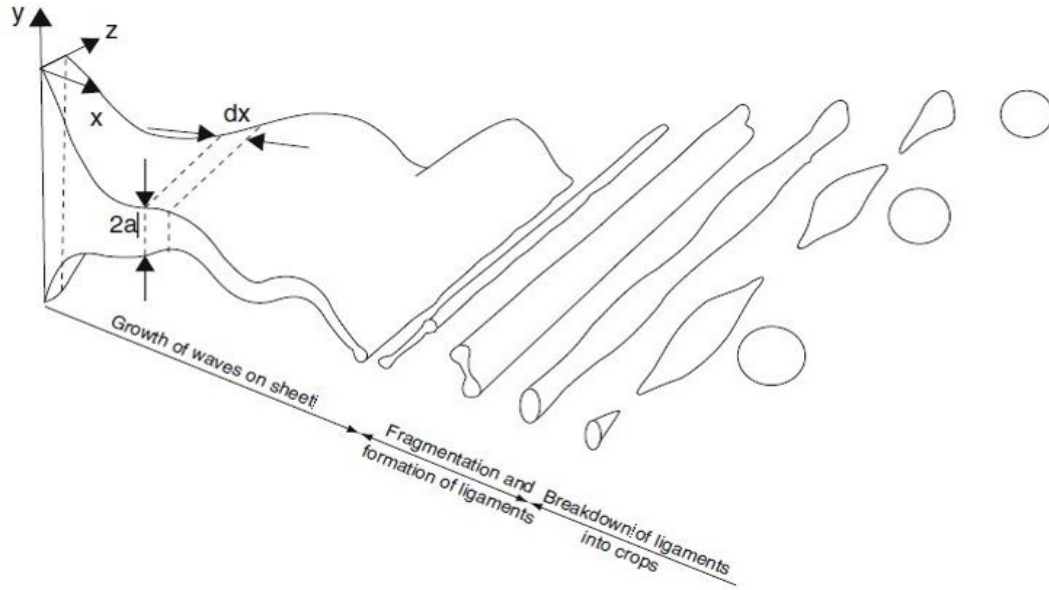


Figure 2-9-Lisa model of sheet primary atomization [61]

The breakup time is evaluated as:

$$T_d = \frac{1}{\omega_{max}} * f \quad (2.46)$$

And the breakup length is expressed as:

$$L_b = U * T_d \quad (2.47)$$

The sheet half-thickness at the breakup length is:

$$a_b = \frac{2a_0(d_0 - a_0) / \cos \theta}{2L_b + d_0 - h_0} \quad (2.48)$$

where θ is the half-angle of spray [3]. The initial sheet thickness a_0 is estimated through the Lefebvre's theory [8], applied on pressure-swirl atomizers. These have a circular outlet orifice preceded by a swirl chamber into which liquid flows through a number of tangential holes. The swirling liquid creates a core of air or gas that extends from the discharge orifice to the rear of swirl chamber. The liquid emerges from the discharge orifice as an annular sheet, which spreads radially outward to form a hollow conical spray. The thickness is directly related to the area of the air core. The relationship between atomizer dimensions and the size of air core is:

$$\left(\frac{A_p}{D_s d_0} \right)^2 = \frac{\pi^2 (1-X)^3}{32 X^2} \quad (2.49)$$

where A_p is the total inlet area, D_s is the swirl chamber diameter. From this relation, X is evaluated. The corresponding value of liquid film thickness a_0 can be derived from geometric considerations:

$$X = \frac{(d_0 - 2a_0)^2}{d_0^2} \quad (2.50)$$

The ligaments diameter is given by the relation:

$$d_L = \sqrt{\frac{16a_b}{k_{max}}} \quad (2.51)$$

where k_{max} is the wave number corresponding to the maximum wave growth rate (K_S). The ligaments break when the unstable waves reach an amplitude equal to their radius. The droplet diameter is calculated as:

$$d_D = 1.88d_L(1 + 3Oh)^{1/6} \quad (2.52)$$

where Oh is the Ohnesorge number which represents the ratio of drop viscous forces to the surface tension ones:

$$Oh = \frac{\sqrt{We}}{Re} = \frac{\mu_L}{\sqrt{\rho_L \sigma_L d_L}} \quad (2.53)$$

It has to be specified that this value is the mean diameter of a Rosin-Rammler distribution.

2.2.5 Secondary atomization

The formed droplets break into smallest fragments due to disruptive aerodynamic forces. This process is termed secondary atomization. The ratio between the aerodynamic force and the stabilizing surface tension force is the dimensionless Weber number:

$$We = \frac{\rho_G d_D U^2}{\sigma_L} \quad (2.54)$$

The larger the Weber number, the higher tendency to breakup. Drop viscosity obstructs the deformation, just like the surface tension force. These two factors are enclosed in the dimensionless Ohnesorge number.

The physical properties refer to the drops' ones. For $Oh < 0.1$, experimental tests determined that the secondary breakup process is independent of Oh number. In this case, the different breaking modes are studied as function of Weber number [63], as listed in Figure 2-10.

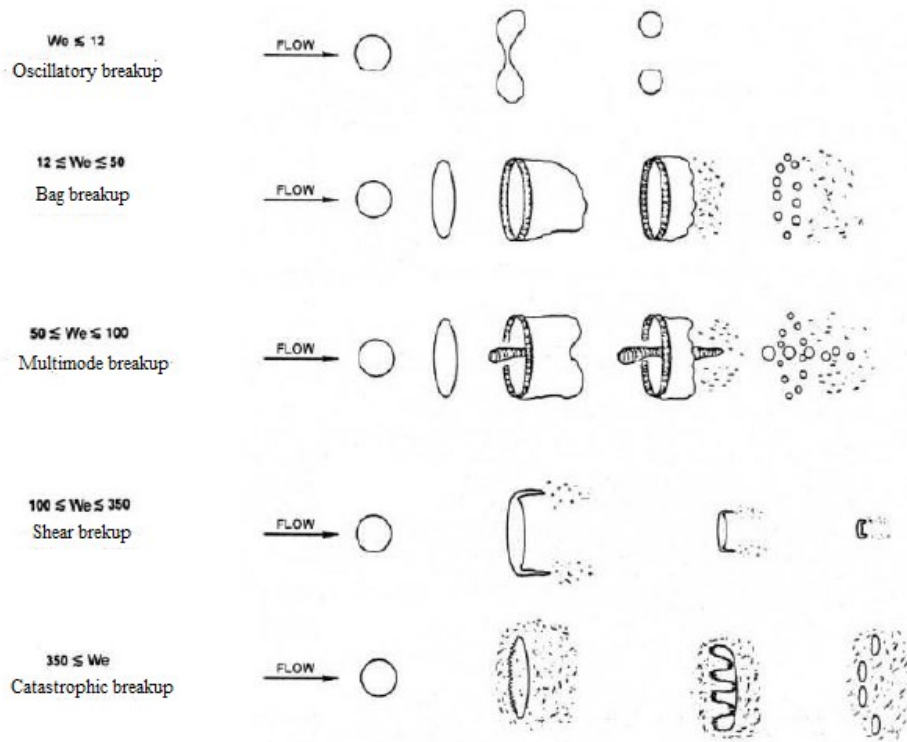


Figure 2-10- Different secondary atomization breakup modes at different Weber numbers [63]

The value of We that demarks each breakup mode is referred to a transitional Weber number. The diagram in Figure 2-11 shows the different breaking modes depending on both dimensionless numbers and for different liquids.

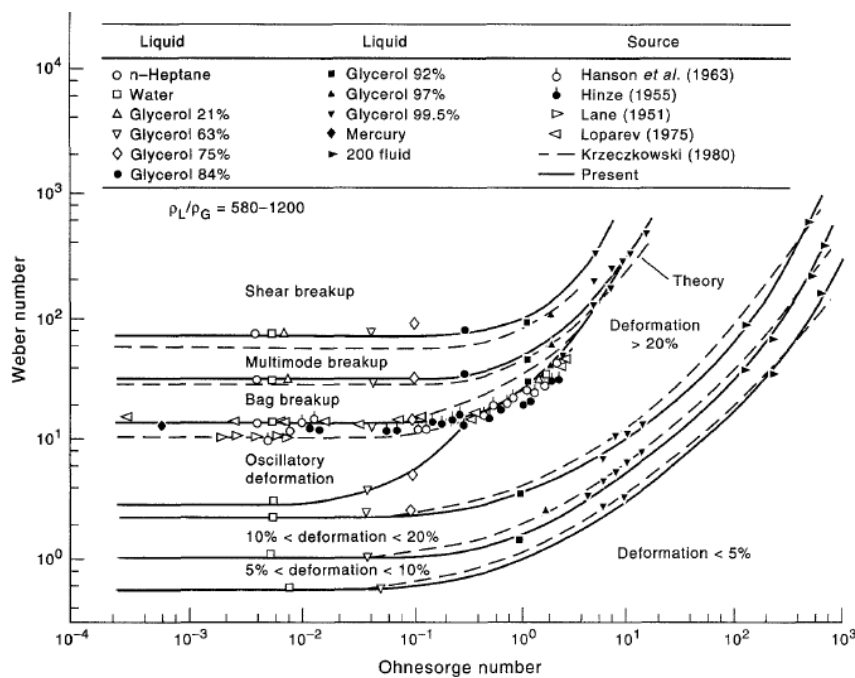


Figure 2-11- Secondary atomization modes as function of Weber and Ohnesorge numbers [63]

After the primary breakup, at low Weber number, a vibrational breakup mode takes place and a spherical drop is subjected to a shape deformation due to an unequal static pressure distribution over its surface. This leads

to drop oscillations similar to the disturbances described for the liquid sheet. These oscillations may cause the breakup into a few large drop fragments. This mode occurs more slowly than the other ones and it does not produce small and fine droplets. Therefore, it is often ignored, and the bag mode is regarded as the first mode of the [64] secondary atomization.

In the *bag breakup mode*, around the deformed drop, there is a positive pressure difference between the leading stagnation point and a wave zone due to the separation of the flow. This blows the centre of the drop downstream and forms a toroidal ring to which a bag is attached [65]. The bag blows up into fine fragments and in the same way acts the ring forming larger fragments. It has experimentally noted that the diameter of droplets formed by the ring fragmentation was 30 % of the original droplets dimension. On the contrary, for the fragments formed by the bag disruption, the diameter was 4% of the starting one.

The *sheet thinning breakup mode* occurs at high velocities. A sheet, formed around the drop surface because of ambient phase inertia, is perturbed and breaks into ligaments and these into a multitude of small droplets [66]. This secondary atomization can be deliberated finished when the velocity of drops is high enough to consider the aerodynamic force negligible. In this case, a core drops remains at the end of the atomization.

The *multimode breakup mode* appears at *We* numbers between those typical of bag mode and those of sheet thinning breakup; it may be studied as a combination of the two modes. Among various structure observed for this breaking mode, one of them is mostly frequent: there is a bag formation and the presence of a core drop, which leads to the formation of a long ligament in the centre of the bag similar to a plume [65].

At extremely high velocities, it was observed the formation and growth of unstable waves on leading drop surfaces. The waves may penetrate the drop causing its breakup into fine drops. This mode is denoted as *catastrophic breakup mode* and it is limited into practical applications because of too high values of relative velocity at which takes place.

2.3 Theory of Electrohydrodynamic

Electro-hydrodynamics (EHD) or electro-fluid-dynamics is the study of an electrically charged fluid. The EHD theory deals with the interaction between ions or particles immersed in a fluid and the surrounding electric field [54] and aims to describe the relationship between the electric and hydrodynamic forces [38].

The Maxwell's Equations describes the electromagnetic phenomena of EHD [38]. The general Equations for a linear and isotropic system are:

$$\nabla \times \mathbf{E} = -\frac{\partial \mu_m H_m}{\partial t} \quad (2.55)$$

$$\nabla \times \mathbf{H}_m = J_c + \frac{\partial \epsilon_r E}{\partial t} \quad (2.56)$$

$$\nabla \cdot \mathbf{D} = q \quad (2.57)$$

where μ_m is the magnetic permittivity, ε_r is the electric permittivity, both assumed constant; \mathbf{J}_c is the current density, \mathbf{H}_m and \mathbf{E} are, respectively, the magnetic and the electric field, \mathbf{D} is the electric displacement vector, q is the droplet charge. If the magnetic field can be neglected ($\mathbf{H}_m=0$), \mathbf{E} is irrotational and conservative, the Equation (2.55) can be written as:

$$\nabla \times \mathbf{E} = 0 \quad (2.58)$$

The electric field can be written as:

$$\mathbf{D} = \varepsilon \mathbf{E} \quad (2.59)$$

Where ε is the dielectric permittivity.

According to Gauss' theory, the relation between \mathbf{E} and the total charge density is given by:

$$\varepsilon_0 \nabla \cdot \mathbf{E} = q \quad (2.60)$$

where ε_0 is the vacuum permittivity. In Equation (2.60), the electric field is evaluated in a generic point, and q is regarded as a continuous and uniform charge distribution depending on position $q=q(r)$.

The function electric potential V can be defined by the relation:

$$\mathbf{E} = -\nabla V \quad (2.61)$$

By combination of Equation 2.60 and 2.61, it can be written:

$$\nabla \cdot \nabla V = -\nabla \cdot \mathbf{E} = -\frac{q}{\varepsilon_0} = \Delta V \quad (2.62)$$

Where Δ is the Laplace operator ($\Delta=\nabla^2$).

Following the Gauss theorem, the total charge Q may be expressed as the flux of electric field through a closed surface of volume V :

$$Q = \oint \varepsilon_0 \mathbf{E} dS = \iiint q dV \quad (2.63)$$

where q can be expressed as function of vector \mathbf{D} through Equation (2.57).

If the total charge is not constant during the time, its rate of change is equal to current density \mathbf{J}_c in a volume V . The relation between \mathbf{J}_c and Q is expressed as:

$$\frac{\partial Q}{\partial t} = -\oint \mathbf{J}_c dA \quad (2.64)$$

The second term can be rewritten regarding the charge conservation relation or Gauss' theorem:

$$\oint_S \mathbf{J}_c dA = \oint_V \nabla \cdot \mathbf{J}_c \quad (2.65)$$

Therefore, the Equation (2.64) can be written as:

$$\frac{\partial Q}{\partial t} + \oint_V \nabla \cdot \mathbf{J}_c = 0 \quad (2.66)$$

The current density is related to electric field through the conductivity as:

$$\mathbf{J}_c = \sigma \mathbf{E} \quad (2.67)$$

For a moving fluid, the Equation (2.67) requires the addition of a convective term to account for the convective motion at velocity \mathbf{U} . The Equation (2.67) becomes:

$$\mathbf{J}_c = \sigma \mathbf{E} + q \mathbf{U} \quad (2.68)$$

The transport Equation of charges in a moving fluid is obtained by coupling Equation (2.66), (2.64) and (2.60):

$$\frac{\partial q}{\partial t} + \nabla \cdot (q \mathbf{U}) + \frac{\sigma}{\varepsilon_r} q = 0 \quad (2.69)$$

The Equation (2.68) defines the relaxation time τ , which is a fundamental parameter to characterize the charging process of a liquid:

$$\tau = \frac{\sigma}{\varepsilon_r} \quad (2.70)$$

Indeed, it describes how fast the charge is transferred to liquid surfaces exposed to a certain electric field.

The mass balance on liquid and its conservation Equation are:

$$\frac{\partial \rho_L}{\partial t} + \rho_L (\nabla \cdot \mathbf{U}) = 0 \quad (2.71)$$

Which for a non-compressible fluid becomes :

$$\nabla \cdot \mathbf{U} = 0 \quad (2.72)$$

The conservation of momentum is expressed as:

$$\rho_L \frac{\partial \mathbf{U}}{\partial t} = \nabla \cdot (\mathbf{T}^m + \mathbf{T}^e) + \mathbf{F}_G \quad (2.73)$$

where \mathbf{F}_G is the body force or gravity, \mathbf{T}^m is the mechanical stress tensor and \mathbf{T}^e is the electrical stress tensor.

The former is the sum of a pressure term and a viscous one [38]:

$$\mathbf{T}^m = -p \mathbf{I} + 2\mu_L \left[\frac{1}{2} (\nabla \mathbf{U} + (\nabla \mathbf{U})^T) \right] \quad (2.74)$$

where \mathbf{I} is the identity tensor.

The divergence of mechanical tensor for Newtonian fluids is expressed as:

$$\nabla \cdot \mathbf{T}^m = -\nabla p + \mu_L \nabla^2 \mathbf{U} \quad (2.75)$$

By substituting Equation (2.75) in Equation (2.73), the Navier-Stokes Equation is found:

$$\rho_L \frac{\partial \mathbf{U}}{\partial t} = -\nabla p + \mu_L \nabla^2 \mathbf{U} + \rho \mathbf{g} \quad (2.76)$$

Concerning the electrical stress tensor, it is written as [38]:

$$\mathbf{T}^e = \varepsilon_r \mathbf{E} \mathbf{E} - \frac{1}{2} \varepsilon_r (1 - s) E^2 \mathbf{I} \quad (2.77)$$

s is a scalar parameter defined as:

$$s = \frac{\rho}{\varepsilon_r} \left(\frac{\partial \varepsilon_r}{\partial \rho} \right)_T \quad (2.78)$$

The divergence of \mathbf{T}^e can be read as a volumetric force \mathbf{f}_e :

$$\mathbf{f}_e = \nabla \cdot \mathbf{T}^e = q\mathbf{E} - \frac{1}{2}E^2\nabla\varepsilon_r + \frac{1}{2}\nabla\varepsilon_r s E^2 \quad (2.79)$$

The force \mathbf{f}_e is added at Navier-Stokes Equation and, by expressing s as in Equation (2.78), this becomes:

$$\rho_L \frac{\partial \mathbf{U}}{\partial t} = -\nabla p + \mu_L \nabla^2 \mathbf{U} + q\mathbf{E} - \frac{1}{2}E^2\nabla\varepsilon_r + \frac{1}{2}\nabla \left(\rho \left(\frac{\partial \varepsilon_r}{\partial \rho} \right)_T E^2 \right) + \rho \mathbf{g} \quad (2.80)$$

The Equation (2.80) is the momentum balance of a linear dielectric fluid in an electric field. It couples the electric field and the fluid dynamics, showing the governing force of fluid deformation caused by E [38]. The term $q\mathbf{E}$ is the Coulomb force, which acts on the fluid charges in the fluid. These become accelerated by the Columbian force and deform the fluid. The term $\frac{1}{2}E^2\nabla\varepsilon_r$ is the dielectric force on polarised charges and it represents the spatial variation of permittivity, which has to be regarded only if the fluid is not isotropic and incompressible. Otherwise, the permittivity has no gradient. The last term of the electric tensor contributes in Equation (2.78) is called electro-restrictive pressure force. It is caused by inhomogeneity of electric field and it has to be taken into account for compressible fluid. Therefore, for a Newtonian, isotropic and incompressible fluid at constant ε_r , the Equation (2.80) is simplified as:

$$\rho_L \frac{\partial \mathbf{U}}{\partial t} = -\nabla p + \mu_L \nabla^2 \mathbf{U} + q\mathbf{E} + \rho \mathbf{g} \quad (2.81)$$

The Equation (2.80) coupled with Eq. (2.68) models the fluid dynamic of a liquid jet under the influence of an electric field. The solution is not simple, and few solutions can be found by CFD simulations made on liquid jets produced by Electrospray [22][55]. While Eq. (2.80) was used to describe low flow rate jets breakup, its application to large glow rate swirl atomizers is far from being achieved.

In this case, the electrification of hydraulic nozzles by induction charging is more complicated due to the complexity of atomization mechanism for that geometry. For this reason, the induction charging mechanism of a hydraulic jet is modelled by assuming a simplified breakup model that is not realistic. It has been done by Artana et al. [51] and revised by Cross et al. [56] and it is described in section 2.4.

2.4 Simplified model of induction charging

The induction charging mechanism was theoretically described by Artana et al. [51]. The model assumes that the shear stresses caused by the aerodynamic interaction between liquid and surrounding air creates a cylindrical sheet exiting from the nozzle. At breakup point, a ring of liquid is going to detach from the sheet and breaks into droplets, when it becomes highly unstable because of liquid-gas relative velocity. In contrast with the LISA model theory, a constant sheet thickness value is considered for simplicity. Indeed, this model does not take into account the disturbance on liquid jet caused by a wavy instability. This theoretical model assumes there is no influence of the electrostatics on the fluid dynamic process. This assumption is supported

by the experimental analysis of charged and uncharged droplets diameter for which no marked difference has been noted [51]. Furthermore, the droplets carry the same charge accumulated in the ligament, and so the electric charge is not influenced by droplet diameter. The induction charging model aims to describe the process in terms of droplet charge to mass ratio. There are two possible mathematical approaches to estimate it: i) taking in exam the equations of an RC electrical circuit or ii) using Maxwell's equations for an electric field.

The first one considers the system nozzle-HV electrode-liquid as an electrical circuit, as showed in Figure 2-12. The electrical induction charging has a characteristic time proportional to drop formation time or breakup time τ_b . The model description used in this work is the simplified version developed by Cross et al. [56], which removed the original hypothesis that there was a second condenser between the liquid cone and the ligaments detached at the breakup point because physically both points are at the same potential (e.g the ground potential).

In the circuit R is the liquid resistance, B' is the breakup point of liquid jet, B'' is the inlet of liquid spray in the "electrode zone", E is the high voltage electrode, E' is the ground electrode (e.g. the nozzle), V is the high voltage supply and C is the capacity of the condenser that takes place between the HV electrode and the liquid lamina. In Figure 2-12 at right, the experimental setup of high-flow rate sprays is modelled as an electrical circuit, as reported in Chapters 3.

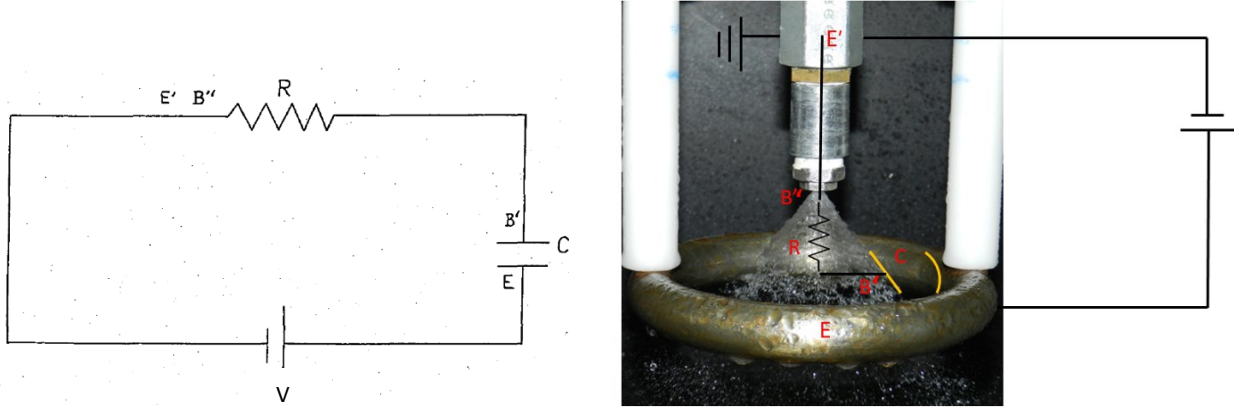


Figure 2-12- Representation of induction charging system as an electrical circuit. Left: model, right: experimental setup

The capacity of the condenser can be estimated as:

$$C = C_j L_j = \frac{2\pi\epsilon_0}{\ln(r_c/r_j)} L_j \quad (2.82)$$

where L_j is the length of liquid film exposed to the electrode, r_c is the electrode radius, r_j is the liquid jet radius at breakup point. The resistance of liquid sheet is expressed as:

$$R = \frac{L_b}{\sigma A_j} \quad (2.83)$$

where A_j is the area of liquid jet.

The charging time in the circuit is defined as:

$$t = \frac{L_j}{U}, \quad 0 < L_j < L_c \quad (2.84)$$

The charging mechanism is time-dependent, and the electrical potential is expressed according to Kirchoff's law:

$$V = iR_j + \frac{q}{C} \quad (2.85)$$

By considering that:

$$i = \frac{dq}{dt} \quad (2.86)$$

The equation (2.86) is written as:

$$V = \frac{dq}{dt} R_j + \frac{q}{C} \quad (2.87)$$

It represents how fast is the charging of a liquid film as a component of an RC circuit. The 1st order differential equation is solved in terms of electric charge q :

$$q = C_1 e^{-t/R_j C} + VC \quad (2.88)$$

where C_1 is a constant that is found by assuming as initial condition that at $t=0$, $q=0$:

$$q = VC \left[1 - \exp\left(-\frac{t}{R_j C}\right) \right] \quad (2.89)$$

where $\tau_c = R_j C$ is the characteristic time of an RC circuit.

The correlation (2.90) is valid only if the liquid jet breakup takes place inside the HV electrode zone or below it. Otherwise, if the liquid breaks before becoming exposed to the electrode, it will not be charged.

By dividing the equation (2.89) by the volume of liquid $V_b = Q_l t = Q_l L_j / U$ and by its density, the droplet charge to mass ratio, $D - CMR_{th-1}$, is obtained:

$$D - CMR_{th-1} = \frac{q}{m_l} = \frac{C_l V}{\rho_l Q_l L_j} \cdot U \cdot \left[1 - \exp\left(-\frac{T_D}{R_l C}\right) \right] \quad (2.90)$$

where R_l is the resistance of liquid lamina and T_d is the droplet time formation (it is coincident with the breakup time τ_b) For a spray, the term T_d/RC is small enough to neglect the exponential term. The simplified equation is:

$$D - CMR_{th-1} = \frac{q}{m_l} = \frac{C_l V}{\rho_l Q_l L_j} \cdot U \quad (2.91)$$

By using the Maxwell's equations, the theoretical Droplet Charge to Mass Ratio D- CMR_{th-2} is expressed as function of electric field and liquid sheet thickness as:

Let \mathbf{H} be a magnetic vector, and \mathbf{D} an electric displacement vector. The model begins from the relation between \mathbf{H} and \mathbf{D} :

$$\text{curl}\mathbf{H} = \mathbf{j}_c + \frac{\partial\mathbf{D}}{\partial t} \quad (2.92)$$

where \mathbf{j}_c is current density.

Then, considering the relation between density current and vector \mathbf{D} , it can be written:

$$\text{div}\mathbf{j}_c = -\text{div}\frac{\partial\mathbf{D}}{\partial t} \quad (2.93)$$

It is also known that:

$$\text{div}\mathbf{j}_c = -\frac{\partial\rho_e}{\partial t} \quad (2.94)$$

where ρ_e is the volume charge density.

Therefore, equalizing (2.93) and (2.94), the relation between ρ_e and \mathbf{D} is found:

$$\frac{\partial\rho_e}{\partial t} = \text{div}\frac{\partial\mathbf{D}}{\partial t} \quad (2.95)$$

The Equation (2.95) becomes fundamental to find a mathematical expression to evaluate the charge Q deposited on the disintegrated liquid volume. It has to be integrated on liquid volume:

$$\int \frac{\partial\rho_e}{\partial t} dV = \int \text{div}\frac{\partial\mathbf{D}}{\partial t} dV \quad (2.96)$$

Transforming the volume integral into a surface one with a cylindrical surface S_l , and a cross surface A , and regarding that the equivalence:

$$j_c dA = -\frac{\partial Q}{\partial t} \quad (2.97)$$

the Q Equation is obtained:

$$\frac{\partial Q}{\partial t} + \frac{\varepsilon_0\varepsilon_r}{\sigma} \frac{\partial^2 Q}{\partial t^2} = \varepsilon_0\varepsilon_a E_r p U_b \quad (2.98)$$

where E_r is the radial electric field that is assumed constant, v is the liquid velocity p is the perimeter of volume cross section, and ε_a is the air relative permittivity which is equal to 1. The perimeter p is calculated as:

$$p = \pi a_j \quad (2.99)$$

where a_j is the thickness of contacted liquid jet.

The Equation (2.95) is integrated for a time as long as T_d , the initial conditions are $t=0$, $Q=0$ and $j=0$. The result of the integration is:

$$Q = \varepsilon_0 E_r p U_b \frac{\varepsilon_0 \varepsilon_r}{\sigma} \left(1 - \exp\left(\frac{-\sigma T_d}{\varepsilon_0 \varepsilon_r}\right) - \frac{-\sigma T_d}{\varepsilon_0 \varepsilon_r} \right) \quad (2.100)$$

The specific charge of a volume V_d is:

$$q_v = \frac{Q}{V_d} = \frac{\varepsilon_0 E_r p \lambda}{V_d} \left\{ \frac{\varepsilon_0 \varepsilon_r}{\sigma T_d} \left(1 - \exp\left(\frac{-\sigma T_d}{\varepsilon_0 \varepsilon_r}\right) \right) - 1 \right\} \quad (2.101)$$

The volume V_d of the liquid is expressed as:

$$V_d = p \lambda' a \quad (2.102)$$

where p is the perimeter of liquid jet and λ' is the length of disintegrated volume, which is assumed to be the same order of magnitude of sheet thickness. λ' and T_d are related by the relation:

$$\lambda' = U_b T_d \quad (2.103)$$

By substituting the correlations (2.101-102) in Equation (2.101) is obtained the second expression for the droplet charge to mass ratio:

$$D - CMR_{th-2} = \frac{\varepsilon_0 E(V)}{a_b} \left\{ \frac{\varepsilon_0 \varepsilon_r}{\sigma T_d} \left(1 - \exp\left(\frac{-\sigma T_d}{\varepsilon_0 \varepsilon_r}\right) \right) - 1 \right\} \quad (2.104)$$

where $E(V)$ is the electric field on liquid film calculated along the direction of liquid lamina from nozzle exit until to its breakup point and a_b is film thickness at breakup point estimated by atomization model [3]. For water it can be considered that $T_d \sigma / \varepsilon_0 \varepsilon_r \ll 1$, therefore, the Equation (2.104) can be simplified as:

$$D - CMR_{th-2} = \frac{\varepsilon_0 \varepsilon_r E(V)}{a_b} \quad (2.105)$$

In order to have a good estimation of the electric field in both atomization model and induction charging model equations, the dependence of physical properties of water on charging potential has to be revised. The only property that had to be adjusted is the liquid surface tension σ_L . From the hypothesis that the surface charge density is the same on the liquid lamina, primary and secondary atomization droplets [67], the electric surface tension σ_e is calculated as a function of droplet charge Q_D and its Rayleigh limit Q_r [68]. Its relation with applied voltage is [11]:

$$\sigma_e = \sigma_L \left(1 - \frac{Q_D}{Q_r} \right) \quad (2.1076)$$

The droplet charge Q_D is calculated by the product of D-CMR and volume of a droplet with diameter d_p .

2.5 Literature review

A liquid jet is encountered in a large variety of fields and has attracted attention to demonstrate some physical phenomena [69]. The earliest study of the behaviour of jets and of breakup was by Leonardo da Vinci in the Codex Leicester. Da Vinci describes the detachment of a falling drop as a condition of gravity force that overcomes the surface tension cohesive action. Figure 2-13 is the sketch that Da Vinci did to represent the breakup of a liquid jet.

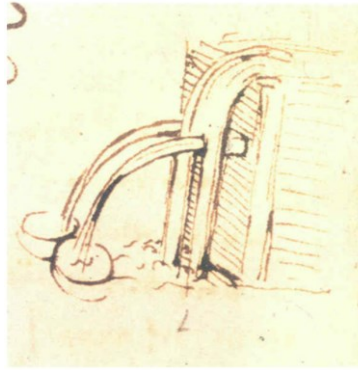


Figure 2-13-Leonardo Da Vinci scheme of liquid jet breakup [70]

Some more complex and exotic topics have also been explored widely during the 19th century and before. The breakup of liquid jets is controlled by applying external forces and during the 19th century and before the application of an electric field started to be explored. Indeed, a strong electric field can easily deform a liquid jet or control the droplet dimension. The approach and the aim of researches on electrified jets are several and they could be classified in school of thoughts.

In Poland, Jaworek and Krupa [25] developed a regime map of an electrified spray at low flow rate by testing distilled water, ethylene glycol and ethanol in a nozzle plate configuration. suggested a classification based on the characteristic time constants and on the spray current. They defined two additional spraying modes, the *precession mode* and the *oscillating-jet mode*

In the precession mode, the liquid left the capillary as a skewed cone from which a thin jet of diameter smaller than 100 μm elongated. Both the cone and the jet rotated regularly round the capillary axis, assuming a form of a fragment of a spiral. The size distribution did not change significantly with the voltage increasing, for this mode of spraying. The fundamental advantage of the precession mode of spraying was the uniform spatial dispersion of the droplets and their size distributions in each point of the spray cone. In the oscillating-jet mode, the continuous jet issued from the tip of the cone and changed its position (oscillates) in one plane with the capillary axis. The cone at the outlet of the capillary transitioned smoothly to a jet. The plane of oscillation was stable, but sometimes could change spontaneously to another orientation, or could rotate slowly around the capillary axis. The authors have been studying since 1997 [71] the presence of corona discharging in EHD atomization. In fact, the ions glow generated during the discharge influences the atomization process due to the space charge. Thanks to technology improvement, in 2014 [72] the authors demonstrated the corona discharging by analysing the light intensity during the tests and observed that when it takes place in the cone-jet mode, the effect of corona discharge is stabilizing. In recent years, their focus was on applying the electrospray in the cone-jet mode to powder production and surface coating [18], [36]. The limit in this type of application to scale it up for industries is the liquid flow rate, but Jaworek et al. suggested the use of multi nozzle systems [36].

The same Polish school has conducted studies on high-flow rate electrified sprays by induction charging in a configuration nozzle-ring and by using pneumatic hollow cone nozzles. The droplets specific charge or

D-CMR showed a non-monotonic trend with applied potential: it rose until a maximum value and then decreased because of discharges between the liquid cone and the ring electrode.

Pioneer of this science is the Spanish school that with mathematical models supported and confirmed by experimental results lays the fundamentals of any electrospray application.

Fernández De la Mora and Loscertales [42], [43] calculated that in the cone-jet mode, the electric force and surface tension balance to form a conical-like surface, called Taylor cone, with a semi-vertical angle of 49.3° . In their studies, the scaling laws of droplet diameter and current carried by the liquid that were estimated are still nowadays milestone in electrospray researches. De La mora and Rosell-Llampart defined the range of liquid flow rate in which the cone-jet mode is stable and the droplets' size distribution is monodisperse [73].

The scaling laws were revised by Gañán-Calvo using a theoretical and experimental study aimed to improve the correlations found by De La Mora and Loscertales. Indeed, Ganán-Calvo et al. observed that the current and droplets' size emitted from an electrospray of liquids with high viscosity and conductivity have a different dependence than those less viscous and conductive. It was due to how the viscosity affects the liquid acceleration caused by the electrical stress. In fact, a low-viscosity liquid, as paraffine, does not obstacle the charge transport in liquid bulk and the liquid is faster (or accelerated by the electric field). The opposite happens when the liquid has not negligible viscosity. For electrified sprays at high-flow rates, the influence of liquid physical properties on electrification process is missing and it demonstrates how the interest on electrified spray has mainly been focused on small scale.

This result agrees with studies made by Yale school of electrospray. Gomez et al. opened the researches on water electrosprays. It was observed that when the liquid is water, the minimum liquid flow rate to obtain a stable cone-jet mode depends on the presence or not of corona discharges. When the corona occurs, the minimum flow rate reduces of one order of magnitude causing a significant issue for industrial application. Gomez and Tang [29] proposed a solution by surrounding the electrospray unit with inert gas as CO₂ to delay the onset of corona. The main application of studies conducted by Gomez et al. is the drug delivery and inhalation [11], [28], [29].

In the Netherlands, Agostinho et al. for the first time studied and characterized electrohydrodynamic atomization of water in the simple-jet mode in a nozzle ring up configuration. The study of this mode is recent and there are not scaling laws of droplets diameter and electric current as for the cone jet mode. This mode allows to produce small droplets but at liquid flow rate higher than the cone-jet mode [39], [49]. More details about it can be found in Chapter 6.

In U.K., Balachandran carried experiments on both low flow rate and high flow rate electrified water sprays. In the former case, the range of operative conditions (flow rate and electric potential) to obtain a stable cone-jet mode by using pure water and saline water [22]. In the second case, hydraulic sprays electrified by induction

charging were tested with smoke cigarettes to verify the capture efficiency of PM from charged droplets [50], [74]. This is the main application of large-scale electrified sprays.

Cross et al [56] investigated the removal of particles electrically charged by means of an induction charged spray. It was employed an air-assisted nozzle to produce droplets, while the particles were got by coal dust. It was noted that the charge to mass ratio increased with the increase of voltage and atomizing air pressure. It was due to a more intense electric field and so more charge was induced on sprayed liquid. The charge to mass ratio increased linearly with the voltage until to a maximum value. The authors suggested three causes. Firstly, some of droplets could wet the electrode causing discharge peak by electric field and an ion current flowing back on charge liquid jet. The second cause could be the occurring of gas breakdown and the electric field strength was reduced and consequently the charge to mass ratio. Finally, droplets highly charge of the same polarity as the induced charge may were emitted from the liquid jet to surface disruption by stresses imposed by interaction of the surface charge and the applied field.

Layrea and No [52] studied the spraying parameters as spray angle and breakup length by atomizing kerosene. It was used a pressure-swirl hollow cone. The results underlined that the spray angle changed with increasing the applied voltage and the operating pressure. It was caused by charging of droplets, because they repulsed each other modifying the spray trajectory and the equilibrium between electric and aerodynamic forces. The breakup length increased with the increasing of liquid flow rate and voltage and the authors stated it was a consequent effect of an inconstant spray angle.

2.6 References

- [1] A. Jaworek and A. Krupa, "Charged Sprays Generation," In *Sprays: Types, Technology And Modeling*, Maria C. Vella, Ed. Nova Science Publishers, Inc., 2011, Pp. 1–100.
- [2] C. Dumouchel, "On The Experimental Investigation on Primary Atomization of Liquid Streams," *Exp. Fluids*, Vol. 45, No. 3, Pp. 371–422, 2008.
- [3] N. Ashgriz, *Handbook Of Atomization And Sprays: Theory And Applications*, Vol. 1. 2011.
- [4] C. J. Clark And N. Dombrowski, "Aerodynamic Instability And Disintegration Of Inviscid Liquid Sheets," *Proc. Roy. Soc. Lond. A*, Vol. 329, P. 467, 1972.
- [5] P. K. Senecal, D. P. Schmidt, I. Nouar, C. J. Rutland, R. D. Reitz, And M. L. Corradini, "Modeling High-Speed Viscous Liquid Sheet Atomization," *Int. J. Multiph. Flow*, Vol. 25, No. 6–7, Pp. 1073–1097, 1999.
- [6] A. Radcliffe, "The Performance Of A Type Of Swirl Atomizer," In *Proceedings Of The Institution Of Mechanical Engineers*, 1955.
- [7] Edmund Giffen And A. Muraszew, *Atomization Of Liquid Fuels*. Chapman & Hall, 1953.
- [8] Levebvre, *Atomization And Sprays*. .
- [9] D. P. Schmidt *Et Al.*, "Pressure-Swirl Atomization In The Near Field," *Sae Tech. Pap.*, Vol. 1999, No. 1999-1–496, 1999.
- [10] G. I. Taylor, "No The Mechanics Of Swirl Atomizers," In *Seventh International Congress Of Applied Mechanics*, 1948, Pp. 280–285.
- [11] K. Tang, "The Electrospray: Fundamentals And Feasibility Of Its Application To Targeted Drug Delivery By Inhalation." 1994.
- [12] D. Camelot, J. C. M. Marijnissen, And B. Scarlett, "Bipolar Coagulation Process For The Production Of Powders," *Ind. Eng. Chem. Res.*, Vol. 38, No. 3, Pp. 631–638, 1999.
- [13] K. B. Geers, "Application To Electrospray: From People To Plants," Tu Delft, 2003.
- [14] R. P. A. Hartman, "Electrohydrodynamic Atomization In The Cone Jet Mode," *Thesis*. P. 177, 1998.
- [15] T. H. Ha, O. Nishida, H. Fujita, And H. Wataru, "Enhancement Of Diesel Particulate Matter Collection In An Electrostatic Water-Spraying Scrubber," *J. Mar. Sci. Technol.*, Vol. 15, No. 3, Pp. 271–279, Sep. 2010.
- [16] M. Cloupeau And B. Prunet-Foch, "Electrohydrodynamic Spraying Functioning Modes A Critical Review," *J. Aerosol Sci.*, 1994.
- [17] J. L. Hensley, X. Feng, And J. E. Bryan, "Induction Charging Nozzle For Flat Fan Sprays," *J.*

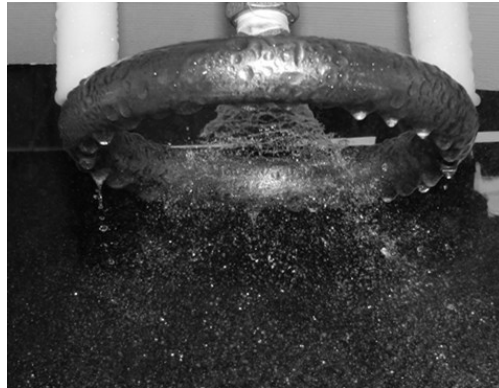
- Electrostat.*, Vol. 66, No. 5–6, Pp. 300–311, 2008.
- [18] A. Jaworek And A. T. Sobczyk, “Electrospraying Route To Nanotechnology: An Overview,” *J. Electrostat.*, Vol. 66, No. 3–4, Pp. 197–219, 2008.
- [19] L. L. F. Agostinho, “Electrohydrodynamic Atomization In The Simple-Jet Mode: Out-Scaling And Application,” 2013.
- [20] S. E. Law, “Embedded- Electrode Electrostatic-Induction Spray-Charging Nozzle: Theoretical And Engineering Design,” *Trans. Asae*, Vol. 21, No. 6, Pp. 1096–1104, 1978.
- [21] S. E. Law, “Agricultural Electrostatic Spray Application: A Review Of Significant Research And Development During The 20th Century,” *J. Electrostat.*, Vol. 6, Pp. 25–42, 2001.
- [22] O. Lastow And W. Balachandran, “Novel Low Voltage Ehd Spray Nozzle For Atomization Of Water In The Cone Jet Mode,” *J. Electrostat.*, Vol. 65, No. 8, Pp. 490–499, 2007.
- [23] M. Chaplin, “Theory Vs Experiment: What Is The Surface Charge Of Water?,” *Water J.*, 2008.
- [24] A. Jaworek And A. Krupa, “Jet And Drops Formation In Electrohydrodynamic Spraying Of Liquids. A Systematic Approach,” *Exp. Fluids*, Vol. 27, No. 1, Pp. 43–52, 1999.
- [25] A. Jaworek And A. Krupa, “Classification Of The Modes Of Ehd Spraying,” *J. Aerosol Sci.*, Vol. 30, No. 7, Pp. 873–893, 1999.
- [26] M. Cloupeau And B. Prunet-Foch, “Electrostatic Spraying Of Liquids: Main Functioning Modes,” *J. Electrostat.*, Vol. 25, No. 2, Pp. 165–184, 1990.
- [27] J. Majewski, “Measurement Methods For Size And Charge Distributions Of Electrosprayed Water Droplets.”
- [28] K. Tang And A. Gomez, “Generation Of Monodisperse Water Droplets From Electrosprays In A Corona-Assisted Cone-Jet Mode,” *J Colloid Interface Sci*, Vol. 175, No. 2, Pp. 326–332, 1995.
- [29] K. Tang And A. Gomez, “Generation By Electrospray Of Monodisperse Water Droplets For Targeted Drug Delivery By Inhalation,” *J. Aerosol Sci.*, 1994.
- [30] J. L. Castillo, S. Martin, D. Rodriguez-Perez, F. J. Higuera, And P. L. Garcia-Ybarra, “Nanostructured Porous Coatings Via Electrospray Atomization And Deposition Of Nanoparticle Suspensions,” *J. Aerosol Sci.*, No. March, Pp. 0–1, 2018.
- [31] F. Carbone And A. Gomez, “High-Resolution Dma Measurements Of Nascent Soot In A Moderately Sooting Laminar C₂H₄/Air Premixed Flame,” *Aerosol Sci. Technol.*, 2015.
- [32] E. Bodnár, J. Grifoll, And J. Rosell-Llompart, “Polymer Solution Electrospraying: A Tool For Engineering Particles And Films With Controlled Morphology,” *J. Aerosol Sci.*, 2018.
- [33] J. Rosell-Llompart, J. Grifoll, And I. G. Loscertales, “Electrosprays In The Cone-Jet Mode: From

- Taylor Cone Formation To Spray Development,” *J. Aerosol Sci.*, No. November 2017, Pp. 1–30, 2018.
- [34] F. Di Natale *Et Al.*, “Capture Of Fine And Ultrafine Particles In A Wet Electrostatic Scrubber,” *J. Environ. Chem. Eng.*, Vol. 3, No. 1, Pp. 349–356, Mar. 2015.
- [35] L. D’addio, F. Di Natale, C. Carotenuto, W. Balachandran, And A. Lancia, “A Lab-Scale System To Study Submicron Particles Removal In Wet Electrostatic Scrubbers,” *Chem. Eng. Sci.*, Vol. 97, Pp. 176–185, Jun. 2013.
- [36] A. Jaworek, A. T. Sobczyk, And A. Krupa, “Electrospray Application To Powder Production And Surface Coating,” *J. Aerosol Sci.*, No. October 2017, Pp. 1–36, 2018.
- [37] W. Balachandran, P. Miao, And P. Xiao, “Electrospray Of Fine Droplets Of Ceramic Suspensions For Thin-Film Preparation,” *J. Electrostat.*, Vol. 50, No. 4, Pp. 249–263, Mar. 2001.
- [38] O. Lastow, “Numerical And Experimental Study Of Electrohydrodynamic Atomisation Of Aqueous Liquids,” No. June, 2007.
- [39] L. L. F. Agostinho, G. Tamminga, C. U. Yurteri, S. P. Brouwer, E. C. Fuchs, And J. C. M. Marijnissen, “Morphology Of Water Electrospays In The Simple-Jet Mode,” *Phys. Rev. E - Stat. Nonlinear, Soft Matter Phys.*, Vol. 86, No. 6, Pp. 1–9, 2012.
- [40] J. M. Grace And J. C. M. Marijnissen, “A Review Of Liquid Atomization By Electrical Means,” *J. Aerosol Sci.*, Vol. 25, No. 6, Pp. 1005–1019, 1994.
- [41] L. R. F.R.S., “On The Equilibrium Of Liquid Conducting Masses Charged With Electricity,” *London, Edinburgh, Dublin Philos. Mag. J. Sci.*, Vol. 14, Pp. 184–186, 1882.
- [42] J. F. De La Mora And I. G. Loscertales, “The Current Emitted By Highly Conducting Taylor Cones,” *J. Fluid Mech.*, 1994.
- [43] J. F. De La Mora, “The Effect Of Charge Emission From Electrified Liquid Cones,” *J. Fluid Mech.*, Vol. 243, No. 1, P. 561, 1992.
- [44] M. Cloupeau And B. Prunet-Foch, “Electrostatic Spraying Of Liquids In Cone-Jet Mode,” *J. Electrostat.*, 1989.
- [45] A. M. Gañán-Calvo, J. Davila, And A. Barrero, “Current And Droplet Size In The Electrospaying Of Liquids. Scaling Laws,” *J. Aerosol Sci.*, 1997.
- [46] J. F. De La Mora, J. Navascues, F. Fernandez, And J. Rosell-Llompart, “Generation Of Submicron Monodisperse Aerosols In Electrospays,” *J. Aerosol Sci.*, 1990.
- [47] R. P. A. Hartman, D. J. Brunner, D. M. A. Camelot, J. C. M. Marijnissen, And B. Scarlett, “Jet Break-Up In Electrohydrodynamic Atomization In The Cone-Jet Mode,” *J. Aerosol Sci.*, Vol. 31, No. 1, Pp. 65–95, 2000.

- [48] L. L. F. Agostinho, C. U. Yurteri, E. C. Fuchs, And J. C. M. Marijnissen, “Monodisperse Water Microdroplets Generated By Electrohydrodynamic Atomization In The Simple-Jet Mode,” *Appl. Phys. Lett.*, Vol. 100, No. 24, Pp. 1–5, 2012.
- [49] L. L. F. Agostinho, B. Bos, A. Kamau, S. P. Brouwer, And J. C. M. Marijnissen, “Simple-Jet Mode Electrospays With Water . Description , Characterization And Application In A Single Effect Evaporation Chamber .”
- [50] W. Balachandran, A. Jaworek, A. Krupa, J. Kulon, And M. Lackowski, “Efficiency Of Smoke Removal By Charged Water Droplets,” *J. Electrostat.*, Vol. 58, No. 3–4, Pp. 209–220, 2003.
- [51] G. Artana, L. C. Bassani, And R. Scaricabarozzi, “Specific Charge Of Induction Electrified Sprays,” *J. Electrostat.*, Vol. 29, No. 2, Pp. 127–145, 1993.
- [52] G. N. Laryea And S. Y. No, “Spray Angle And Breakup Length Of Charge-Injected Electrostatic Pressure-Swirl Nozzle,” *J. Electrostat.*, Vol. 60, No. 1, Pp. 37–47, 2004.
- [53] J. A. Marchant And R. Green, “An Electrostatic Charging System For Hydraulic Spray Nozzles,” *J. Agric. Eng. Res.*, Vol. 27, No. 4, Pp. 309–319, 1982.
- [54] A. Castellanos And International Centre For Mechanical Sciences., *Electrohydrodynamics* . .
- [55] J. M. Lopez-Herrera, A. M. Gañán-Calvo, And M. Perez-Saborid, “One-Dimensional Simulation Of The Breakup Of Capillary Jets Of Conducting Liquids. Application To E.H.D. Spraying,” *J. Aerosol Sci.*, Vol. 30, No. 7, Pp. 895–912, 1999.
- [56] J. A. Cross, J. C. W. Fowler, And G. Fu, “Electrostatic Enhancement Of Water Sprays For Coal Dust Suppression,” Sydney, Australia, 2003.
- [57] J. A. Marchant, A. J. Dix, And J. M. Wilson, “The Electrostatic Charging Of Spray Produced By Hydraulic Nozzles: Part I. Theoretical Analysis,” *J. Agric. Eng. Res.*, Vol. 31, No. 4, Pp. 329–344, 1985.
- [58] Z. Han, S. Parrish, And R. D. Reitz, “Modelling Atomization Processes Of Pressure-Swirl Hollow-Cone Fuel Sprays,” *At. Sprays*, Vol. 7, Pp. 663–684, 1997.
- [59] S. Lin, “Breakup Up Of Liquid Sheets And Jets,” *Cambridge Univeristy Press*, 2003.
- [60] H. B. Squire, “Investigation Of The Instability Of A Moving Liquid Film,” *Br. J. Appl. Phys.*, Vol. 4, No. 6, Pp. 167–169, 2002.
- [61] N. Dombrowski And W. R. Johns, “The Aerodynamic Instability And Disintegration Of Viscous Liquid Sheets,” *Chem. Eng. Sci.*, Vol. 18, No. 3, Pp. 203–214, 1963.
- [62] A. A. Ibrahim And M. A. Jog, “Nonlinear Instability Of An Annular Liquid Sheet Exposed To Gas Flow,” *Int. J. Multiph. Flow*, Vol. 34, No. 7, Pp. 647–664, 2008.

- [63] G. M. Faeth, L. P. Hsiang, And P. K. Wu, “Structure And Breakup Properties Of Sprays,” *Int. J. Multiph. Flow*, Vol. 21, No. Suppl, Pp. 99–127, 1995.
- [64] J. Han And G. Tryggvason, “Secondary Breakup Of Axisymmetric Liquid Drops. Ii. Impulsive Acceleration,” *Phys. Fluids*, Vol. 13, No. 6, Pp. 1554–1565, Jun. 2001.
- [65] M. Pilch And C. A. Erdman, “Use Of Breakup Time Data And Velocity History Data To Predict The Maximum Size Of Stable Fragments For Acceleration-Induced Breakup Of A Liquid Drop,” *Int. J. Multiph. Flow*, Vol. 13, No. 6, Pp. 741–757, Nov. 1987.
- [66] J. A. Nicholls; And A. A. Range, “Aerodynamic Shattering Of Liquid Drops,” *Aiaa J.*, Vol. 7, No. 2, Pp. 285–290, Feb. 1969.
- [67] A. Krupa, A. Jaworek, A. T. Sobczyk, A. Marchewicz, M. Szudyga, And T. Antes, “Charged Spray Generation For Gas Cleaning Applications,” *J. Electrostat.*, Vol. 71, No. 3, Pp. 260–264, 2013.
- [68] D. C. Taflin, T. L. Ward, And E. J. Davis, “Electrified Droplet Fission And The Rayleigh Limit,” *Langmuir*, Vol. 5, No. 2, Pp. 376–384, Mar. 1989.
- [69] J. Eggers And E. Villermaux, “Physics Of Liquid Jets,” *Reports Prog. Phys.*, Vol. 71, No. 3, 2008.
- [70] L. Da Vinci, *The Codex Leicester*. 1980.
- [71] A. Jaworek And A. Krupa, “Studies Of The Corona Discharge In Ehd Spraying,” *J. Electrostat.*, Vol. 41, Pp. 173–178, 1997.
- [72] A. Jaworek, A. T. Sobczyk, T. Czech, And A. Krupa, “Corona Discharge In Electrospraying,” *J. Electrostat.*, Vol. 72, No. 2, Pp. 166–178, 2014.
- [73] J. Rosell-Llompart And J. F. De La Mora, “Generation Of Monodisperse Droplets 0.3 To 4 μ m In Diameter From Electrified Cone-Jets Of Highly Conducting And Viscous Liquids,” *J. Aerosol Sci.*, 1994.
- [74] W. Balachandran, A. Krupa, W. Machowski, And A. Jaworek, “Smoke Precipitation By Charged Water Aerosol,” *J. Electrostat.*, Vol. 51–52, No. 1–4, Pp. 193–199, 2001.
- [I] <http://www.lechler.de>

Chapter 3. Induction Charging and Breakup of Water Sprays¹



pic by L. Manna

¹ The chapter is based on publications:

Chemical Engineering Transaction, vol 52, 2016 DOI: 10.3303/CET1652071

Conference proceeding ILASS – Europe 2016, 27th Annual Conference on Liquid Atomization and Spray Systems, 4-7 September 2016, Brighton, UK

3.1 Introduction

Interest in charging water sprays has started years ago to exploit their possible use in many research fields from drug delivery to agricultural and industrial processes. The combination of aerodynamic and electrostatic forces improves the dispersion of liquids in gas and forms smaller droplets. Recently, many studies on the electrostatic spraying of pesticides in agricultural applications found that the electric forces improved the adhesion and the distributions of droplets on target [1]: the charged droplets wet both the upper and the bottom sides of leaves thanks to the electrostatic attraction between the leaves surfaces, that are grounded, and the charged drops [2].

Liquid sprays deliver inside positive and negative charge but are globally electrically neutral. This was observed for natural waterfalls by Lenard [3]. He found that the production of a negative charge occurred at the base of a waterfall after the splashing. Huschke [4] applied the “Lenard effect” to the separation of electric charge accompanying the aerodynamic breakup of water drops [5].

When an electric field is applied, the negative and positive charges are distributed so that the net charge is zero and the drops carry on either a net negative or a positive charge [1]. Liquid spray can be charged by corona charging, electrospray or induction charging. The latter lets exert the spray with lower operating voltages, compared with corona, and with higher liquid flow rate compared to electrosprays. In the induction charging, a positively or negatively charged HV electrode is held in the vicinity of a grounded spray nozzle. The liquid cone is polarized: the liquid exiting from the nozzle breaks up due to natural surface instability phenomena and the formed droplets trap a charge opposite to electrode one, while the free charges with same polarity of electrode move towards the ground via the nozzle [6]. The induction charging is effective if the fluid is sufficiently conductive to allow an efficient charge transfer to droplets during their formation [6, 8]. It means that the charge relaxation time, τ , has to be much smaller than droplets formation time, τ_b . It was indicated that the minimum required liquid conductivity is 10^{-10} S/m [2]. Thanks to its high conductivity, water is an appropriate candidate as electrified spray, but it is rarely used because of its ionic properties. Indeed, the electrification of water sprays is more unstable than that of dielectric and/or organic liquids [7].

Among the few studies conducted with water, Cross et al. [9] investigated properties of induction charged sprays with air assisted nozzle. The charge acquired by droplets increased with applied potential until to a limit identified by the occurrence of gas breakdown. Balachandran et al [10] carried out experiments with charged and uncharged water droplets to evaluate the removal of smoke particles from air. It was observed that the charging of water droplets significantly increased the efficiency of capture.

Di Natale et al. [11, 12, 13] applied the electrification of liquid spray on marine diesel engines emission control. In a pilot scale wet electrostatic scrubber experiments with oppositely charged tap water droplets and carbon particles were conducted. It was observed that the electrostatic interaction between droplets and particles allowed to achieve removal efficiencies as high as 93%.

Ha et al. [14] employed sea water as liquid spraying in induction charging atomization to capture particles emitted by marine engines. The measured droplets specific charge was higher than the same calculated with tap water. The result was explained by the greater sea water conductivity due to salts presence (3.21 S/m instead of 0.75 S/m): in water the salts released ions, and these enhanced the charging phenomenon. Indeed, the liquid conductivity, which represents the property of a liquid to transport charges when an electric field or a potential difference is applied, increases in presence of aqueous impurities. For this reason, the experimental tests of this work were executed using tap water instead of deionized one.

The effectiveness of induction charging depends on breakup mechanism of liquid spray and droplets diameter. Krupa et al. [15] compared the spray currents measured with a hollow cone nozzle and a full cone one varying the applied potential. For both nozzle types, the current increased with voltage up to a maximum value that was higher for the hollow cone. The result was explained by the authors as a consequence of the diverse mechanism of liquid jet disruption and droplet distribution. In fact, the hollow cone produces finest droplets that acquire more charge.

Most of the studies conducted on water electrified spray are based on the assumption that the presence of electric field does not influence the hydrodynamic of jets. However, Laryea and No [16] studied the breakup mechanism and its related parameters as spray angle and breakup length by atomizing kerosene in a hollow cone spray. They found that both the breakup length and spray angle changed with the electric potential. The change in spray angle was explained by repulsion of equally charged droplets; the modification of breakup length influenced the charge that droplets could trap during their formation.

At our knowledge, for tap water few studies had been conducted on the electro-hydrodynamic of induction charged sprays. Our research group started to study the electro-hydrodynamic of water induction charged sprays and the breakup length produced by two hollow cone nozzles in absence of electric field and at different potentials was evaluated [17]. The breakup length reduced by more than 25% by increasing potential suggesting that the electric field actually influenced the jet breakup dynamics.

In this chapter, the experimental results on both water spray charging, and its atomization mechanism in presence of the electric field are presented. We tested hollow cone sprays in a lab-scale charging unit in which tap water was inductively charged. The Droplet Charge to Mass Ratio, D-CMR, was evaluated by the ratio of measured droplets current I_{drop} and liquid flow rate Q_L as:

$$D - CMR = \frac{I_{drop}}{Q_L} \quad (3.1)$$

The experimental water charging was compared to theoretical predictions of the induction charging model of Artana et al. [18]. The atomization parameters were estimated by the hydrodynamic model of liquid sheet or *LISA* model [19], except for the breakup length that was evaluated optically. The breakup mechanism was investigated in both uncharged and charged conditions.

3.2 Material and methods

The experiments were conducted with tap water with a conductivity of about 0.75 S/m in a lab-scale experimental rig, whose schematic representation is showed in Figure 3-1. It consisted in an open electrified spray. The electrified spray is composed by three main components: i) a charging electrode in the form of a full metallic ring with internal diameter of 110 mm and external diameter of 130 mm (9); a hydraulic spray nozzle placed along the centreline of the electrode at a given height from its plane (10) and iii) a support structure (7). This last was a Teflon parallelepiped 200×62×90 mm sizes supporting two Teflon shielded high voltage connections to the electrodes and a grounded metal tube used to feed water to the nozzle. Also, the support structure was electrically grounded.

The high voltage was provided by a Spellman DC power supplier BERTRAN 230 (6) with reversible polarity. The liquid was sprayed using a volumetric pump (FLUID-TECH PO 060) regulated through an inverter (2,3).

The water felt in a large (1500×1500×200 mm) grounded tank to collect water (14). Its size was chosen so that the footprint of the spray is far smaller than the tank surface. Four slim metallic bars were welded to the four edges of the tank and to a horizontal metallic frame (1500×400×10 mm) placed at 1300 mm height, on which the electrified spray support was fixed.

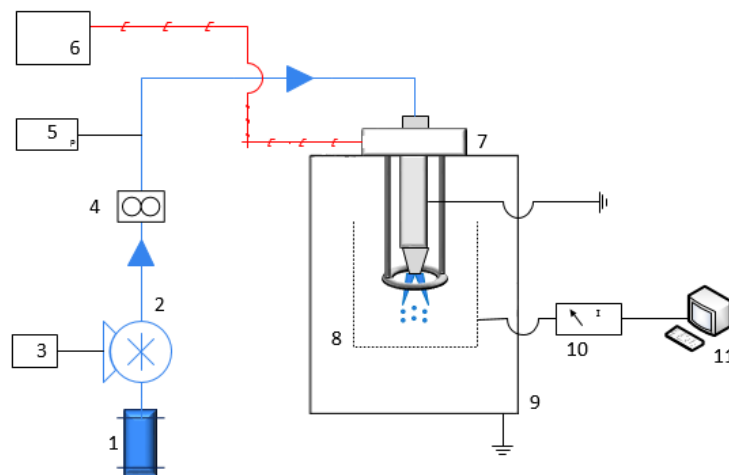


Figure 3-1- Experimental Rig. 1: water tank, 2: pump, 3: inverter, 4: flow meter, 5: pressure gauge, 6: HV power supply, 7: droplet charge unit (DCU), 8: Faraday pail, 9: water collector, 10: electrometer, 11: computer to elaborate experimental results. The red line indicates the high-tension connection, while the blue line is the liquid flow path.

Hydraulic hollow cone nozzles manufactured by different companies were used: the nozzle BD5 produced by Spraying Systems and the nozzles 216.364 and 216.404 made by Lechler. The nozzle design could be found on the catalogue [I-II]; in Table 3-1, the spray angle and liquid flow rates at different pressures are reported.

Table 3-1- Summary of fluid-dynamic properties of tested nozzle. SS: Spraying System; LC: Lechler

Nozzle	Type of nozzles	Spray angle θ , °	d_0 , m	Q_L , L/min						
				1 bar	2 bar	2.5 bar	3 bar	3.5 bar	4 bar	6 bar
BD5	SS	≈ 60	0.0032	2.3	3.2	3.57	3.9	4.27	4.6	/
216.364	LC	≈ 60	0.0014	0.53	0.71	/	0.81	/	0.9	1.16
216.404	LC	≈ 60	0.002	0.85	1.16	/	1.4	/	1.58	1.95

Two experimental campaigns were conducted to evaluate the charge acquired from liquid droplets at different voltages and to observe how the fluid-dynamic features of spray were influenced by electric field.

As a starting point, the breakup length L_b and the spray angle θ in uncharged condition and as function of the applied voltage were evaluated by optical tests. Photos were taken with a NIKON P300 at $P=3$ and 6 bar for Lechler nozzles and at P ranging from 2 and 4 bar for Spraying systems ones. The images were elaborated with the software Image Pro Plus[®]. An example of optical tests results is shown in Figure 3-2 for two applied voltages

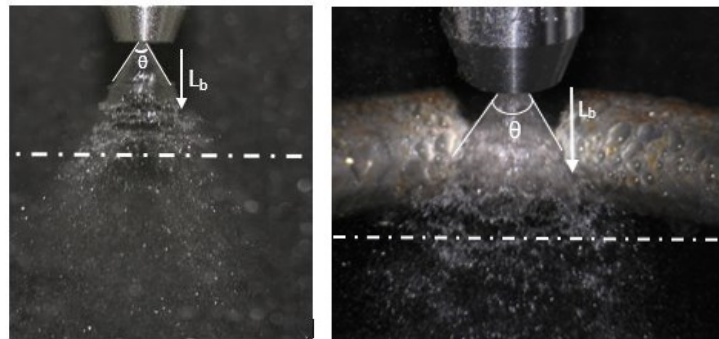


Figure 3-2- Breakup length and spray angle. In the pictures the nozzle 216.364 at $P=3$ bar is reported at 0 kV (left) and at $V=10$ kV (right). The dotted line divides the primary and secondary atomization zones.

The second investigation aimed to measure the charge acquired from sprayed droplets. The charging tests were executed by placing the electrode at exactly L_b cm from the nozzle exit and the Droplet Charge to Mass Ratio (D-CMR) was estimated according equation (3.1) by measuring the droplets current at different charging potential.

As a general rule, the values of D-CMR showed a linear increase with electric potential up to reach te maximum at $V=V_{opt}$, then it started to decrease. From 0 kV to V_{opt} , the spray angle and the breakup length at each potential were measured through optical tests to estimate in both uncharged and charged conditions the spray parameters.

3.3 Results

In Figures 3-3 and 3-4, the breakup length L_b , the droplets charging I_{drop} and the D-CMR trends with electric potential at different pressures are showed for SS nozzles (Fig. 3-3) and LC nozzles (Fig. 3-4), respectively.

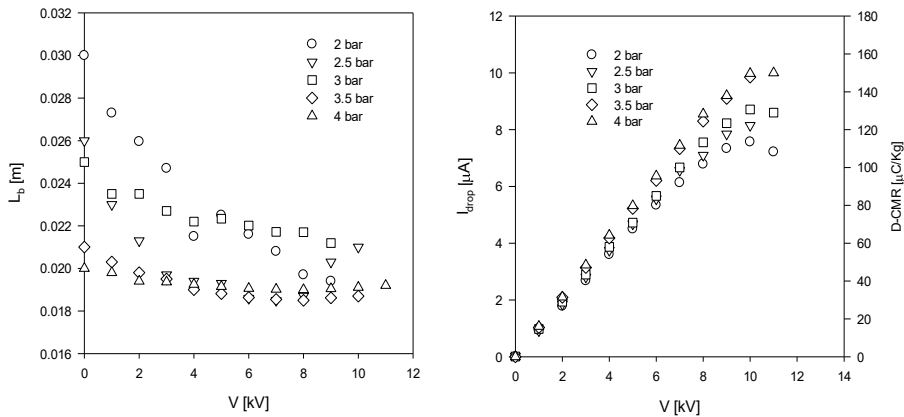


Figure 3-3- Breakup Length L_b (left), droplets current I_{drop} and D-CMR (right) as function of applied voltages at different pressures.

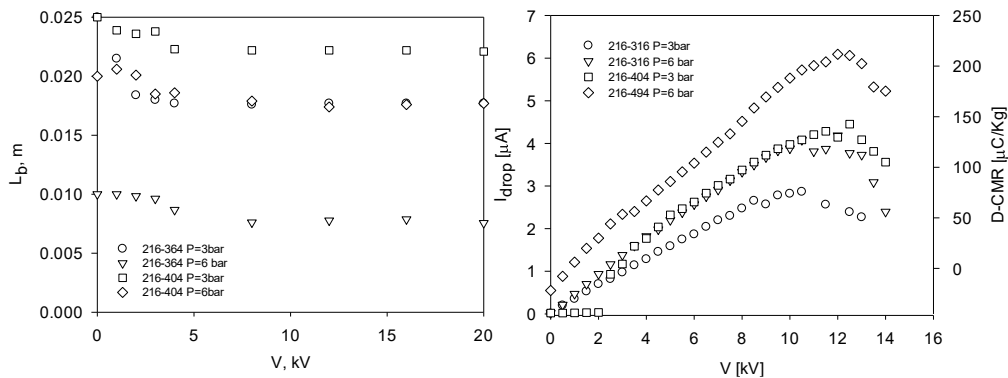


Figure 3-4- Comparison of breakup length ((left) and Droplet charge to mass ratio/droplets current (right) at different voltages for nozzles LC Nozzle

Regarding the behaviour of L_b , it is evident how the breakup length decreased with applied voltages. In uncharged condition ($V=0$ kV), it can be noted that as pressure increased and so the flow rate, the breakup length decreased as a consequence of a greater aerodynamic force acting on liquid lamina. As a function of voltage, it was observed that the breakup length had the most of reduction at low voltages, then for most of the experiments, it reached an almost constant value as if the “global disturbance” has reached a steady condition. Indeed, the reduction of the breakup length might be explained as the addition of a perturbation caused by electric field to the aerodynamic forces acting on liquid sheet. It is worth to underline that the percentage of reduction of L_b is affected both by the difficulties in evaluation of the parameter optically and by the error in estimation of L_b means by a software. The spray angle slightly increased by about 5 degs by increasing the electric potential because of the repulsion of charge droplets (details in Table 3-2)

The measured current (and the D-CMR) had a linear increase with voltage with slope β until reaching its highest value at V_{opt} , then it started to decrease. The slope β increased with pressure: the higher the flow rate, the higher the current. Indeed, the maximum charging level was measured at the highest pressure tested for each nozzle with an increase of about 50% of electric current.

Table 3-2 resumes the main results of the experimental campaign.

Table 3-2- Experimental studies results

P [bar]	Type of nozzle	Q_L [L/min]	β [1/ Ω]	L_b (0 kV) [m]	L_b (V_{opt}) [m]	$V_{opt} 10^{-3}$ [V]	$I_{opt} 10^{-6}$ [A]	θ (0 kV) [°]	θ (V_{opt}) [°]
2	SS-BD5	3.2	0.83	0.03	0.0194	9	7.57	60	72
2.5	SS-BD5	3.57	0.88	0.026	0.0203	10	8.11	60	77.4
3	SS-BD%	3.9	0.92	0.025	0.0212	10	8.71	60	79
3.5	SS-BD5	4.27	1	0.021	0.0186	10	9.85	60	84
4	SS-BD5	4.6	1.02	0.02	0.0147	11	10	60	84
3	LC-216.364	0.81	0.3	2.5	1.76	10.5	2.86	60	60
6	LC-216.364	1.16	0.39	1	0.75	12	4.18	60	65
3	LC-216.404	1.4	0.40	2.5	2.2	12.5	4.45	60	60
6	LC-216.404	1.96	0.56	2	1.74	12	6.09	60	62

3.4 Discussion

The experimental assessment of breakup length at different electric potentials allowed the estimation of breakup parameters such as sheet thickness at nozzle exit (a_0) and at breakup point (a_b), the droplets mean diameter² (d_D) and breakup time (t_b). They were calculated from Linearized Instability Sheet Atomization (*LISA*) model [16]. This is a fluid-dynamic model that takes into account the aerodynamic instability that causes the jet breakup. The mathematical analysis considers a wavy disturbance acting on the liquid film that develops at nozzle exit. This film breaks into ligaments and successively into droplets. This breakup mechanism is called primary atomization. The formed droplets break into smaller drops because of interaction with surrounding air (secondary atomization). In Figure 3-5, the breakup mechanism for our nozzle is showed by underlying the primary and secondary atomization zones.

² The *LISA* model estimates the droplets mean diameter d_D as mean value of a Rosin-Rammler distribution [19]

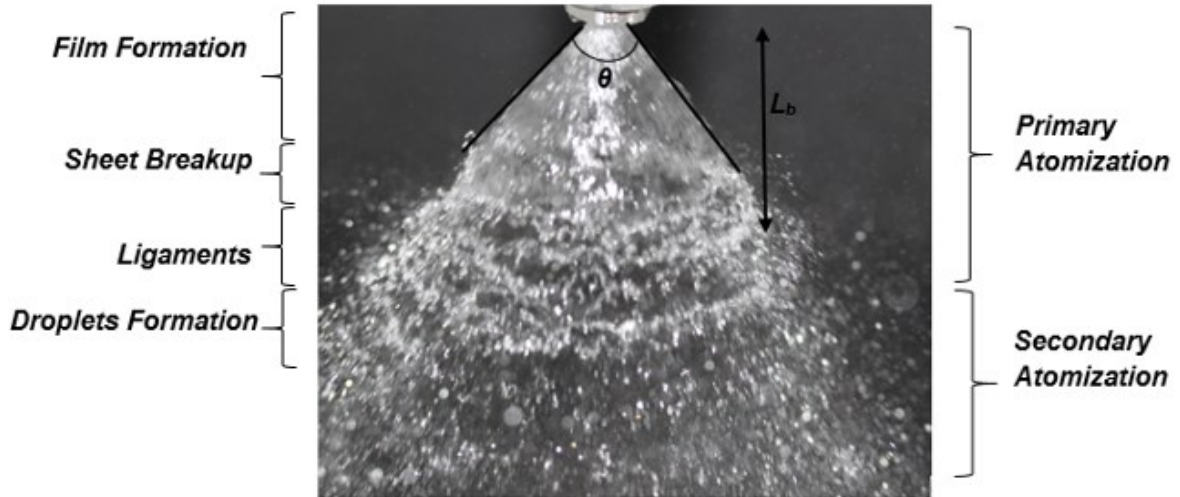


Figure 3-5- Breakup mechanism for tested nozzle

In order to have a good implementation of electric field in model equations, the dependence of physical properties of water on charging potential was revised. The only property that had to be adjusted was the liquid surface tension, γ . From the hypothesis that the surface charge density is the same on liquid lamina, primary and secondary atomization droplets [15], the electric surface tension γ_e was calculated as function of droplet charge Q_D and its Rayleigh limit Q_r [22]. Its correlation with applied voltage is [21]:

$$\gamma_e = \gamma_L \left(1 - \frac{Q_D}{Q_r}\right) \quad (3.2)$$

The droplet charge Q_D was calculated, for each potential from 0 kV to V_{opt} by the product of D-CMR and volume of a droplet with diameter d_D , obtained from *LISA* equations. The Rayleigh limit was calculated according to the equation:

$$Q_r = \sqrt{8\pi^2 \epsilon_0 \gamma d_D^3} \quad (3.3)$$

In Figure 3-6, the trend of electrical surface tension with voltage for the single nozzle SS-BD5 is graphed.

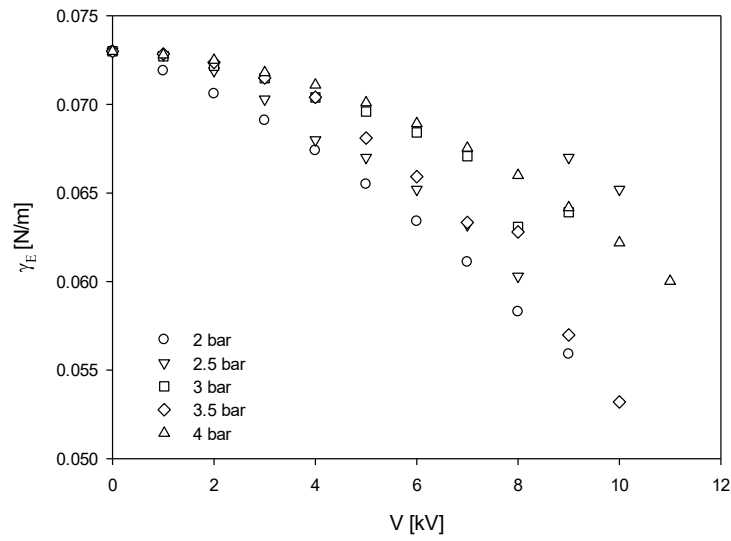


Figure 3-6 Electrical surface tension as function of applied electric potentials at different liquid pressure for the nozzle SS-BD5.

The presence of electric field caused a reduction of liquid surface tension. By rewriting the equation (3.2) as function of primary atomization droplet diameter, d_D , we obtained:

$$\gamma_e \approx \gamma_L \left(1 - \frac{d_D^3}{d_D^{3/2}} \right) \quad (3.4)$$

As the atomization pressure increases, the droplets diameter reduces and γ_e grows. In our opinion, this result explains why in Figure 3-6 the greater reduction of liquid surface tension with potential was noted at low pressure. Table 3-3 and 3-4 list the parameters extrapolated from *LISA* model for all tested nozzles at 0 kV and at V_{opt} , respectively.

Table 3-3- LISA model parameters in uncharged conditions. SS: Spraying systems. LC: Lechler

P [bar]	Type of nozzle	$L_b \cdot 10^{-2}$ [m]	$a_0 \cdot 10^{-4}$ [m]	$a_b \cdot 10^{-4}$ [m]	$d_D \cdot 10^{-3}$ [m]	$t_b \cdot 10^{-4}$ [s]
2	SS-BD5	3	4.60	0.889	1.31	19.3
2.5	SS-BD5	2.6	4.59	1.01	1.29	14.9
3	SS-BD5	2.5	4.59	1.06	1.21	13.2
3.5	SS-BD5	2.1	4.53	1.23	1.21	10.2
4	SS-BD5	2	4.65	1.29	1.21	9.03
3	LC-216.364	2.5	2.3	2.49	6.61	1.13
6	LC-216.364	1	2.3	5.10	6.10	41.7
3	LC-216.404	2.5	2.7	3.67	8.60	1.50
6	LC-216.404	2	2.7	4.37	5.80	89.0

Table 3-4- LISA model parameters in presence of electric field at V_{opt} . SS: Spraying systems. LC: Lechler

P [bar]	Type of nozzle	$L_b \cdot 10^{-2}$ [m]	$a_0 \cdot 10^{-4}$ [m]	$a_b \cdot 10^{-4}$ [m]	$d_D \cdot 10^{-3}$ [m]	$t_b \cdot 10^{-4}$ [s]
2	SS-BD5	1.94	4.60	1.11	1.34	15.0
2.5	SS-BD5	2.03	4.59	1.22	1.35	12.08
3	SS-BD5	2.12	4.59	1.22	1.23	11.2
3.5	SS-BD%	1.86	4.53	1.36	1.09	9.06
4	SS-BD5	1.91	4.65	1.34	1.089	8.63
3	LC-216.364	1.76	2.3	3.11	7.23	8.97
6	LC-216.364	0.75	2.3	7.09	6.92	2.92
3	LC-216.404	2.2	2.7	4.50	9.09	12.1
6	LC-216.404	1.74	2.7	5.64	6.30	6.81

By comparing the results, it was observed that the half sheet thickness a_0 increased with diameter d_0 and as consequence the larger a_0 , the bigger half sheet thickness at breakup point. It is worth underlining

that, in uncharged condition, as the pressure increased the aerodynamic forces acting on liquid lamina were more intense at higher flow rate. As consequence, the LISA model predicted that the sheet broke earlier (smaller breakup time) with a larger thickness and larger droplets were formed.

To take into account for the effect of charging potential, these parameters were estimated, for each pressure, at increasing voltage. It was observed that the breakup thickness was larger as the breakup length L_b and the breakup point t_b were lower. These results indicate clearly the effect of electrical perturbation on the liquid sheet.

The values of sheet thickness at breakup point for electric potential ranging from 0 kV to V_{opt} were used to evaluate the theoretical Droplet Charge to Mass Ratio by the induction-charging model [18] and compare it to the experimental one. The model regards a cylindrical liquid sheet polarized by electric field with a constant thickness along the spray until the breakup point. The system liquid lamina-electrode is schematised as an electrical circuit and the D-CMR_{th} comes out to be dependent on applied electric potential through the electric field. The theoretical model calculates the Droplet Charge to Mass Ratio as:

$$D - CMR_{th} = \frac{\varepsilon_0 E(V)}{a_b} \left\{ \frac{\varepsilon_0 \varepsilon_r}{\sigma \tau_d} \left(1 - \exp\left(\frac{-K T_d}{\varepsilon_0 \varepsilon_r}\right) \right) - 1 \right\} \quad (3.5)$$

where ε_0 and ε_r are the vacuum and liquid permittivity respectively, $E(V)$ is the electric field on liquid film calculated along the direction of liquid lamina from nozzle exit until to its breakup point from computational studies using the electrostatic module of COMSOL Multiphysics, K is the liquid conductivity, τ_b is the droplet time formation (breakup time) and a_b is film thickness. For water it can be considered that $\tau_b \ll 1$ to simplify Equation 3.5 and express the theoretical specific charge of droplets as:

$$D - CMR_{th} = \frac{\varepsilon_0 \varepsilon_r E(V)}{a_b} \quad (3.6)$$

Due to the geometrical constraints of the Artana model, we think that a comparison among experimental and theoretical results should consider a corrective, geometrical, factor that we define as α .

In Figures 3-7 and 3-8, D-CMR_{exp} versus D-CMR_{th} is graphed for SS-BD5 and LC nozzles, respectively.

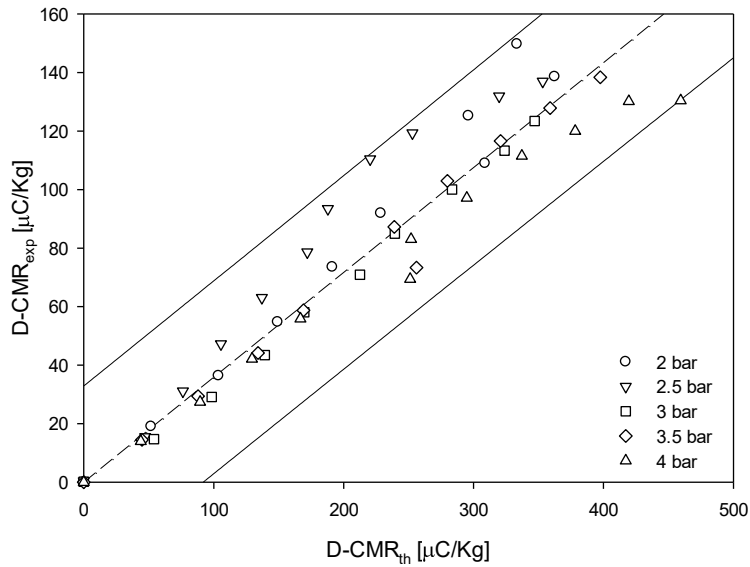


Figure 3-7- Comparison of experimental and theoretical Droplet Charge to Mass Ratio for SS-BD5.

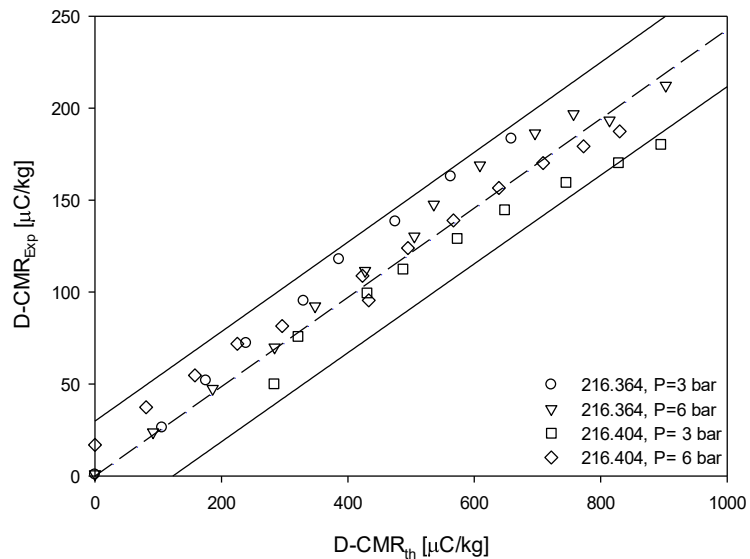


Figure 3-8- Comparison of experimental and theoretical Droplet Charge to Mass Ratio for LC-nozzles.

It is worth to underline that experimental data of LC-216.404 at P=3 bar from 0 kV to 4 kV are not plotted because this evaluation is restricted to the linear range of D-CMR (V). All data were fitted with a linear regression to estimate the slope that is the proportional factor between experimental and theoretical evaluations. The result of regression was a coefficient of $0.243 \pm 8.80 \cdot 10^{-3}$ and a coefficient of determination R^2 of 0.9364 for LC nozzles and a correction factor of 0.34 ± 0.013 and a coefficient of determination R^2 of 0.94 for SS-BD5.

It can be observed that all data are enclosed in a defined range. It implies that the model describes the experimental values satisfactory.

3.5 Summary

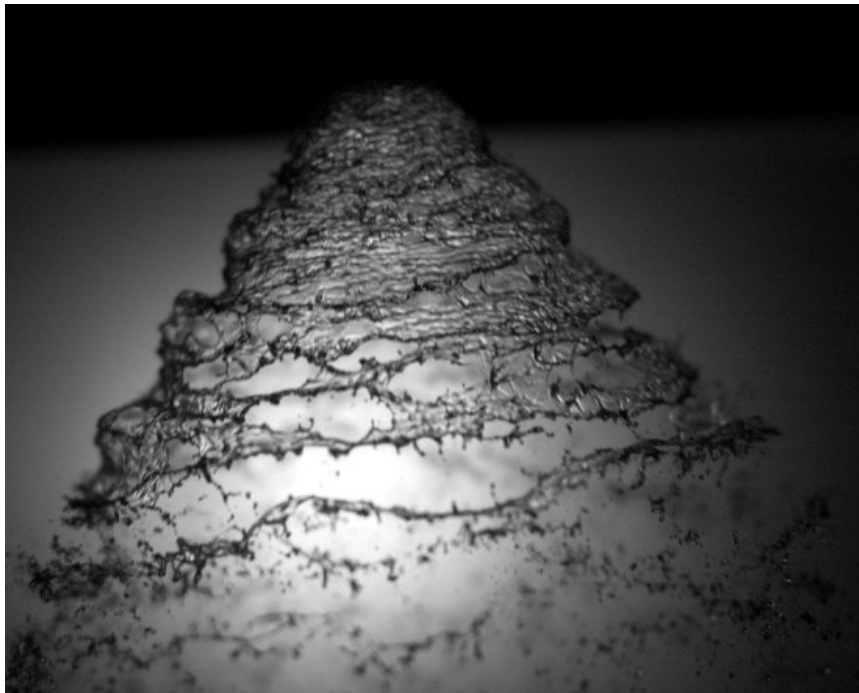
In this experimental campaign, a lab-scale electrified spray was studied to estimate the specific charge of liquid droplets and the electro-hydrodynamic properties of spray. Different 60 degree hollow cone nozzles were electrically charged by induction through a toroidal ring as induction charging electrode and tested at different operating pressures. The spray breakup parameters in uncharged and charged conditions and droplets charge as D-CMR were estimated at different electric potentials. The breakup length L_b decreased with pressure. We observed that, once electric potential was applied, for each investigated pressure the value of L_b was smaller than that estimated for the uncharged spray, suggesting that the electric field actually influenced the jet break-up dynamics. The experiments revealed that the D-CMR increased linearly with the potential with a slope β that depended on liquid pressure. The D-CMR reached an optimum at a potential named V_{opt} and then it started to decrease. For voltages ranging from 0 kV to V_{opt} , the theoretical Droplet Charge to Mass Ratio was estimated and compared to the experimental results. The experimental D-CMR was described from the model satisfactorily with a corrective factor about 0.34 and 0.243 for SS and LC nozzles, respectively. Future works might need a deeper investigation to verify whether the corrective factor is universal or if it depends on the geometry of system as nozzle dimension, induction electrode geometry and surrounding gas temperature and humidity.

3.6 References

- [1] Hislop, E.C., 1988, *Weed Science Society of America and Allen Press*, 2, pp. 94-105
- [2] S. E. Law, "Agricultural electrostatic spray application: a review of significant research and development during the 20th century," *J. Electrostat.*, vol. 6, pp. 25–42, 2001.
- [3] Pierce, E.T. and Whitson, A.L., 1964, *Journal of the Atmospheric Sciences*, 22, pp. 314-319
- [4] Huschke, R., 1959, *American Meteorological Society*,
- [5] Lenard, P., 1982, 46, *Annals of Physics*, 46, pp. 584-636
- [6] Henley, J.L., Feng, X., and Bryan, J.E., 2008, *Journal of Electrostatics*, 66, pp. 300-311
- [7] Lastow, O., 2007, "Numerical and Experimental Study of Electro-hydro-dynamic Atomization of Aqueous Liquids", PhD dissertation, London, UK.
- [8] S. E. Law, "Embedded- Electrode Electrostatic-Induction Spray-Charging Nozzle: Theoretical and Engineering Design," *Trans. ASAE*, vol. 21, no. 6, pp. 1096–1104, 1978.
- [9] J. A. Cross, J. C. W. Fowler, And G. Fu, "Electrostatic Enhancement Of Water Sprays For Coal Dust Suppression," Sydney, Australia, 2003.
- [10] W. Balachandran, A. Krupa, W. Machowski, And A. Jaworek, "Smoke Precipitation By Charged Water Aerosol," *J. Electrostat.*, Vol. 51–52, No. 1–4, Pp. 193–199, 2001.

- [11] Di Natale, F., D'Addio, L., Carotenuto, C. and Lancia, A, "Capture of fine and ultrafine particles in a wet electrostatic scrubber," *J. Environ. Chem. Eng.*, vol. 3, no. 1, pp. 349–356, Mar. 2015.
- [12] Di Natale, F. and Carotenuto, C., 2015, *Transportation Research Part D: Transport and Environment*, 40, pp. 166-191
- [13] Di Natale, F., Carotenuto, C., D'Addio, L., Lancia, A. and Balachandran, W., 2013, *Chemical Engineering Transaction*, 32. pp. 361-366
- [14] T. H. Ha, O. Nishida, H. Fujita, and H. Wataru, "Enhancement of diesel particulate matter collection in an electrostatic water-spraying scrubber," *J. Mar. Sci. Technol.*, vol. 15, no. 3, pp. 271–279, Sep. 2010.
- [15] Krupa, A. and Jaworek, A., 2013, *Journal of Electrostatics*, 64, pp. 194-202
- [16] G. N. Laryea and S. Y. No, "Spray angle and breakup length of charge-injected electrostatic pressure-swirl nozzle," *J. Electrostat.*, vol. 60, no. 1, pp. 37–47, 2004.
- [17] L. Manna, F. Di Natale, C. Carotenuto, and A. Lancia, "Electrified water sprays generation for gas pollutants emission control," *Chem. Eng. Trans.*, vol. 52, 2016.
- [18] G. Artana, L. C. Bassani, And R. Scaricabarozzi, "Specific Charge Of Induction Electrified Sprays," *J. Electrostat.*, Vol. 29, No. 2, Pp. 127–145, 1993.
- [19] N. Ashgriz, *Handbook of atomization and sprays: theory and applications*, 1st edition, Springer, New York, 2011
- [21] Tang, K., "The Electrospray: fundamentals and feasibility of its application to targeted drug delivery", 1994.
- [22] D. C. Taflin, T. L. Ward, And E. J. Davis, "Electrified Droplet Fission And The Rayleigh Limit," *Langmuir*, Vol. 5, No. 2, Pp. 376–384, Mar. 1989.
- [I] <https://www.spray.com/>
- [II] <https://www.lechler.com/de-en/>

Chapter 4. Primary atomization of electrified water sprays³



pic by L. Manna

³ This chapter is based on the publication: *Canadian Journal of Chemical Engineering*, vol.95, 2017 DOI <https://doi.org/10.1002/cjee.22841>

4.1 Introduction

The spray technology plays a key role in many chemical and mechanical engineering processes based on the dispersion of a liquid in a gaseous stream: surface coating, fuel injections, water scrubbing, drug delivery, synthesis of nanoparticles are exemplar fields of sprays employment [1,2].

The efficacy of a spray depends on drop-size and velocity distributions, droplet density (defined by the number of droplets per unit volume), droplet spatial distribution (defined by the local volume fraction) and droplet temperature [2]. One of the main issues in the analysis of spray hydrodynamics is predicting the features of the sprayed droplets starting from the geometric characteristics of the nozzle and the physical properties of the liquid and the gas.

It is widely accepted that the spray hydrodynamic is described by the sequence of three phenomena.^[3,4] Initially, during the so-called Jet Breakup Phase, the liquid sheet exiting the nozzle tip is subjected to several mechanical disturbances occurring at the liquid-gas interfaces and related to competition between aerodynamic, inertial, shear and centrifugal forces - responsible for the stretching of the liquid sheet - and the surface tension, which tends to preserve the original shape of the liquid-gas interface.^[5] With specific attention to swirl hollow cone nozzles, as those used in this work, the disturbances occurring at liquid-gas interface are described by Kelvin-Helmholtz waves [6]. The swirling motion is transferred to the liquid by means of one or more swirl chambers. In this kind of nozzle, the pressure decreases towards the nozzle orifice until it reaches atmospheric pressure and an air core is formed within the liquid cone. The solid cone formed between the median plane of the jet and the vertical axis from the nozzle centre is called spray angle, 2θ . As Fu et al. observed, the air core is a prerequisite for the formation of conical liquid sheet with a variable thickness from the nozzle exit until the breakup [7]. The disturbances increase progressively, while at a given distance from the nozzle tip – called breakup length, L – they reached a critical value and the liquid sheet breaks forming primary ligaments. The disturbances propagate on the same primary ligaments until they separated to form primary droplets (that is known as Primary Atomization Phase). Successively, the primary droplets undergo a Secondary Atomization Phase, which leads to their rupture and to the formation of the actual spray.^[3] Once the liquid forms secondary droplets, the spray behaviour is determined by drag, collision and coalescence phenomena [8].

For a given nozzle geometry, the atomization quality depends on injection pressure. In fact, five stages can be identified: dribble, distorted pencil, onion, tulip and fully developed [9]. The breakup length and the spray angle are estimated when the spray is fully developed, and they determine the properties of the ligaments and of the primary droplets as well as their influence on the secondary atomization patterns and the dispersion of sprayed droplets in the gas phase.

Several models have been developed to understand the atomization dynamic and estimate the breakup length of liquid [8,10–15]. Squire described a moving liquid sheet with a constant thickness in a linear 2D system and provided the explanation of the disturbance due to growing waves on liquid surfaces

[11]. Dombrowski and Clark and Dombrowski and John extended Squire's study [12,15]. The authors found that the disturbance was an asymmetric long sinuous wave and, as a consequence, the sheet thickness diminished until the wave reached the maximum growth rate. At this point, the sheet rupture occurred. Senecal et al. pointed out that the aerodynamic perturbation over the liquid sheet was dependent on both liquid physical properties (viscosity and surface tension) and wave type (short and long)[8]. Senecal et al. derived a critical Weber number for the transition from long to short waves and formulated models for wave growth-rate as a function of the wave type [8]. With these equations, Senecal et al. developed a robust modelling to estimate the jet breakup parameters (L and θ) as well as the primary ligaments diameter [8]. From Senecal et al. and Schmidt et al. studies, the Linearized Instability Sheet Atomization (LISA) model was extracted [3,6,8]. In this model the breakup point of liquid sheet is estimated starting from the breakup time. This last, the ligaments diameter and the sheet thickness at breakup point are evaluated as function of wave number (or frequency) corresponding at the maximum growth rate [6].

It means that the jet breakup parameters are strongly dependent on the way the perturbation spreads over the liquid surface. A validation of this dependence is the effect of pressure on jet atomization. In fact, as the pressure increases, the wavy growth becomes faster as the liquid sheet rupture.

Recently, it was shown that electric forces can be combined with hydrodynamic ones to improve the droplets dispersion in gases [16,17]. In fact, if the droplets are charged, they repel each other, better dispersing in the gas stream. Besides, when subjected to exposure, charged drops undergo a coulombic fission, exploding into an ensemble of smaller droplets. For large scale applications, when the liquid flow rate is larger than 1 L/min, the optimal way to charge a spray is the induction charging applied to a swirl atomiser nozzle [18]. The induction charging is effective if the fluid is sufficiently conductive to allow an efficient charge transfer to the droplets during their formation [18,19]. It means that the charge relaxation time, τ , has to be smaller than droplets formation time, τ_b [21]. Law estimated that the minimum liquid conductivity required for charging is 10^{-10} S/m [22].

The reference model for induction charging of hydraulic sprays indicated that the charge density acquired by the sprayed droplets depends on the intensity of the electric field acting on the liquid sheet and on its physical size, among all by its average thickness [21]. This parameter is hard to measure but can be estimated if the jet breakup length and the spray angle are available.

Laryea and No studied the jet breakup parameters as spray angle and breakup length by atomizing kerosene in a pressure-swirl hollow cone [23]. Their results underlined that electric forces led to a breakup length reduction and spray angle enlargement by increasing the applied voltage and the operating pressure. The authors proposed that these effects took place because they repelled each other modifying the spray trajectory and the equilibrium between electric and aerodynamic forces.

Marchant et al. electrified ordinary water by induction in a hydraulic nozzle and measured the distribution of spray volume by drop diameter in uncharged and charged conditions [24]. They found that droplet size distribution for the charged spray was different from that of the uncharged one. Indeed,

the authors reported a 3.8% reduction of droplets having size larger than 250 μm , arguing the occurrence of further atomization processes due to electrostatic breakup. Similarly, they indicated that droplets with size below 50 μm reduced by 1.5% since they are attracted by the electrode. However, Marchant et al. did not observed any relevant change on the jet breakup parameters of the charged spray [4,24]. In a recent paper, Jaworek et al. showed that droplets size distribution for electrified water jet did not changed significantly as a function on the applied voltage [25].

Our research group is developing new prototypes of electrified sprays for gas cleaning applications as component of the so called technology Wet Electrostatic Scrubbing (WES) [20,25–28]. This technology makes use of electrified sprays to induce electrostatic interactions between the droplets, the gas and the particles. It was found that WES system provided faster capture of acid gases and submicron particles compared to conventional wet scrubbers. This translates into higher removal efficiencies [17,26–30]. Thanks to its low cost, the affinity towards acid gases and the high conductivity, water is an appropriate candidate to WES processes. However, because of its ionic properties, the electrification of water sprays is more unstable than that of dielectric and/or organic liquids [16,25,31].

In light of the experimental evidences showed in Chapter 3, further studies on primary atomization of water sprays in presence of an electric field were conducted and they are discussed in this chapter.

4.2 Materials and methods

The experiments were performed in the lab-scale setup shown in Figure 3-1 in Chapter 3.

Experiments were carried out with tap water at $T=20^\circ\text{C}$, having conductivity of 0.75 S/m and pH 7.15.

Table 4-1 summarizes the chemical speciation of tap water ions.

Table 4-1- Chemical speciation of tap water

<i>Ion</i>	Formula	C, g/L
<i>Sodium</i>	Na^+	0.033
<i>Magnesium</i>	Mg^{2+}	0.026
<i>Calcium</i>	Ca^{2+}	0.111
<i>Potassium</i>	K^+	0.002
<i>Chloride</i>	Cl^-	0.008
<i>Bicarbonate</i>	HCO_3^-	0.535
<i>Carbonate</i>	CO_3^{2-}	-
<i>Sulphate</i>	SO_4^{2-}	0.011
<i>Bromide</i>	Br^-	-
<i>Fluoride</i>	F^-	-
<i>Nitrate</i>	NO_3^-	0.0042
<i>Phosphate</i>	PO_4^{3-}	0.0002

During the experiments, the height of nozzle tip from the middle plane of the electrode was set so that the breakup of the liquid sheet took place in correspondence of the ring horizontal place. The breakup length and the spray angle were optically measured by capturing at least 50 images of the liquid cone

by flash photography with a Nikon P500 bridge digital photo-camera (12.1Megapixels) conveniently focused and with time-exposure 1/1000 s. The images were not captured as a continuous sequence, but randomly for around 10 mins functioning. Experiments were repeated in triplicate during different days. The images were analysed through the software IMAGE PRO PLUS®. To calibrate the software, we used the nozzle dimension d_N , measured by a micrometric caliber, that was equal to $1 \text{ mm} \pm 5 \mu\text{m}$ for all the nozzles.

In literature, the breakup length can be measured in two possible ways by means of photographic analysis of sprays [7]. The first identifies the breakup length as the distance where the sheet displays the first hole perforation. The second define the breakup length as the distance at which the ligament formation occurs. In this study, we adopted the first method according to Dombrowski et al [12]. For the spray angle measurements, we referred to the lines which better fit the liquid-sheet profile, i.e. passing within the liquid peaks, as in Figure 4-1

The accuracy of the measurement depends on the pixel size: in our experiments, each pixel corresponds to a square of $35 \mu\text{m}$ side. Figure 4-1 is a sample image of the typical experimental picture of jet atomization in which the breakup length and spray angle are defined.

For the mean experimental values of breakup length and spray angle presented thereafter, the error of determination was within 4 % for the breakup length and 6 % for the spray angle.

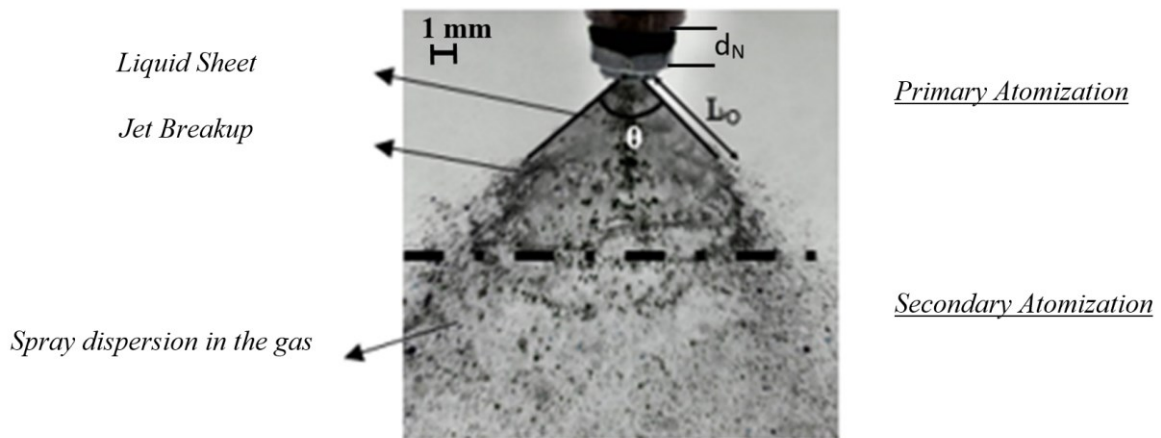


Figure 4-1- Liquid jet breakup mechanism for the nozzle BD5 at $P=3 \text{ bar}$ [32].

The tested nozzles were the 60 degrees (nominal) hollow cone BD5, BD8 and BD10 provided by Spraying Systems (USA). The nozzles were operated with pressures from 1 to 4 bar and water flow rates Q_L from 2.3 to 7.9 L/min. The three nozzles had similar geometric design, but different orifice size, d_0 , respectively equal to 3.2, 4 and 4.4 mm. Spray induction experiments were carried out by varying the charging potential that was set as negative from 0 kV up to -20 kV. It is worth noticing that for BD10 the tests cannot be performed above 9 kV because of the insurgence of electrical discharges: the increase of the spray angle caused a remarkable wetting of the charging ring leading to short circuits. The determination of experimental values for breakup length and spray angle allowed estimating the discharge coefficient, C_D , and the liquid jet velocity, v_{jet} , by resolving the system of equations (4.1-4):

$$C_D = \frac{Q_L}{\pi \frac{d_0^2}{4} (2 \rho_L P)^{0.5}} \quad (4.1)$$

$$v_{jet} = \frac{Q_L}{\rho_L \pi a_0 (a_0 - d_0)} \quad (4.2)$$

$$C_D = 1.17 \cdot \left[\frac{(1-X)^3}{1+X} \right]^{0.5} \quad (4.3)$$

$$X = \frac{(d_0 - 2a_0)^2}{d_0^2} \quad (4.4)$$

In this equation, ρ_L is the liquid density, a_0 is the film thickness at nozzle exit, X is the ratio between the air core area and orifice discharge area. Equations (4.1,2) are the geometric definitions of C_D and v_{jet} , while equations (4.3,4) are the Lefebvre approach to the calculation of the thickness a_0 . [9]

4.3 Results and discussion

Table 4-2 shows the trend of breakup length (L_0), spray angle (θ_0), jet velocity (v_{jet}) and discharge coefficient (C_D) with the atomization pressure, P , for the uncharged system. The spray regime according to Lefebvre is also reported where F and T indicate fully developed and almost fully developed regimes, respectively [9].

Table 4-2-- Experimental results in uncharged conditions

Nozzle	Parameters	P, bar					
		1	1.5	2	3	3.5	4
BD5	Q _L , L/min			3.2	3.9	4.27	4.6
	L ₀ , m			0.03	0.025	0.021	0.02
	θ ₀ , deg			67	68	68	70
	v _{jet} , m/s			15.55	18.98	20.64	22.15
	C _D , -			0.329	0.327	0.332	0.334
				F	F	F	F
BD8	Q _L , L/min		4.6	5.2	6.3		
	L ₀ , m		0.033	0.03	0.025		
	θ ₀ , deg		63	69.7	73		
	v _{jet} , m/s		15.55	15.78	19.26		
	C _D , -		0.342	0.342	0.338		
			F	F	F		
BD10	Q _L , L/min	4.6		6.4			
	L ₀ , m	0.0376		0.026			
	θ ₀ , deg	74		79			
	v _{jet} , m/s	11.32		15.9			
	C _D , -	0.354		0.348			
	Spray Regime	AF		AF			

The experiments showed that by increasing pressure (i.e. by increasing the liquid jet velocity), the spray angle slightly increased while the breakup length reduced because of the greater aerodynamic force acting on liquid sheet [3,9]. The liquid flow rate was proportional to pressure square root through the discharge coefficient, as in Equation (4.1). The discharge coefficient, C_D , was nearly constant with pressure and was about 0.34. The low values of C_D were due to the presence of air core in water spray because of the induced reduction of the effective flow area in the nozzle [7,17,18].

Senecal et al. considered the spray angle θ_0 as constant with the spray pressure and referred the effect of pressure on $L_{0,th}$ as inversely proportional to the liquid jet velocity, v_{jet} , according to the equation [8]:

$$L_{0, th} = \sqrt{\frac{\rho_L \cdot \sigma \cdot a \cdot \cos \theta_0}{\rho_g^2 \cdot v_{jet}^2}} \quad (4.5)$$

where ρ_g is the gas density, γ is the liquid surface tension and a is the liquid film thickness at breakup point and it is given by [8]:

$$h = \sqrt{\frac{12 \cdot \mu_L \cdot Q_L \cdot (1+X)}{\pi \cdot d_0 \cdot P \cdot (1+X)^2}} \quad (4.6)$$

where μ_L is the liquid viscosity.

Figure 4-2 shows the trends of the experimental breakup lengths as a function of the theoretical predictions of Senecal et al. calculated for the three nozzles [8].

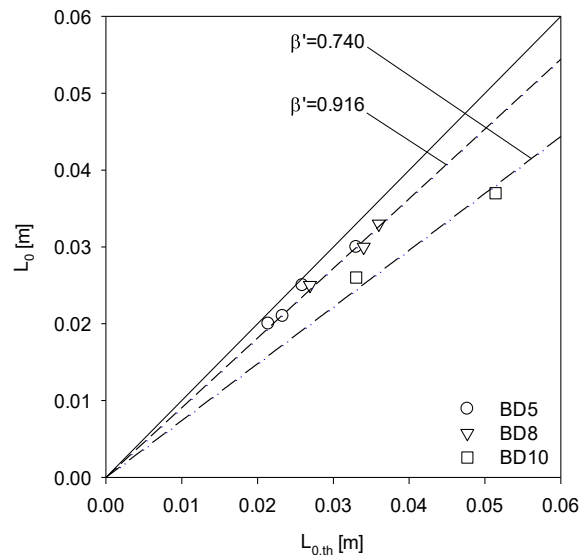


Figure 4-2- Breakup length as a function of the theoretical prediction for all tested nozzles.

Figure 4-2 shows that all data described a linear trend with a slope β that depends on nozzle. The factors β' were estimated by a linear regression with $R^2=0.98$ and they are equal to 0.916 ± 0.010 for BD5 and

BD8 and 0.740 ± 0.017 for BD10. This confirms the consistency of Senecal et al. [8] predictive model for our experimental conditions.

The BD10 showed the highest deviation from Senecal et al. model due to the pressure at which it was tested. In fact, the nozzle was performed at pressures at which the spray cone was not fully developed [8].

The left side of Figure 4-3 shows the ratio between the breakup length at different applied voltages, L_v , and the corresponding value estimated in absence of electric field, L_0 . The right side of Figure 4 shows the trend of the spray angle.

As a general rule, when the electric field is imposed to the electrode, the breakup length decreased with the charging potential, while the spray angle increased. Anyway, why the trend of L_v/L_0 is always a decreasing one, there are exceptions in the observed trend for the spray angle. Indeed, for BD10, for BD8 at $v_{jet}=19.26$ m/s ($P=3$ bar) and for BD5 at $v_{jet}=20.64$ m/s ($P=4$ bar), the variations of spray angle with voltage were almost negligible.

Indeed, the effect of charging potential over the spray angle can be considered as the results of the combined effects of the electrical repulsion, which tends to enhance the spray angle, and the inertial forces which helped preserving the initial spray angle. The effect of electric field was due to the high charge density that liquid sheet acquired for the induction effects. It caused the occurrence of repulsion forces that spread the liquid sheet away from the centreline of the spray.

Besides, the experimental results suggested that when the liquid jet velocity was higher (or that is the same, the inertia is higher), the intensive charge density on liquid sheet surface had a smaller effect on the spray angle, which remained similar to that observed under uncharged conditions.

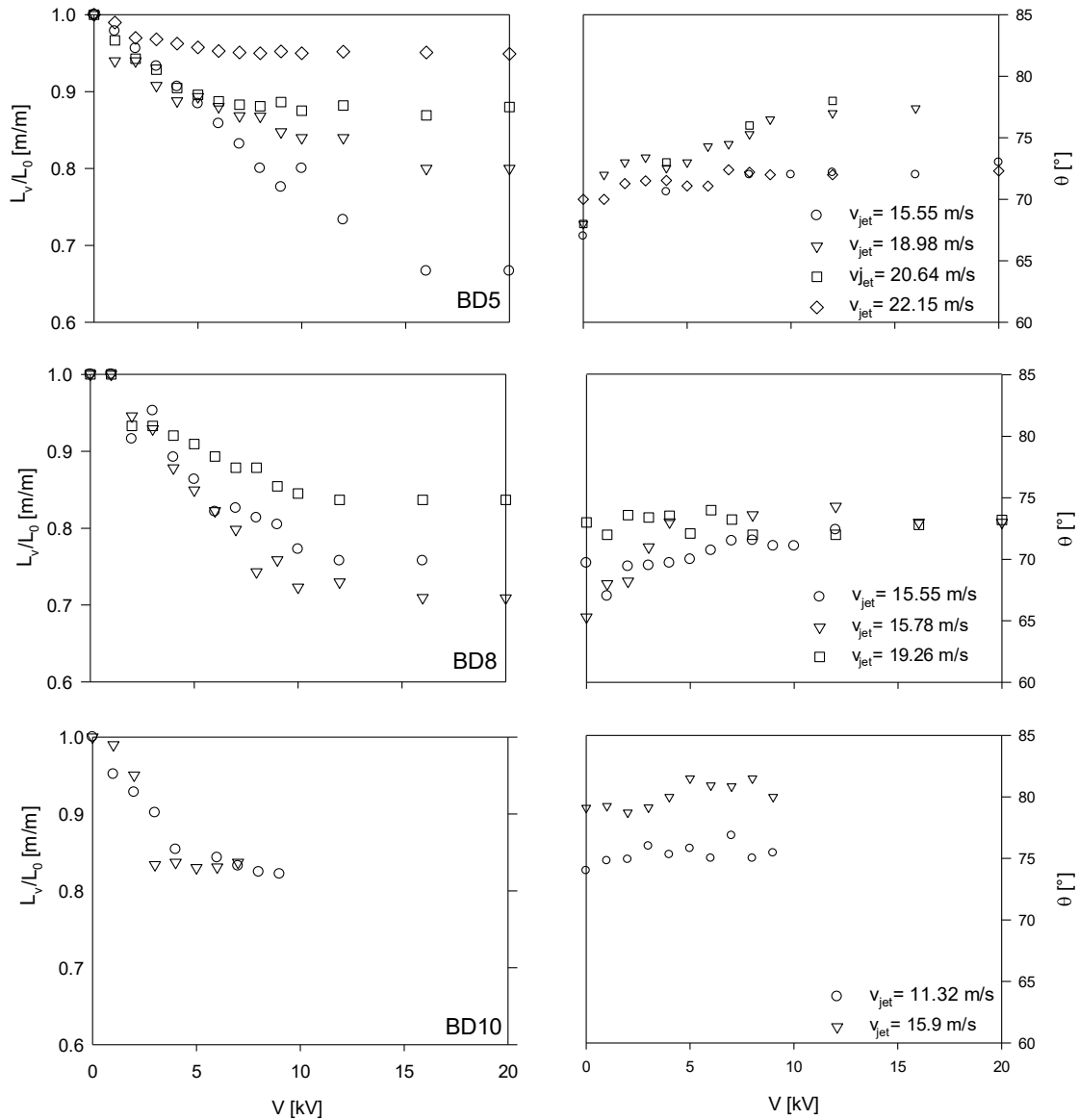


Figure 4-3- Experimental breakup length (left graphs) and spray angle (right graphs) as a function of charging potential at different pressures for BD5, BD8 and BD10

The experimental values on jet breakup length showed that the L_v decreased from L_0 until an asymptotic value, named $L_{V\infty}$, for a charging potential, V_∞ , higher of about 10 kV and dependent on the nozzle type and the atomization pressure.

The experimental results are analysed in terms of a new dimensionless parameter named ξ_{L_b} :

$$\xi_{L_b} = \frac{L_0 - L_v}{L_0 - L_{V\infty}} \quad (4.7)$$

The plot of ξ_{L_b} against the charging potential is shown in Figure 4-4. We observed that all the curves were well described by an exponential rise to maximum trend, according to the single parameter equation:

$$\xi_{L_b} = 1 - e^{-V/\phi} \quad (4.8)$$

The parameter Φ is a characteristic charging potential related to the onset of the asymptotic value of L_V at V_∞ . The values of Φ are reported in Table 4-3 with the corresponding values of $L_{V\infty}$ and V_∞ .

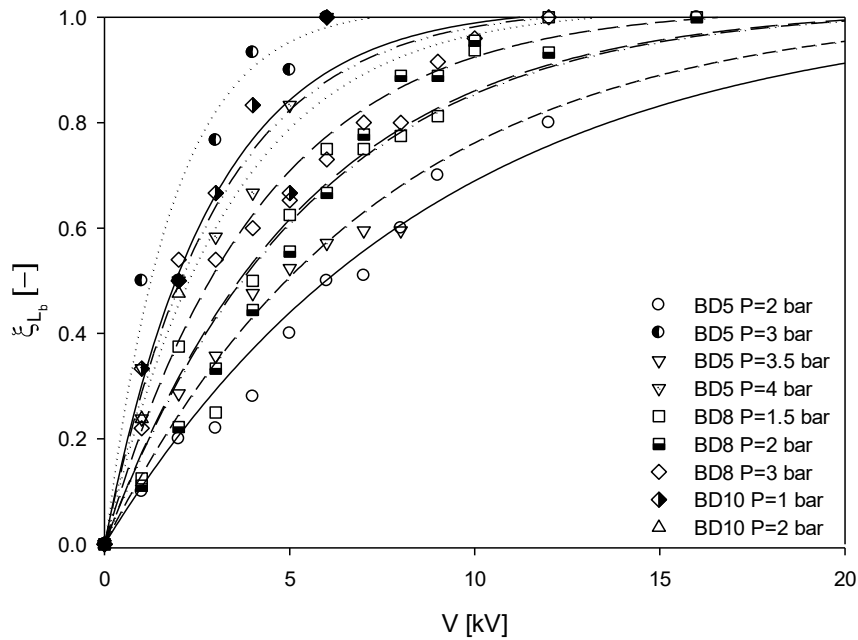


Figure 4-4-Breakup length variation trend with voltage and global curve regression.

Table 4-3-Values of the asymptotic values of the liquid jet breakup, $L_{V\infty}$, the asymptotic potential, V_{∞} , and of the characteristic charging potential, Φ for all tested nozzles together with the corresponding values of the standard error and the coefficients of correlation

Nozzle	Parameters	P, bar					
		1	1.5	2	3	3.5	4
BD5	L_{∞} , m			0.024	0.02	0.018	0.019
	V_{∞} , V			$1 \cdot 10^4$	$12 \cdot 10^3$	$9 \cdot 10^3$	$9 \cdot 10^3$
	Φ , -			$1 \cdot 10^4$	$5 \cdot 10^3$	$1 \cdot 10^4$	$1.6 \cdot 10^3$
	Err, -			$9.50 \cdot 10^{-6}$	$1.61 \cdot 10^{-5}$	$1.22 \cdot 10^{-5}$	$6.92 \cdot 10^{-6}$
	R^2 , -			0.96	0.95	0.91	0.94
BD8	L_{∞} , m		0.027	0.025	0.020		
	V_{∞} , V		$1 \cdot 10^4$	$12 \cdot 10^3$	$12 \cdot 10^3$		
	Φ , -		$5 \cdot 10^3$	$5 \cdot 10^3$	$5 \cdot 10^3$		
	Err, -		$1.65 \cdot 10^{-5}$	$1.65 \cdot 10^{-5}$	$2.26 \cdot 10^{-5}$		
	R^2 , -		0.95	0.96	0.95		
BD10	L_{∞} , m	0.030		0.021			
	V_{∞} , V	$1 \cdot 10^4$		$9 \cdot 10^3$			
	Φ , -	$5 \cdot 10^3$		$5 \cdot 10^3$			
	Err, -	$2.05 \cdot 10^{-5}$		$2.05 \cdot 10^{-5}$			
	R^2 , -	0.94		0.80			

According to the experimental results, Φ varied between 10 kV and 15 kV and may depend on the atomizing pressure.

Equation (4.8) can be implemented in light of Equation (4.5) to obtain a descriptive model to estimate the jet breakup length as a function of atomization pressure (or v_{jet}) and charging potential, when the values of β' , Φ and $L_{V\infty}$ are known.

$$L_0 = L_{V\infty} + (L_0 - L_{V\infty}) \cdot e^{-V/\phi} \quad (4.9)$$

where the breakup length L_0 can be expressed as:

$$L_0 = \beta' \cdot \sqrt{\frac{\rho_L \gamma \cdot a \cdot \cos \theta_0}{\rho_g^2 \cdot v_{jet}^2}} \quad (4.10)$$

From the experimental analysis of jet breakup, the parameters L_0 , V_{∞} , ϕ are known. Once these parameters are defined, Equation (4.9) provides a descriptive relation of exponential decay of breakup length under the influence of electric field.

In order to understand the physics behind these phenomena, we performed two qualitative analyses. Following the indication of previous studies on induction charging of sprays, we estimated the spatial profile of the electric field by using Comsol Multiphysics® [25,33]. We noticed that, at the V_{∞} , the electric field in the breakup point of the liquid sheet was always in the range $1.1-1.3 \cdot 10^5$ V/m. It seems that once this critical value of the electric field is approached, other phenomena take place and they

do not further alter the liquid sheet properties. Indeed, the electric field at V_{∞} is likely to be correlated to the occurrence of Townsend discharge phenomena [34–36]. The further increases in the charging potential above V_{∞} should initially led to dark discharges and, for even higher potentials, to corona discharge. During our experiments, we never showed corona discharges, but we noticed that the current provided by the HV supply progressively increased above V_{∞} . Indeed, this finding can be further confirmed by the observations reported by Manna et al. and Jaworek et al., which indicated that spay current reached a maximum in proximity of a charging potential corresponding to V_{∞} or close to it [20,25,26].

To further support these observations, we also performed a qualitative analysis of the spray images, noticing that the electric field ramped up the stretching of liquid sheet in terms of rising the frequency of the wavy oscillations (Figure 4-5). The images show how the frequency of wavy oscillation changes from 0 kV (a) to 20 kV (f). It seems that the peaks become smaller and uninterrupted as if the liquid surface was quite smooth.

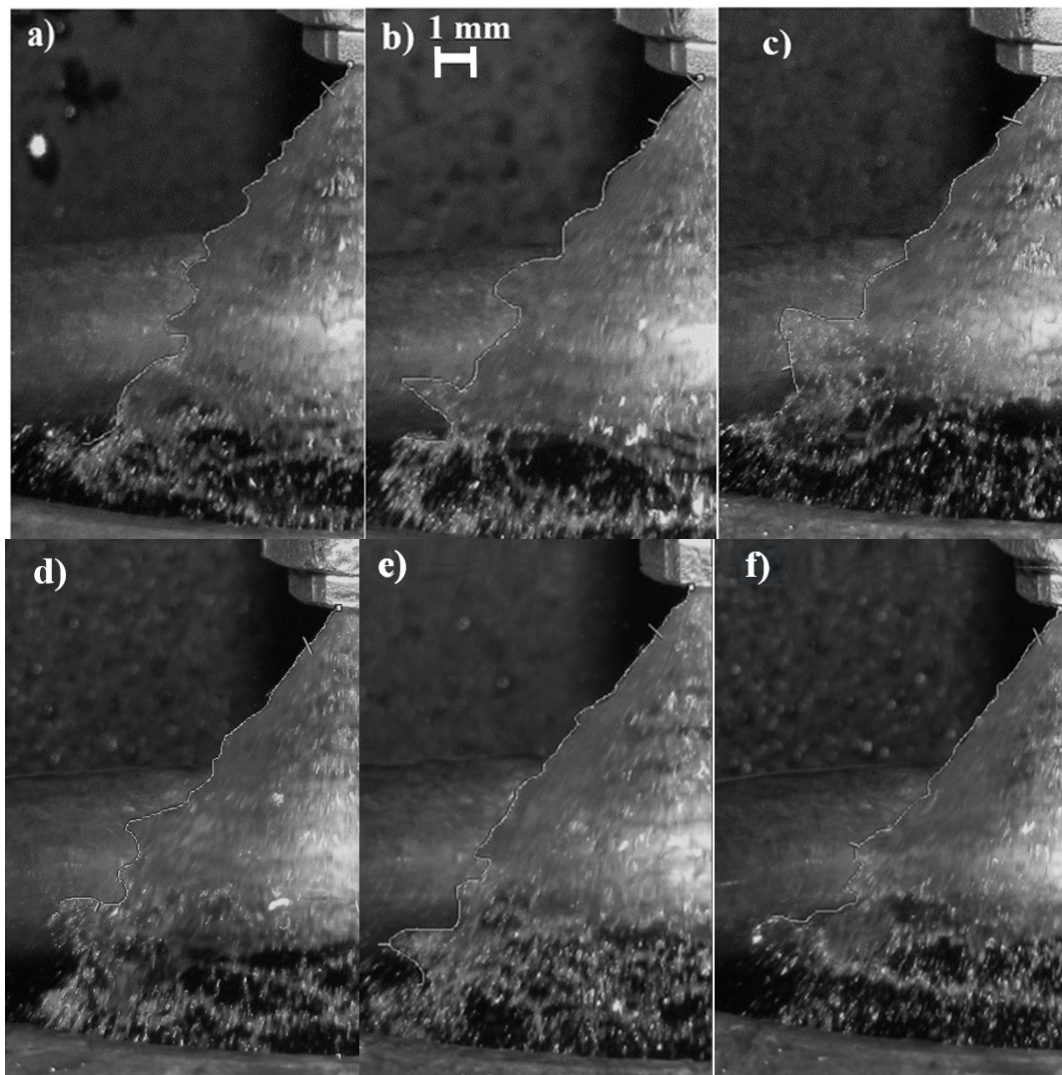


Figure 4-5-. Wave profile on liquid surface for nozzle BD5 at $P=2$ bar and rising charging potential $V=0$ kV (a), $V=4$ kV (b), $V=8$ kV (c), $V=12$ kV (d), $V=16$ kV (e) and $V=20$ kV (f).

This effect is the same occurring under the influence of pressure as described in the LISA model: the higher frequency mirrors the occurrence of faster wave growth, corresponding to a smaller breakup time and to a breakup of jet that takes place at lower distances from nozzle tip [3].

4.4 Summary

In this chapter, we reported the results of experiments on the breakup parameters of water sprays produced by hydraulic nozzles and electrified by induction charging. For the uncharged spray, the spray properties were well described by the Senecal et al. model [8].

When the electric field was applied, the spray angle generally increased due to of the repulsion of the charged droplets while the breakup length reduced up to an asymptotic value L_{vo} . This effect severely affect the charging efficiency of the spray and confirmed the observation of Laryea and No, in contrast with the results of Marchant et al [21–24,26].

Our experimental findings suggested that the electric forces induced on the liquid sheet generated an increment of the wavy oscillations and deformed the sheet so to enlarge the spray angle. We envisage that all the spray geometries observed for a given charging potential represented an equilibrium condition between the electric field effects, which tend to enlarge the spray and reduced the break up length, and the inertial forces, which acted to preserve its original shape. The higher the electric field, the higher the spray deformation. However, once the electric field approached a critical value, related to Townsend discharges, the energy provided by the HV supply is converted in ionic discharges and the actual forces exerted on the liquid sheet did not increase anymore, leading to the asymptotic values of L_{vo} and θ_{σ} .

In light of the indications achieved with these experiments, we believe that a detailed electrohydrodynamic study on the liquid jets of induction charged sprays are needed to definitely provide a physical description of this process. In the next chapter, indeed, the experiments carried on an electrospray unit are reported.

4.5 References

- [1] A. Jaworek, A. Krupa, “Charged Sprays Generation and Application,” *Sprays: Types, Technology and Modelling*, Maria C. Vella, Nova Science Publishers, Inc., New York, 2011, p. 1–100.
- [2] C. Dumouchel, “On the experimental investigation on primary atomization of liquid streams,” *Exp. Fluids*, vol. 45, no. 3, pp. 371–422, 2008.
- [3] N. Ashgriz, *Handbook of atomization and sprays: theory and applications*, 1st edition, Springer, New York, 2011.
- [4] J. A. Marchant, A. J. Dix, And J. M. Wilson, “The Electrostatic Charging Of Spray Produced By Hydraulic Nozzles: Part I. Theoretical Analysis,” *J. Agric. Eng. Res.*, Vol. 31, No. 4, Pp. 329–344, 1985.
- [5] Q. Fu, L. Yang, Y. Qu, B. Gu, *J. Propuls. Power*, 2010, 26, 955.
- [6] D. P. Schmidt, I. Nouar, P. K. Senecal, C. J. Rutland, J. K. Martin, R. D. Reitz, “Pressure-Swirl Atomization in the Near Field,” *SAE Tech. Pap.*, vol. 1999, no. 1999-1–496, 1999.
- [7] Q.-F. Fu, L.-J. Yang, W. Zhang, K.-D. Cui, *Atomization Sprays*, 2012, 22, 431.
- [8] P. K. Senecal, D. P. Schmidt, I. Nouar, C. J. Rutland, R. D. Reitz, And M. L. Corradini, “Modeling High-Speed Viscous Liquid Sheet Atomization,” *Int. J. Multiph. Flow*, Vol. 25, No. 6–7, Pp. 1073–1097, 1999.
- [9] A. H. Levebvre, *Atomization and Sprays*, 1st edition Hemisphere Publishing Corporation, London, 1989.
- [10] Z. Han, S. Parrish, And R. D. Reitz, “Modelling Atomization Processes Of Pressure-Swirl Hollow-Cone Fuel Sprays,” *At. Sprays*, Vol. 7, Pp. 663–684, 1997.
- [11] H. B. Squire, “Investigation Of The Instability Of A Moving Liquid Film,” *Br. J. Appl. Phys.*, Vol. 4, No. 6, Pp. 167–169, 2002.
- [12] C. J. Clark and N. Dombrowski, “Aerodynamic Instability and Disintegration of Inviscid Liquid Sheets,” *Proc. Roy. Soc. Lond. A*, vol. 329, p. 467, 1972.
- [13] N. Dombrowski, P. C. Hooper, *Chem. Eng. Sci.*, 1962, 17, 291.
- [14] A. Hussein, M. Hafiz, H. Rashid, A. Halim, W. Wisnoe, S. Kasolang, *J. Teknol. Sciences Eng.*, 2012, 58, 1.
- [15] N. Dombrowski, W. R. Johns, *Chem. Eng. Sci.*, 1963, 18, 203.
- [16] O. Lastow and W. Balachandran, *J. Electrostat.*, 2007, 65, 490.
- [17] W. Balachandran, A. Jaworek, A. Krupa, J. Kulon, and M. Lackowski, “Efficiency of smoke removal by charged water droplets,” *J. Electrostat.*, vol. 58, no. 3–4, pp. 209–220, 2003.

- [18] A. Jaworek, A. Krupa, A.T. Sobczyk, A. Marchewicz, M. Szudyga, T. Antes, W. Balachandran, F. Di Natale, C. Carotenuto, *J. Electrostat.*, 2013, 71, 345.
- [19] J. L. Hensley, X. Feng, and J. E. Bryan, "Induction charging nozzle for flat fan sprays," *J. Electrostat.*, vol. 66, no. 5–6, pp. 300–311, 2008.
- [20] L. Manna, F. Di Natale, C. Carotenuto, and A. Lancia, "Electrified water sprays generation for gas pollutants emission control," *Chem. Eng. Trans.*, vol. 52, 2016.
- [21] G. Artana, L. C. Bassani, and R. Scaricabarozzi, "Specific charge of induction electrified sprays," *J. Electrostat.*, vol. 29, no. 2, pp. 127–145, 1993.
- [22] S. E. Law, "Agricultural electrostatic spray application: a review of significant research and development during the 20th century," *J. Electrostat.*, vol. 6, pp. 25–42, 2001.
- [23] G. N. Laryea and S. Y. No, "Spray angle and breakup length of charge-injected electrostatic pressure-swirl nozzle," *J. Electrostat.*, vol. 60, no. 1, pp. 37–47, 2004.
- [24] J. A. Marchant and R. Green, "An electrostatic charging system for hydraulic spray nozzles," *J. Agric. Eng. Res.*, vol. 27, no. 4, pp. 309–319, 1982.
- [25] A. Krupa, A. Jaworek, A. T. Sobczyk, A. Marchewicz, M. Szudyga, And T. Antes, "Charged Spray Generation For Gas Cleaning Applications," *J. Electrostat.*, Vol. 71, No. 3, Pp. 260–264, 2013.
- [26] L. Manna, F. Di Natale, S. Caserta, A. Lancia, "Induction Charging of Water Sprays", *27th European Conference on Liquid Atomization and Spray Systems*, University of Brighton, 2016, Brighton, 4-7 September 2016.
- [27] F. Di Natale, C. Carotenuto, L. D'Addio, A. Jaworek, A Krupa, M. Szudyga A. Lancia, *J. Environ. Chem. Eng.*, 2015, 3, 349.
- [28] F. Di Natale, C. Carotenuto, L. Manna, M. Esposito, F. La Motta, L. D'Addio. A. Lancia, *Int. J. Heat Technol.*, 2016, 34, S597.
- [29] W. Balachandran, A. Krupa, W. Machowski, And A. Jaworek, "Smoke Precipitation By Charged Water Aerosol," *J. Electrostat.*, Vol. 51–52, No. 1–4, Pp. 193–199, 2001.
- [30] L. D'Addio, F. Di Natale, C. Carotenuto, W. Balachandran, and A. Lancia, "A lab-scale system to study submicron particles removal in wet electrostatic scrubbers," *Chem. Eng. Sci.*, vol. 97, pp. 176–185, Jun. 2013.
- [31] S. E. Law, "Embedded- Electrode Electrostatic-Induction Spray-Charging Nozzle: Theoretical And Engineering Design," *Trans. Asae*, Vol. 21, No. 6, Pp. 1096–1104, 1978.
- [32] <http://www.spray.com>

- [33] COMSOL Multiphysics[®], 5.0, COMSOL, Stockholm, 2015. <https://www.comsol.it/products>
- [34] K. Adamiak, P. Atten, *J Electrostat.* 2004;61, 85.
- [35] K. Yamada, K., *J Appl Phys.*, 2004; 96, 2472.
- [36] J.D. Cobine, *Gaseous Conductors: Theory and Engineering Applications*, 2nd edition, Dover Publications, New York; 1958.
- [37] O. Lastow, *Numerical and Experimental Study of Electrohydrodynamic Atomization of Aqueous Liquids*, PhD thesis, Brunel University, London, 2007.
- [38] H.T. Yang, S. Viswanathan, W. Balachandran, M.B. Ray, *Environ Sci Technol.*,2003, 37, 2547.
- [39] A. Gomez, K. Tang, *Phys Fluids*,1994, 6, 404
- [40] K. Tang And A. Gomez, "Generation Of Monodisperse Water Droplets From Electrospays In A Corona-Assisted Cone-Jet Mode," *J Colloid Interface Sci*, Vol. 175, No. 2, Pp. 326–332, 1995.
- [41] J.A. Cross, J.C.W. Fowler, G. Fu, *Electrostatic Enhancement of Water Sprays for Coal Dust Suppression*, The Health and Safety Trust, Sydney,2003.

Chapter 5. Electrohydrodynamic Atomization of water in the simple-jet mode with whipping breakup⁴



pic by L. Manna & F. Karithi

⁴This chapter is based on a publication on submission “*Electrohydrodynamic Atomization of water in the simple-jet mode with whipping breakup*”

5.1 Introduction

Spray technologies have been widely studied over the years for applications in chemical and mechanical engineering processes which require the dispersion of liquid droplets in a gaseous stream [1]. A liquid can be atomized into droplets by different ways that differ basically according to the type of energy transferred to the liquid, e.g. kinetic, ultrasonic, electric [2]. In the latter case, the combination of hydrodynamic and electrostatic forces change the jet breakup mechanism and generate charged droplets with improved dispersion in the gas phase [3]–[5]. This atomization technique is denoted as Electrohydrodynamic Atomization (EHDA) or Electrospray. It is based on the disruption of a liquid jet under the influence of an intense electric field ($\text{kV}\cdot\text{cm}^{-1}$).

For an uncharged spray, the breakup of a jet into droplets is dictated basically by the balance between inertial force and the surface tension. In this case, the breakup mechanism can be classified based on the liquid Weber number, which is the ratio between inertial forces and surface tension [6]. According to the literature [7], normally for Weber numbers below 1 the droplet's formation mechanism is denoted as “dripping regime”; on the contrary the “jetting regime” is established when the Weber number is larger than 4. In between these two regimes, the mechanism is denoted “transition regime” [8]. When an electric field is applied, the breakup mechanism is modified giving rise to different spray morphologies known as electrospray modes.

For Weber numbers comparable with the “dripping regime”, the electrospray modes that could take place are the enhanced dripping mode, the microdripping mode and the cone-jet mode [7]. At Weber numbers comparable with the jetting regime, instead, the electrospray mode is the simple-jet mode [7]. EHDA in the cone-jet mode is the most studied one because it generates nano and micrometer size droplets, monodispersed, which are crucial for many industrial applications as drug delivery [9], mass spectrometry [10], bipolar coagulation [11] or thin layer deposition [12]. However, this mode operates with small flow rate ($\mu\text{L}\cdot\text{h}^{-1}$), which makes its use rather challenging for many industrial applications as gas cleaning, or water treatment. To overcome this limitation, some researchers focused on the simple-jet mode [2], [4]. As mentioned above, for the same set-up geometry, the simple-jet mode happens as soon as a strong electric field is applied but at liquid flow rates compatible with the jetting regime. Both electrospray modes produce fine droplets but, in the cone-jet mode, they are emitted from a liquid jet which elongates from the tip of a Taylor cone, while in the simple-jet mode, they are detached from the liquid jet which is formed directly at the nozzle tip [2]. Agostinho et al. [2] observed that the simple-jet mode has three main breakup mechanisms: varicose breakup, whipping breakup and ramified breakup. The former is comparable with the breakup mechanism of an uncharged jet in the jetting regime, but the presence of the electrical stresses can reduce the liquid jet radius, thus the droplet size as well [2]. The whipping breakup takes place when the electric stresses are high enough to create

off-axis instabilities of the jet. In the ramified breakup, secondary jets extend from the main one and each of them act as an electrospray [13].

Regarding the application of the simple jet mode with whipping breakup in different systems, Loscertales et al. [14] studied the whipping instability of an electrospray of glycerin immersed in a bath of hexane. The authors observed that non-symmetric perturbations happened due to the net charge distributed on the liquid jet: if the charge is non-uniformly distributed, the radial component of the electric field becomes predominant and the liquid jet starts whipping to find a new balance. Hohman et al [15], [16] conducted theoretical and experimental studies on the production of nanometer fibers by electrospinning. They found that for PEO/water solutions, the onset of electrospinning corresponded with the onset of whipping instability. The instability took place when the liquid jet surface charge (or current through the jet) overcame the varicose breakup and enhance the off-axes instability bending the liquid jet. Agostinho et al. [7] performed some tests with deionized water in the simple jet mode and studied how the droplets' size were influenced by the electric potential. The authors observed that as soon as the whipping breakup appeared, two distinct populations appeared. In this breakup, the Relative Standard Deviation (RSD) of the droplets' population is much larger than 0.2, thus the spray can be considered polydisperse [7].

It was also observed that in this breakup mechanism a large fraction of the generated droplets is much smaller than the nozzle inner diameter, which can be seen as an advantage for industrial applications that require, at the same time, high flow rates and small droplets [7].

Even though other authors have explored the *simple-jet mode with whipping breakup*, a clear description of the droplets' population in that regime as well as a more complete definition of the window where the mode takes place is still missing. Therefore, in this chapter, the results of experiments aimed on classifying the droplets' population, the electric current and the whipping window, using water as the spraying liquid are reported. Furthermore, the results were used to verify if such mode could be used for gas cleaning systems.

5.2 Materials and Methods

The experimental methods were divided into optical and electrical tests. The former was structured to analyze the droplets' populations and overall spray characteristics, e.g. spray modes, whipping window, droplet diameter, droplet circularity etc.; the latter to measure the electrical current of the electrospray, which allowed us later to calculate the electric and surface tension stresses ratio.

5.2.1 Materials

The experiments were conducted at lab-scale using the experimental rig shown in Figure 5-1.

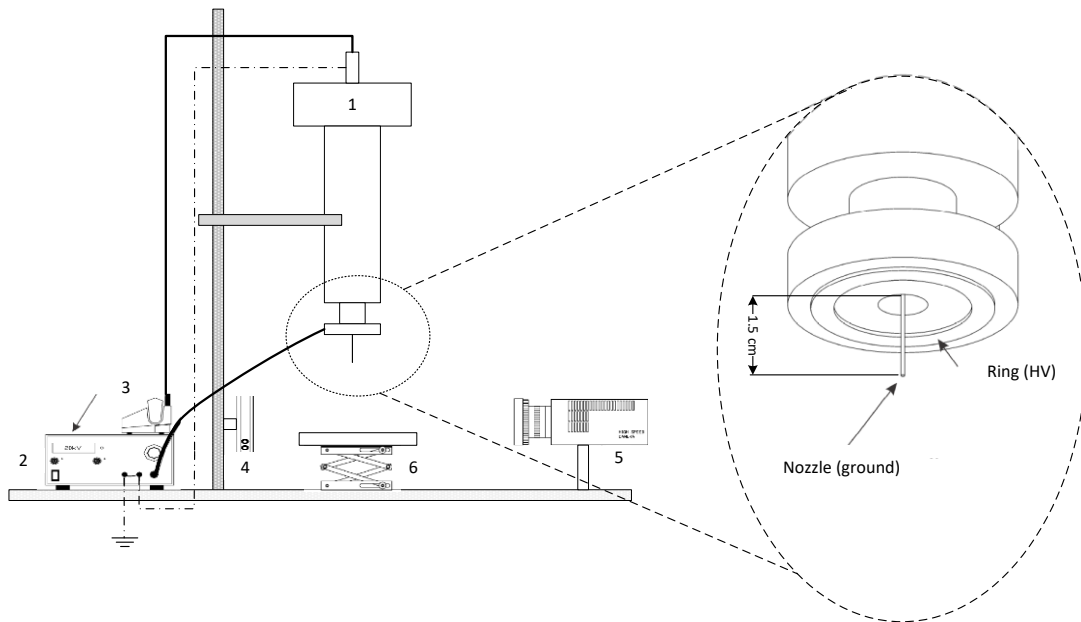


Figure 5-1- Experimental set-up 1: Electro spray unit; 2: High Voltage (HV) power supply; 3: Syringe pump; 4: Back light; 5: High-Speed Camera; 6: Water tank. Solid line: water; dash dot-line: Electric circuit

The electro spray unit (1) was made of an uncoated nozzle and a metallic ring with a diameter of 4 cm and thickness of 2 cm used as counter-electrode. Three different nozzles (EFD inc.) were used and hereinafter named N1, N2 and N3. The inner and outer diameter, d_i and d_o , were for the nozzle N1 410 and 720 μm , for nozzle N2 500 and 810 μm and for nozzle N3 610 and 910 μm , respectively.

The nozzle was placed in the middle of the ring in a way that the distance between nozzle tip and ring closer surface was kept at 1.5 cm (see details in Figure 5-1). In all conducted experiments, the nozzle was grounded, while the ring was connected to a High Voltage (HV) power supply (2), FUG model HCP 14-20000, set to negative polarity. The tests were performed with demineralized water (viscosity, μ , $1 \cdot 10^{-3}$ Pa·s, electrical conductivity, k , $5.5 \cdot 10^{-6}$ S·m $^{-1}$, density, ρ , $1 \cdot 10^3$ Kg·m $^{-3}$, surface tension, γ , $7.3 \cdot 10^{-2}$ N·m $^{-1}$ and electrical permittivity, ϵ , 80.1 F·m $^{-1}$). The liquid was pumped through the nozzle using a syringe pump (AITECS model PRO SP-125 (3)) and, after sprayed, it was collected in a grounded tank (6).

To characterize the *simple-jet mode* with *whipping breakup*, both the droplet population generated with this breakup and the ratio between the electrical and the surface tension stresses, observed when the whipping breakup appeared, were studied. In sequence, the methods used to characterize the droplet's population and the stresses ratio are described.

5.2.2 Experimental methods

The experiments were based in two different tests: the optical investigation of the spray and the electric current measurements. The spray electric current was measured using a digital multimeter (not shown in Figure 5-1) KEYSIGHT (model 34461A) connected in series between the nozzle and the power supply ground line. The optical tests were performed using a high-speed imaging system. This setup

was composed of a high-speed camera (FASTCAM model SA-X2) (5), a microscopic lens (NAVITAR 125X) and a backlight (DEDOCOOL 250W) (4), as shown in Figure 5-1.

As the main intention of the tests was to characterize the *simple-jet mode* with *whipping breakup*, the experiments were performed for each nozzle with three different Weber numbers namely, 3.16, 4.93 and 7.11. For each Weber number, the electric potential was varied from 0 kV (uncharged spray) until whipping conditions (≈ 17 kV). As noticed, the situation in which the Weber number is smaller than 4 (transition regime) was evaluated to provide information about *the simple-jet mode* inside this regime. To calculate the Weber number, the Eq.6.1 was used:

$$W_e = \frac{\rho \cdot d_i \cdot v^2}{\gamma} \quad (5.1)$$

where v is the liquid velocity evaluated at nozzle exit. It is worthy specifying that the Weber number was estimated for an uncharged spray.

As used by other authors [2], the electric potential was represented by the electric Bond number as in Eq. 6.2

$$B = \frac{\varepsilon \cdot V^2}{\gamma \cdot d_i} \quad (5.2)$$

where V is the electric potential.

During the optical measurements, an image sequence of around 2000 frames was captured for each test. For all images, the selected field of view was a rectangle of $30 \times 38 \text{ mm}^2$ where the nozzle was placed in the middle of it in a way that it would allow both the nozzle and the jet breakup point to be visible. In this region, the droplet surface deformation is still visible, which can affect the measured droplet diameter. To compensate the surface deformation after breakup, the major and minor Feret diameters of the droplet, a and b respectively (see Figure 5-2.2), were measured and the droplet volume was calculated as the one of an ellipsoid. The third axe of the ellipsoid was considered coincident with the minor axe. The final droplet diameter was considered as the diameter of a sphere with the same volume of this ellipsoid. Figure 5-2 indicates how the jet breakup length, L_j , the jet diameter, d_{jet} , the major, a , and minor, b , axes of a droplet were defined.

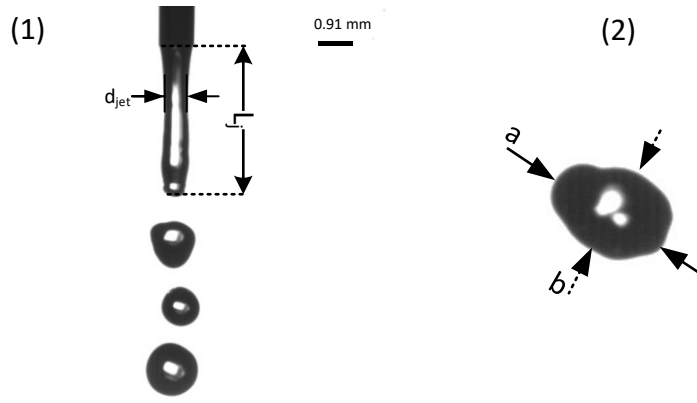


Figure 5-2-1) Jet parameters as jet diameter and breakup length; 2) major and minor axes of a droplet

As mentioned by Agostinho et al. [7], the droplets' population in the whipping breakup is rather polydisperse, which indicated the presence of sub-populations of droplets inside the whipping population. To identify and isolate each population, we used a Matlab routine (*fitgmdist tool*) which reconstructs the droplet size distribution as the super imposition of several gaussian-like subpopulations. Each sub-population was characterized in terms of average droplet diameter and standard deviation. Finally, the whole population was also analysed in a cumulative plot to quantify the percentage of each sub-population average diameter.

5.2.3 Imaging data post-processing

The experimental results in terms of droplet diameter d , electrical current I_{exp} were used to estimate the characteristics of the spray as the droplets circularity, C_i , the ratio R between the electrical stress developed on liquid jet and the surface tension stress, the number of droplets produced per seconds n , the interface area of droplets produced per unit time A_i . These parameters are defined as:

$$R = \frac{\sigma^2 / 2\epsilon_0}{\gamma / d_{jet}} \quad (5.3)$$

$$n = \frac{Q_L}{\sum_i \frac{\pi d_i^3}{6} \psi(d_i)} \quad (5.4)$$

$$A_i = n \cdot \sum_i \pi d s_i^2 \cdot \psi(d s_i) \quad (5.5)$$

where σ is the jet surface charge density, ϵ_0 is the vacuum electrical permittivity and d_{jet} is the jet diameter, d_s is the surface diameter and $\psi(d s)$ is the distributions of surface diameters, d is the volumetric diameter and $\psi(d)$ is the distribution of volumetric diameters.

The relation (5.3) was proposed by different authors [17]–[19] and, as suggested by Geers [17], the jet surface charge density could be expressed as function of electric current, I_{exp} , the liquid jet velocity v_{jet} and the jet circumference, C_j , as shown in Equation (5.6):

$$\sigma = \frac{l_{exp}}{v_{jet} \cdot C_j} = \frac{l_{exp}}{v_{jet} \cdot (\pi \cdot d_{jet})} \quad (5.6)$$

The liquid jet velocity was estimated assuming that it had the same velocity of the droplets immediately after the breakup [17]. The droplets' velocity was calculated by droplets' tracking in the imaging analysis. For a given liquid flow rate, the jet diameter was obtained once the liquid velocity was known.

5.3 Results and discussion

This section is divided in five paragraphs. Firstly, the experimental results obtained from both optical and electrical results are described. Secondly, the influence of whipping breakup on droplets' population and liquid jet stresses is discussed. Then the transition zone between the varicose and whipping breakup is analysed and at last, the spray characteristics in the simple jet mode with both varicose and whipping breakup are compared.

5.3.1 Experimental results

Figure 5-3 shows the breakup of an uncharged jet and the electrospray in the simple-jet mode for different Bond numbers for nozzle N2 and at $We=7.11$.

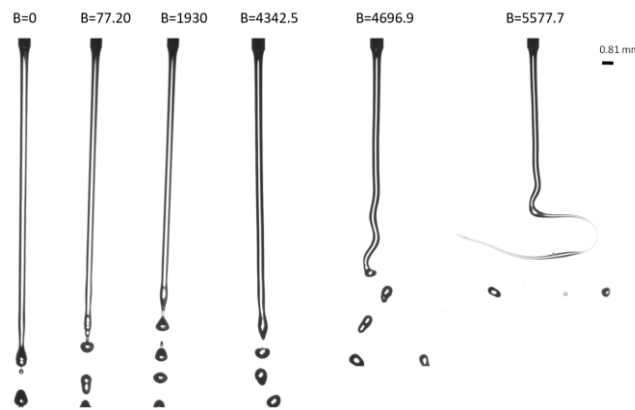


Figure 5-3- Sampling of droplets' images for nozzle N2 at $We=7.11$ and different Bond numbers

For an uncharged spray ($B=0$), according to Rayleigh theory [20], a stable liquid jet (with $d_{jet} \approx 0.55$ mm for the uncharged jet and $d_{jet}=0.44$ for the electrified jet) is formed at the nozzle tip and broke into droplets after a certain distance. For B between 77.20 ($V=2$ kV) and 4342.5 ($V=15$ kV), the electrospray is in the *simple-jet mode with varicose breakup*. In this case, it is observed that the liquid jet diameter remains constant while the breakup length is reduced for the higher value of Bond numbers. At $B=4696.9$ (15.6kV), the off-axes instabilities started to appear on the liquid jet and from this Bond value on, the electrospray happens in the *simple-jet mode with whipping breakup*. In this mode, the liquid jet whips following the electric field with a frequency increasing with the electric potential. Just before the whipping, at $B=4342.5$ the liquid jet started to bend indicating that the liquid jet is in the transition from varicose to whipping breakup. It means that a range of Bond values in which the liquid

jet breakup oscillates between the varicose and whipping breakup can be defined. By looking at Figure 5-3, the transition range is delimited at Bond values ranging from 4342.5 and 4696.5, which can be defined as Lower and Higher Bond numbers from imaging analysis, $B_{i,L}$ and $B_{i,H}$, respectively.

Figure 5-4 shows some characteristics of *the simple-jet mode with whipping breakup* for nozzle N1. The picture (5-4-A) is a superimposition of 100 frames, while the picture (4-B) is obtained by superimposing 500 frames. Both figures allow showing that both big and very small droplets are produced in this breakup mechanism.

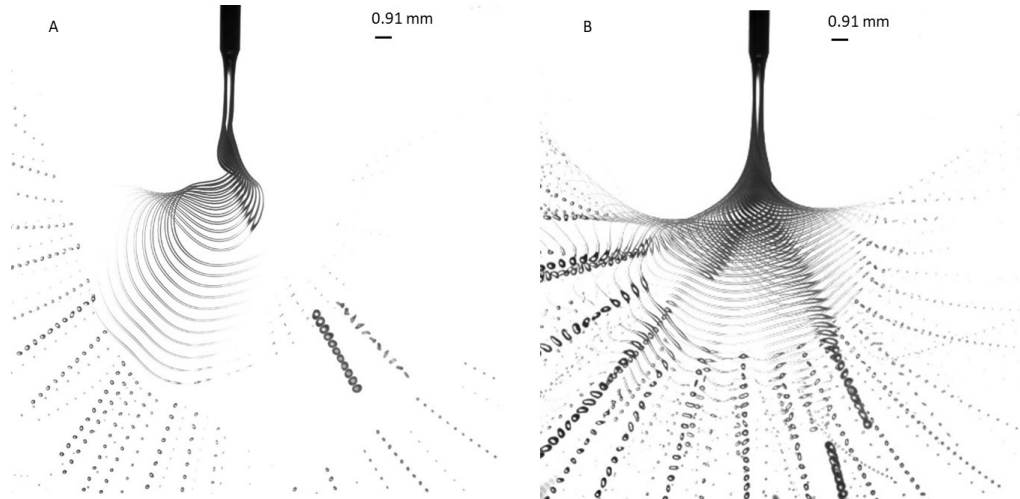


Figure 5-4- Superimposition of 100 frames (A) and 500 frames (B) at $We=7.11$ and $B= 5295.8$ for N1

The changing of breakup mechanisms with the intensity of the electric field can be observed through the droplets' size distributions. Figure 5-5 shows the Probability Density Functions for $We= 7.11$ and for B ranging from 0 to 5577.7 for nozzle N2. From the Figure 5-5, it is clear that the varicose regime droplets 'population is rather different from the whipping breakup population.

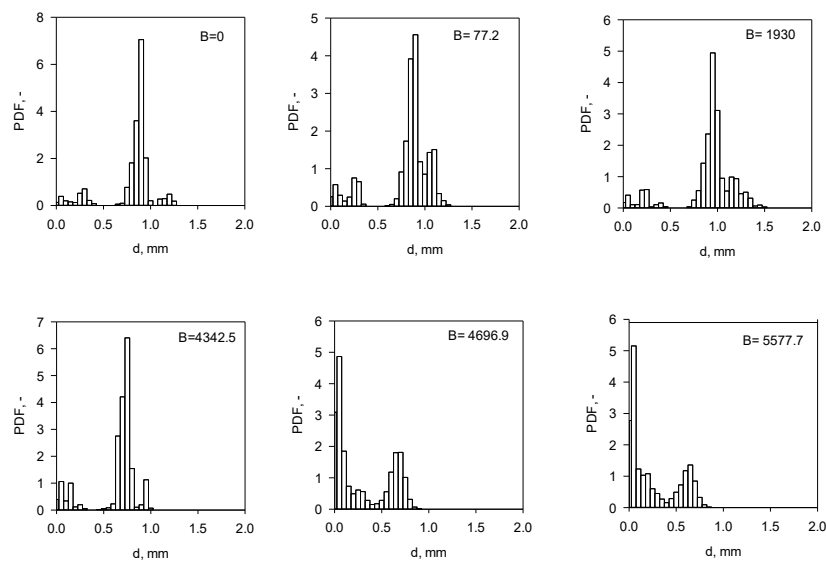


Figure 5-5- Probability Density Functions for N2 at $We= 7.11$ and at six different Bond numbers

If we observe the first three diagrams from $B=0$ to $B=1930$, they showed a predominant peak at a diameter of about 1 mm, and two small populations at $d=1.2$ mm and $d=0.3$ mm are formed. For $B=4343.5$, the PDF was quite similar to those at lower potentials with a main peak, which is slightly reduced slightly of 10% to a diameter of about 0.85 mm and a small population at $d=0.25$ mm is formed, while the droplets larger than 1 mm disappeared. All these diagrams are representing *the simple-jet mode with varicose breakup*.

The diagrams at $B=4696.9$ and 5577.7 in Figure 5-5 displayed a predominant droplets population at $d=0.04$ mm that is quite smaller than nozzle inner size (0.5 mm), and a second population at an average diameter slightly larger than 0.5 mm. It is worth remembering that the optical setup had a lower detection limit of 0.04 mm. Indeed, the droplets smaller than that size could not be detected by the high-speed camera and are thus not seen in the diagrams. At Bond values above 4696.6 ($V=15.5$ kV), the electrospay mechanism was the whipping breakup.

The Cumulative Density Function (CDF) may provide a better visualization of the droplets' population as a function of the applied electric potential. Figure 6-6 is the CDF for N1 at $We=7.11$ and for all tested Bond values (for electric potential V ranging between 0 and 17 kV).

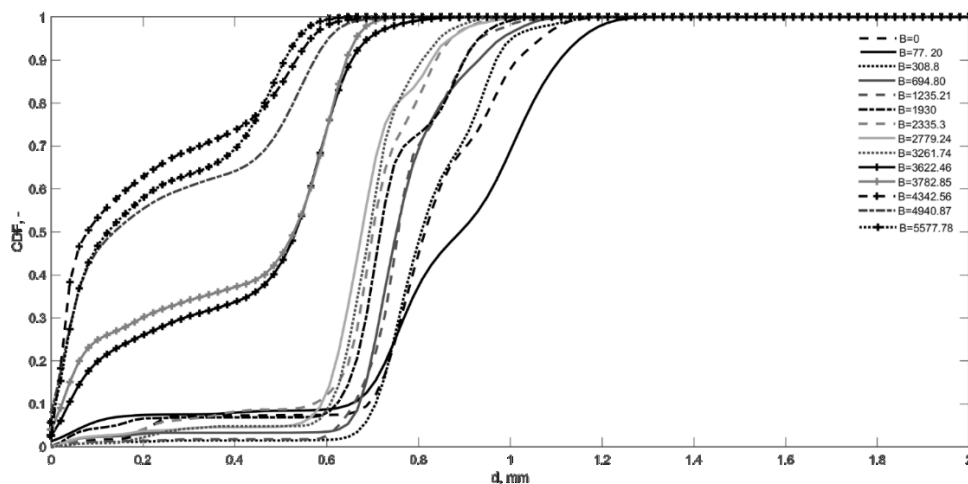


Figure 5-6- Cumulative Density Functions (CDFs) at different Bond numbers and at $We=7.11$ for N1

In Figure 5-6 three zones can be recognized. For B values between 0 and 3261.74 (Zone 1), the electrospay was run in the simple-jet mode with varicose breakup. In these cases, the CDFs had the typical sigmoidal shape but with inflection points mirroring the presence of multimodal distributions. At $B=3622.46$ and 3782.85 (zone 2), the first off-axis instabilities of whipping breakup appeared on the liquid jet and the shape of CDFs mirrors the presence of a droplets' population composed by smaller diameters. From $B=4342.5$ on (zone 3), the liquid jet has a whipping breakup and the droplets' distribution gathers droplets that are much smaller than the nozzle inner diameter. Similar results were observed for nozzles N2 and N3 (not shown in Figure 5-6). As mentioned in Figure 5-4, the zone 2

represents for nozzle N2 for $We=7.11$, and the Bond values 3622.46 and 3782.85 are the $B_{i,L}$ and $B_{i,H}$, respectively.

Figure 5-7 graphs the spray electric current versus the Bond numbers and at different Weber numbers for all three nozzles.

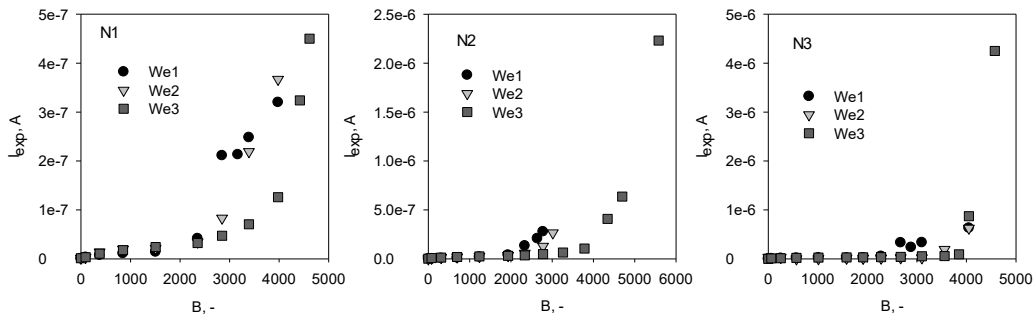


Figure 5-7- Electric current versus Bond number for nozzle N1, N2 and N3.

In the three diagrams, the electric current versus Bond number showed an exponential relation. For the same nozzle, the higher the Weber number, the smoother the exponential shape of curves. The point at which the electric current reached the highest values is the Bond number in correspondence with the onset of the whipping instability.

5.3.2 Influence of whipping breakup on droplet's population

When the spray moves from the varicose breakup to whipping breakup a clear effect on droplets' population appears. This effect was already shown in Figures 5-5.6 and now, in Figure 5-8, it is expressed in terms of the diameter d_{50} , which is the diameter corresponding to the 50% of the population. In this Figure, the d_{50} is plotted versus Bond numbers for different Weber numbers and for the nozzles N1-N2 and N3.

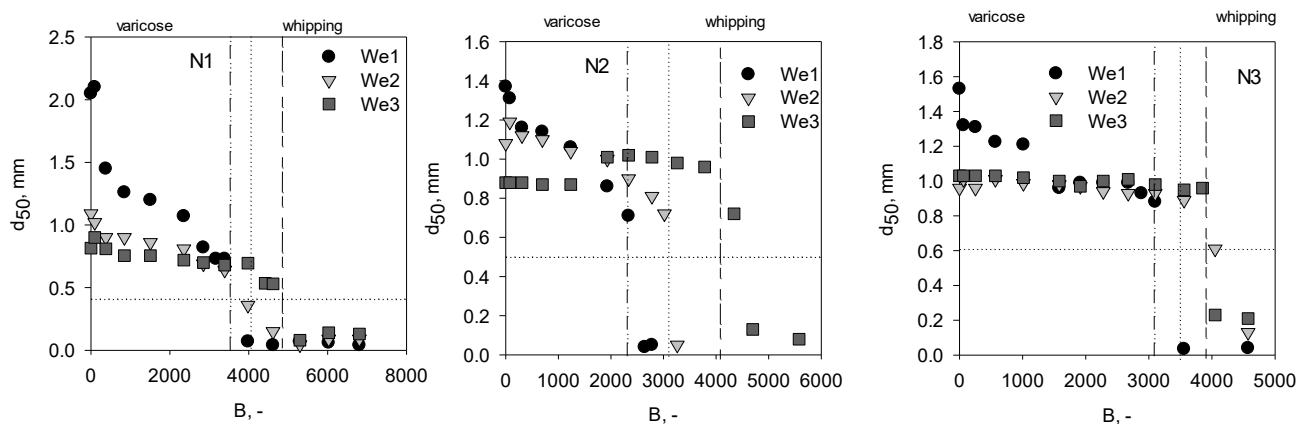


Figure 5-8- Diameter d_{50} versus Bond number for the three nozzles at different Weber numbers. Whipping line for $We=3.16$: Dash-dot-dot line; Whipping line for $We=4.93$: dot line; Whipping line for $We=7.11$: dot-dash line

As it can be seen, the d_{50} reduced as the Bond number increased, until the point at which it collapsed drastically and remained quite constant. In this point, the electropray mode changed from varicose breakup into whipping breakup. The varicose and whipping breakup zones are divided in graphs for each Weber number (e.g. different Weber numbers have different whipping starting points). In the three graphs, the horizontal reference line represents the nozzle inner diameter. As it can be observed, for whipping breakup, the d_{50} is normally much smaller than d_0 up to 70% smaller.

5.3.3 Influence of whipping breakup on liquid jet stresses

The parameter R is the ratio between the electrical and surface tension stresses acting on the liquid jet. It was estimated according to Eq. (5.3) in which the electric current was used to evaluate the jet surface density charge, σ .

Figure 5-9 graphs this ratio R versus the Bond numbers for different nozzles and Weber numbers.

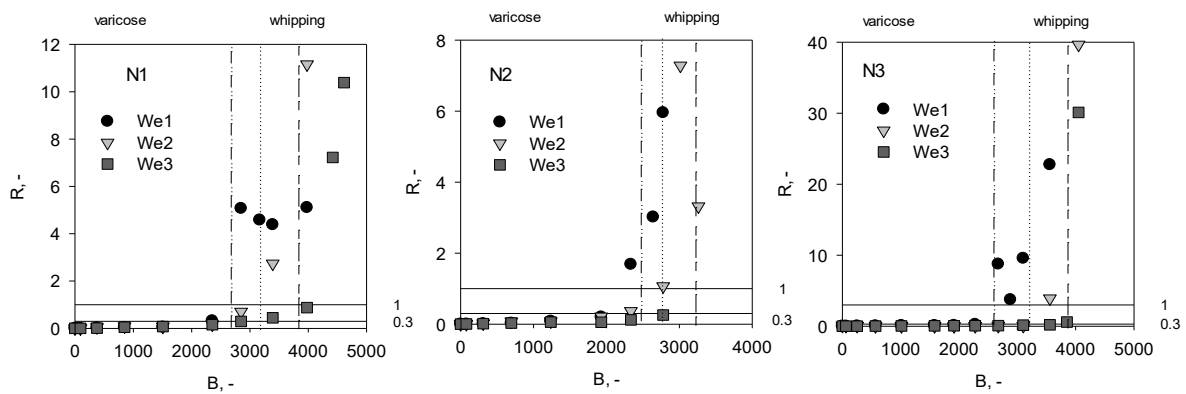


Figure 5-9- Ratio between the electrical and surface tension stresses, R , for different Weber and Bond numbers for the three nozzles N1, N2 and N3. Whipping line for $We=3.16$: Dash-dot-dot line; Whipping line for $We=4.93$: dot line; Whipping line for $We=7.11$: dot-dash line.

This result reflects the observations made by imaging analysis. Indeed, ratio R slightly increased with Bond number until when the ratio was 0.3 ± 0.05 . At this point, the whipping instabilities started to appear on the liquid jet, and it is consistent with former experiments [17]–[19]. The breakup mechanism was fully whipping when the ratio R become larger than 1. It means that there is transition region between the varicose breakup and the whipping breakup, as it was observed from imaging analysis. The Bond values at which $R=0.3$ and $R=1$ can be defined as lower and higher electrical bond number for whipping onset or $B_{e,L}$ and $B_{e,H}$, respectively. In Figure 5-9, the dividing line from varicose and whipping breakup is reported for all Weber numbers. As it can be seen, the transition started later at higher Bond numbers for increasing Weber values because of larger liquid inertia.

Once the breakup mode is whipping at $R > 1$, the ratio swiftly increased reaching values up to 40 (as for N3 and $We=7.11$) and, considering that this specific breakup mode requires very high electric potentials, the whipping breakup establishes with the corona onset. Some verification tests were done to verify this hypothesis. Optical tests were conducted in a black room for the operative conditions at

which the whipping breakup occurs. Figure 5-10 shows the liquid jet whipping breakup (left) and the corona fluorescence (right) observed for the same liquid jet.

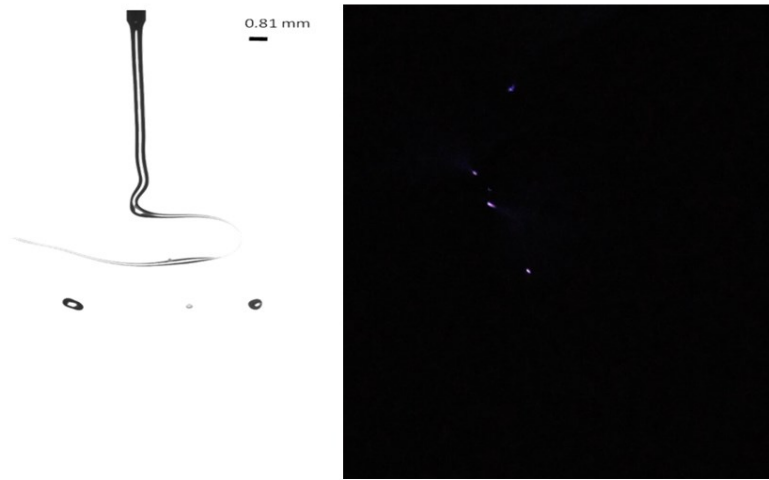


Figure 5-10- Liquid jet whipping breakup (left) and corona fluorescence (right) for N2 and We_3

5.3.4 Transition of the simple-jet mode from the varicose breakup to the whipping breakup

In light of the results showed in Figures 5-9, the transition of the electrospray mode from the simple-jet mode with varicose breakup towards the simple-jet mode with whipping breakup could be derived both from imaging tests and from the electric current (i.e. ratio R) tests. By using the inflection point of d_{50} curves and the criteria of $R > 0.3$ to define the transition B number for each Weber number, Table 5-1 lists for both electrical and optical analysis, the lower and higher values of Bond numbers at which the whipping instability started to appear and become fully developed, respectively. $B_{e,L}$ and $B_{e,H}$ denoted the lower and higher values of whipping transition observed from electric current trends, $B_{i,L}$ and $B_{i,H}$ indicated the lower and higher values of whipping transition observed from imaging analysis.

Table 5-1- Lower and higher values of Bond numbers for whipping transition observed from electrical and optical tests.

$We, -$	Nozzle	$B_{e,L}$	$B_{e,H}$	$B_{i,L}$	$B_{i,H}$
3.16	N1	1506.36	2847.96	2847.96	3977.739
4.94	N1	2353.69	3389.31	3389.31	3977.739
7.11	N1	3389.31	4613.23	3622.46	3782.85
3.16	N2	1930.02	2642.01	1235.21	2642.01
4.94	N2	2335.33	3015.74	2335.33	3261.74
7.11	N2	3261	2779.24	4342.5	4696.91
3.16	N3	2278.06	3100.7	1914.20	3559.47
4.94	N3	3559.47	4049.89	3559.47	4571.95
7.11	N3	3849.93	4571.95	3849	4049.894

The experiments indicated the absence of a sharp transition between the varicose and whipping breakup. It was not possible to find a correlation between Bond and Weber numbers but the range of values in which the whipping instability started to develop on the liquid jet, depended on the nozzle dimension too. Generally, for the three nozzles, the higher the Weber number, the higher the values of B_w . The discrepancy between the optical and electrical whipping Bond numbers reduced for larger Weber number.

5.3.5 Improved spray properties with the whipping breakup mechanism

The spray characteristics as droplets' circularity (evaluated from Image J), the numbers of droplets produced per seconds, n , and the interface area of the produced droplets, A_i , were estimated using Eq. (5.3-4). The obtained values are resumed in Figure 5-11.

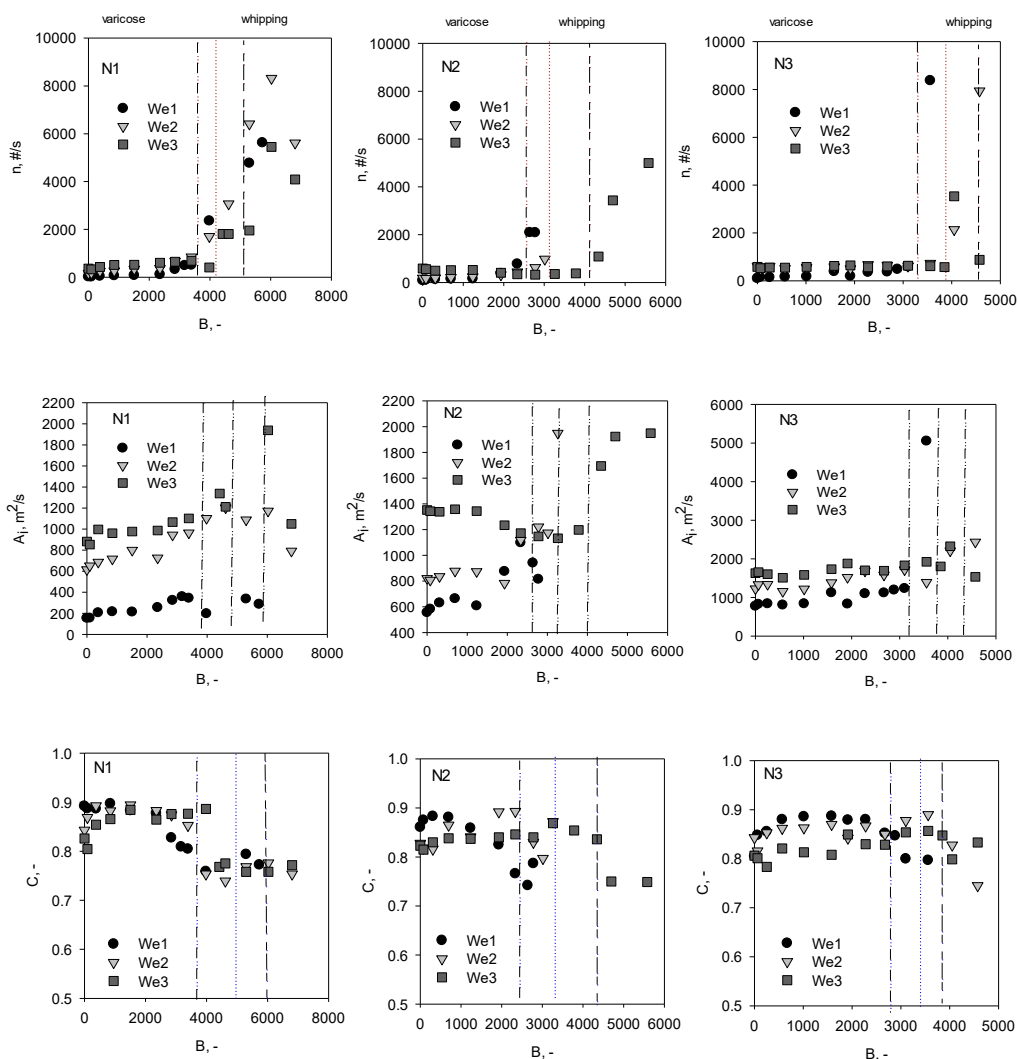


Figure 5-11- Number of droplets produced per second n , interface area of droplets A_i , circularity C , at different Bond and Weber numbers. Whipping line for We1: Dash-dot-dot line; Whipping line for We2: dot line; Whipping line for We3: dot-dash line.

As expected, the number of droplets emitted per second by the electro spray increased with the electric potential because the electric field accelerates the liquid jet breakup (the breakup time reduces) and the

atomization mechanism becomes faster. The number n rose swiftly at potentials in which the electro spray was run in the simple jet mode with whipping breakup. The reduction that was observed in some experiments for nozzles N1 and N3 at B larger than 5000 was probably caused by droplets that were not inside the field of view.

The interface area of droplets shifted towards higher values as the Weber number increased for the three nozzles. At same Weber number, it had larger values because of greater flow rate exerted with bigger nozzles. The interface area was almost constant in simple-jet mode with varicose breakup, while in the whipping breakup, the area A_i smoothly increased, and the increase was about 61%, 54% and 25% at We_1 , We_2 and We_3 , respectively, by comparing the value of A_i at potential soon after the whipping establishment and the value of A_i in the constant range. Similarly, the droplets circularity, C , ranged between 0.8 and 0.9 at low potentials and reduced to 0.7 for the whipping breakup. The reduction was more intense at low liquid flow rates thanks to the lower liquid inertia.

In summary, the whipping breakup gives rise to smaller and more deformed drops with a higher charge density compared to the varicose breakup. The production of very small droplets, charged, highly deformed is of primary interest for mass and heat transfer processes. For example, Di Natale et al. [20, 21] carried lab-scale experiments on SO_2 capture in a scrubber equipped with an electro spray unit running in dripping and transition mode. The authors found that when the droplets were charged and deformed, the mass-transfer coefficient were higher leading to a faster SO_2 absorption process.

5.4 Summary

In this section of the thesis, an experimental campaign on EHDA atomization in the simple-jet mode with whipping breakup was conducted. The electro spray unit was a nozzle-ring up configuration and three different nozzles were tested. The experiments were made with demineralized water at Weber numbers of 3.16, 4.94 and 7.11 and by varying the Bond number between 0 and 5000 (0 and 17 kV). It was observed that i) the droplets' size distributions were multi-modals with a predominant peak at a diameter similar to the nozzle outer one at low Bond numbers that shifted to a value much smaller than d_0 when the breakup mode was whipping; ii) the electrical current slowly increased with Bond number until the whipping instability took place on the liquid jet and at this condition the electric current rapidly increased; iii) the ratio R between the electric and surface tension stresses showed the same trend of the electric current and, accordingly with previous experiments, it became larger than 0.3 ± 0.05 when the transition to the whipping breakup started; iv) the spray characteristics as number of droplets per seconds, n , and the interface area of droplets, A_i , and droplets circularity, C , were influenced by the transition to the whipping breakup mechanism. The droplets were much smaller than inner nozzle diameter and highly charged and deformed.

Moreover, the experimental results revealed that the transition from varicose to whipping breakup did not take place sharply at a fixed value of Bond, but rather in a narrow range of Bond values meaning that the stretching of the liquid jet caused by the electric stress is a dynamic process, which leads to the onset of corona discharges, which generate a space charge and therefore an electric field more intense than the one emitted by the ring-electrode.

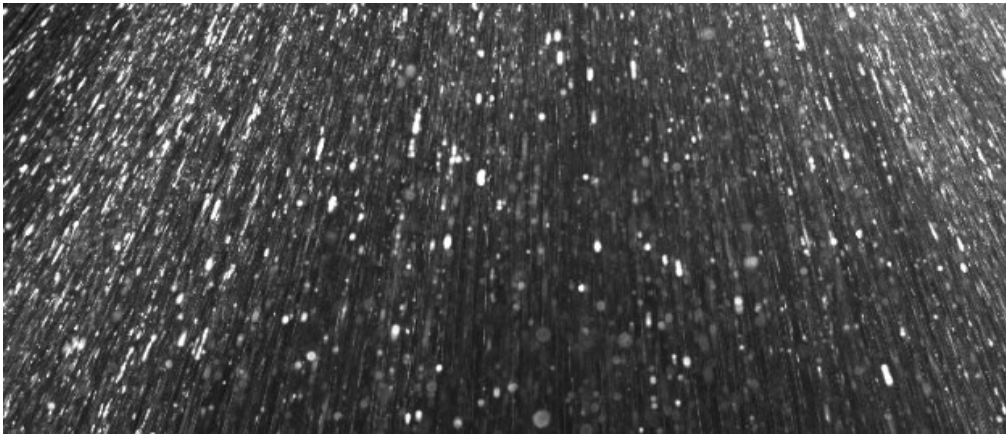
5.5 References

- [1] L. Manna, C. Carotenuto, R. Nigro, A. Lancia, and F. Di Natale, "Primary atomization of electrified water sprays," *Can. J. Chem. Eng.*, vol. 95, no. 9, pp. 1781–1788, Sep. 2017.
- [2] L. L. F. Agostinho, G. Tamminga, C. U. Yurteri, S. P. Brouwer, E. C. Fuchs, and J. C. M. Marijnissen, "Morphology of water electrosprays in the simple-jet mode," *Phys. Rev. E - Stat. Nonlinear, Soft Matter Phys.*, vol. 86, no. 6, pp. 1–9, 2012.
- [3] K. Tang and A. Gomez, "Generation of Monodisperse Water Droplets from Electrosprays in a Corona-Assisted Cone-Jet Mode," *J Colloid Interface Sci*, vol. 175, no. 2, pp. 326–332, 1995.
- [4] P. Miao *et al.*, "Morphology of water electrosprays in the simple-jet mode," *J. Aerosol Sci.*, vol. 25, no. 1, pp. 1–176, 2013.
- [5] O. Lastow and W. Balachandran, "Novel low voltage EHD spray nozzle for atomization of water in the cone jet mode," *J. Electrostat.*, vol. 65, no. 8, pp. 490–499, 2007.
- [6] J. Eggers and E. Villermaux, "Physics of liquid jets," *Reports Prog. Phys.*, vol. 71, no. 3, 2008.
- [7] L. L. F. Agostinho, B. Bos, A. Kamau, S. P. Brouwer, and J. C. M. Marijnissen, "Simple-jet mode electrosprays with water . Description , characterization and application in a single effect evaporation chamber ."
- [8] W. van Hoeve, S. Gekle, J. H. Snoeijer, M. Versluis, M. P. Brenner, and D. Lohse, "Breakup of diminutive Rayleigh jets," *Phys. Fluids*, vol. 22, no. 12, pp. 1–24, 2010.
- [9] K. Tang and A. Gomez, "Generation by electrospray of monodisperse water droplets for targeted drug delivery by inhalation," *J. Aerosol Sci.*, 1994.
- [10] P. Kebarle and L. Tang, "From Ions in Solution to Ions in the Gas Phase: The Mechanism of Electrospray Mass Spectrometry," *Anal. Chem.*, vol. 65, no. 22, 1993.
- [11] D. Camelot, J. C. M. Marijnissen, and B. Scarlett, "Bipolar coagulation process for the production of powders," *Ind. Eng. Chem. Res.*, vol. 38, no. 3, pp. 631–638, 1999.
- [12] B. Martinez-Vazquez, D. G. Sanchez, J. L. Castillo, K. A. Friedrich, and P. L. Garcia-Ybarra, "Scaling-up and characterization of ultralow-loading MEAs made-up by electrospray," *Int. J.*

Hydrogen Energy, vol. 40, no. 15, pp. 5384–5389, 2015.

- [13] L. L. F. Agostinho, B. Bos, A. Kamau, S. P. Brouwer, E. C. Fuchs, and J. C. M. Marijnissen, “Simple-jet mode electrosprays with water. Description, characterization and application in a single effect evaporation chamber,” *J. Aerosol Sci.*, no. October 2017, pp. 1–14, 2018.
- [14] G. Riboux, A. G. Marnín., I. G. Loscertales, and A. Barrero, “Whipping instability characterization of an electrified visco-capillary jet,” *J. Fluid Mech.*, vol. 671, no. December 2015, pp. 226–253, 2011.
- [15] M. M. Hohman, M. Shin, G. Rutledge, and M. P. Brenner, “Electrospinning and electrically forced jets . I . Stability theory Electrospinning and electrically forced jets . I . Stability theory,” *Phys. Fluids*, vol. 13, no. 8, pp. 2201–2220, 2001.
- [16] M. M. Hohman, M. Shin, G. Rutledge, and M. P. Brenner, “Electrospinning and electrically forced jets. II. Applications,” *Phys. Fluids*, vol. 13, no. 8, pp. 2221–2236, 2001.
- [17] K. B. Geers, “Application to Electrospray: from people to plants,” TU Delft, 2003.
- [18] D. Camelot, “The Bipolar Coagulation Process for Powder Production,” TU Delft, 1999.
- [19] R. P. A. Hartman, “Electrohydrodynamic Atomization in the Cone Jet Mode,” *Thesis*. p. 177, 1998.
- [20] L. R. F.R.S., “On the equilibrium of liquid conducting masses charged with electricity,” *London, Edinburgh, Dublin Philos. Mag. J. Sci.*, vol. 14, pp. 184–186, 1882.
- [21] F. Di Natale, C. Carotenuto, and A. Lancia, “Enhanced SO₂ removal by using charged water droplets,” *Chem. Eng. Trans.*, vol. 52, pp. 505–510, 2016.
- [22] F. Di Natale, C. Carotenuto, L. Manna, and A. Lancia, “Chemi-electro-hydrodynamic of sulphur dioxide absorption by electrified water drops,” *Chem. Eng. Trans.*, vol. 69, 2018.

Chapter 6. Secondary Atomization of Electrified Water Sprays⁵



pic by F. Di Natale

⁵ This chapter is based on the paper on submission: “*Secondary Atomization of Electrified Water Sprays*”

6.1 Introduction

The electrified sprays can be classified on charging mechanisms (i.e. corona charging, induction charging or contact charging/electrospray) [1]–[4] and on liquid flow rate.

The type of charging mechanism and the liquid flow rate are strictly correlated and define the optimum mechanism to charge the liquid spray. Indeed, for low-flow rate sprays (<mL/h), the contact charging/electrospray or induction charging are the most indicated [5]. The high-flow rate sprays (~L/min) are usually charged by induction for safety reasons [6], [7]. The corona charging is barely used on liquid sprays because of its low charging efficiency.

The combination of an electric field and a liquid spray has been widely studied for two main reasons: 1) the better dispersion of liquid droplets in gas phase, 2) the production of smaller droplets. The better dispersion is due to repulsion forces acting between the equally charged droplets and to the fact that, if small enough, the droplets are driven by the electric field lines. The reduction of droplets' size has been investigated and demonstrated for low-flow rate electrified sprays and at the moment several scaling laws to correlate droplet diameter and electrical current to electrical potential and flow rate have been extrapolated [12]–[14].

The high-flow rate electrified sprays started to be studied since industrial application required a higher flow rate as gas cleaning or injection systems [9], [10], [15]–[17]. These studies were focused on understanding how the droplet specific charge or droplet charge to mass ratio depended on the electric field [1], [16], [17] and few studies were about the influence of electric field on atomization process.

In previous studies, we started to verify if the presence of electric field influenced and change the atomization mechanism of a liquid spray [2]–[4]. Considering the atomization model described by Dombrovski et al. for pressure swirl hollow cones [20]–[24], we investigated the influence of applied electric potential on primary atomization of different sprays (e.g. length of breakup, spray angle). The experimental tests revealed an effective influence of the electric field on primary atomization parameters. We observed that the breakup length reduced with the applied electric potential and, at same time, the spray angle enlarged.

In this chapter, we continued the study by analysing the droplets' populations produced during the second atomization of same sprays. The results were correlated with the electrical current measured as in Chapter 3 to describe the droplets' parameters as a combination of atomization and electrification processes.

6.2 Materials and Methods

The experiments were performed in the lab-scale setup shown in Figure 3-1 in Chapters 3.

The tested nozzles were the 60 degrees (nominal) hollow cone BD5, BD8 and BD10 provided by Spraying Systems (USA). The nozzles were operated with pressures from 1 to 4 bar and water flow rates Q_L from 2.3 to 7.9 L/min. The three nozzles had similar geometric design, but different orifice size, d_0 , respectively equal to 3.2, 4 and 4.4 mm. Spray induction experiments were carried out by varying the charging potential that was set as negative from 0 kV up to -20 kV, except for some tests that were performed until -14 kV because of the insurgence of electrical discharges caused by the wetting of the charging ring leading to short circuits. Experiments were carried out with tap water at $T=20^\circ\text{C}$, having conductivity of 0.75 S/m and pH 7.15.

To characterize the droplets' population generated by the three nozzles a high-speed camera Phantom model Miro C110 was used. The optical lens was NIKKOR LENS AF-S 85 mm f1/8G and a macro ring pk11a was added. The light required by the camera was provided by a blue led produced by Thor Lab model LEDD1B.

6.2.1 Experimental methods

Considering that in previous studies the process of primary atomization of these kind of sprays has been already investigated [4], [7], the optical tests carried in this study aimed to obtain the size distribution of droplets produced during the second atomization in terms of Probability Density Functions (PDFs) or Cumulative Density Functions (CDFs). Figure 6-1 (left) is a typical image of the electrified spray global atomization process captured by means a Nikon P500 bridge digital photo-camera (12.1Megapixels) as in [4] in which is highlighted the zone of secondary atomization. At right it is reported a frame of secondary atomization droplets captured by means the high-speed camera.

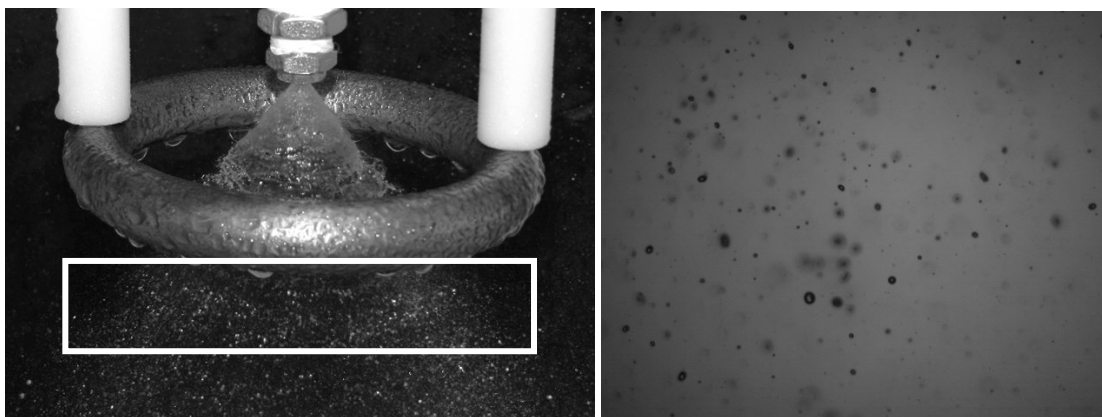


Figure 6-1- Atomization process of an hydraulic water spray (left) and secondary atomization droplets (right)

For each test, 4000 frames were recorded with an exposure time of $4\ \mu\text{s}$. The field of view was a rectangle $1280 \times 1024\ \text{mm}^2$ and the light was placed behind the spray in a way to avoid shadow zone as best as possible. The high-speed camera was focalized with a ruler of 28 mm that was used to calibrate the imagine analysis software, which was IMAGE J[®].

The accuracy of the measurement depends on the pixel size: in our experiments, each pixel corresponds to a square of 35 μm side. Considering that the droplets produced by an electrified spray could be deformed, the diameter of each droplet was estimated as the diameter of a sphere with the same volume of an ellipsoid. Indeed, from Image J, each droplet was analysed as an ellipse and the major and minor axes were measured to evaluate the volume of the ellipse and then the diameter of the equivalent sphere (as described in Chapter 5).

Once the diameters populations were obtained, the Matlab[®] tool of distribution fitting was implemented to get the PDFs and CDFs, as described in Chapter 6.

To understand how the presence of electric field influenced the atomization process, the ratio R was estimated. This parameter is the ratio between the electrical stress, τ_e , impressed to the liquid by the electric field, and the surface tension stress, τ_s :

$$R = \frac{\tau_e}{\tau_s} \quad (6.1)$$

The electrical stress, τ_e , is the ratio between the electrical force, F_e , and the surface on which the force is applied. In this evaluation the electrical stress was defined on lateral surface of liquid cone. It is expressed as:

$$\tau_e = \frac{F_e}{S} = \frac{q^2}{4\pi \cdot \epsilon_0 \cdot r_c^2} \cdot \frac{1}{\pi \cdot a \cdot r_c \cdot L_b} \quad (6.2)$$

where ϵ_0 is the vacuum permittivity, q is the liquid charge, a is the liquid cone thickness and it was considered as mean value between the liquid thickness at nozzle exit and at breakup point, evaluated from LISA model [23]. L_b is the breakup length, r_c is the liquid cone radius, and it was estimated geometrically known the breakup length and the half spray angle, $\vartheta/2$, as represented in Figure 6-2.

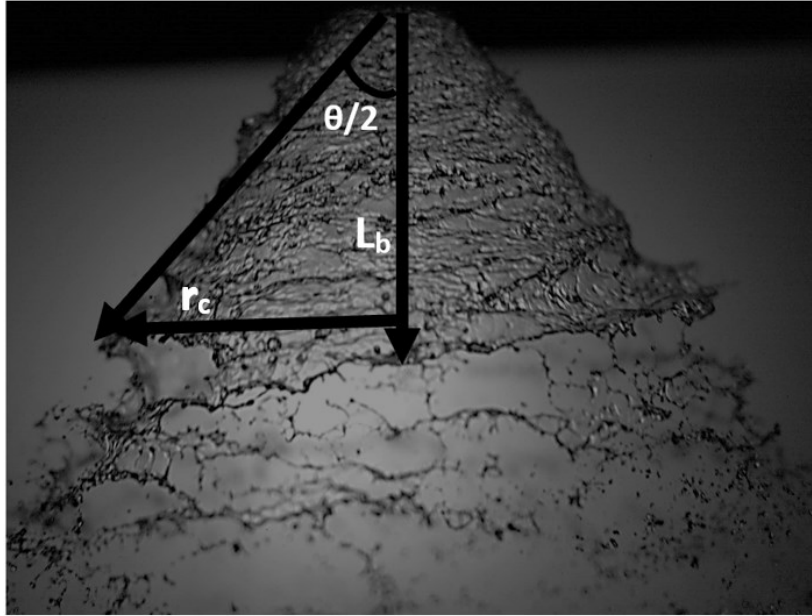


Figure 6-2. Representation of liquid cone parameters as cone radius, r , breakup length, L_b , and half spray angle, $\theta/2$.

Both the breakup length and the spray angle at different electric potentials were calculated in previous study and are shown in Chapters 3-4.

The electric charge, q , was expressed as function of volumetric density charge, σ_{vol} , and the volume of the cone, V_{cone} :

$$q = \sigma_{vol} \cdot V_{cone} = \left(\frac{I_{cone}}{Q_L} \right) \cdot \left(\frac{\pi \cdot r_c \cdot L_b \cdot \langle a \rangle}{3} \right) \quad (6.3)$$

where I_{cone} is the electrical current measured on grounded nozzle during the experimental procedure carried on same nozzles in previous studies [4], [7], Q_L is the liquid flow rate, $\langle a \rangle$ is the liquid sheet thickness as average between the a_0 and $a(V)$, where a_0 is the thickness for the uncharged spray estimated with Eq. 2.50, while $a(V)$ is the thickness at different electric potentials calculated with Eq. 2.48 in which the parameters $L_b(V)$ and $\theta(V)$ are experimentally evaluated.

Combining Equations (6.2) and (6.3), the electrical stress is expressed as:

$$\tau_e = \frac{I_{cone}^2 \cdot \langle a^2 \rangle \cdot L_b \cdot \cos\left(\frac{\theta}{2}\right)}{36 \cdot \epsilon_0 \cdot r_c \cdot Q_L^2} \quad (6.4)$$

The surface tension stress, τ_s , is the ratio between the force that the liquid exerts to acquire the least possible surface and the surface itself. We will refer the surface tension to the length of the liquid sheet at the breakup point, as:

$$\tau_s = \frac{F_s}{S} = \frac{2 \cdot \gamma}{2 \cdot \pi \cdot r_c} \quad (6.5)$$

where γ is the liquid surface tension for an uncharged spray.

The ratio R is thus expressed as:

$$R = \frac{\tau_e}{\tau_s} = \frac{\pi \cdot I_{cone}^2 \cdot \langle a^2 \rangle \cdot L_b \cdot \cos\left(\frac{\theta}{2}\right)}{36 \cdot \epsilon_0 \cdot \gamma \cdot Q_L^2} \quad (6.6)$$

6.3 Experimental results

Figure 6-3 shows the Probability Density Functions at different electric potentials for the nozzle BD8 at P=3bar and Q_L= 6.4 L/min.

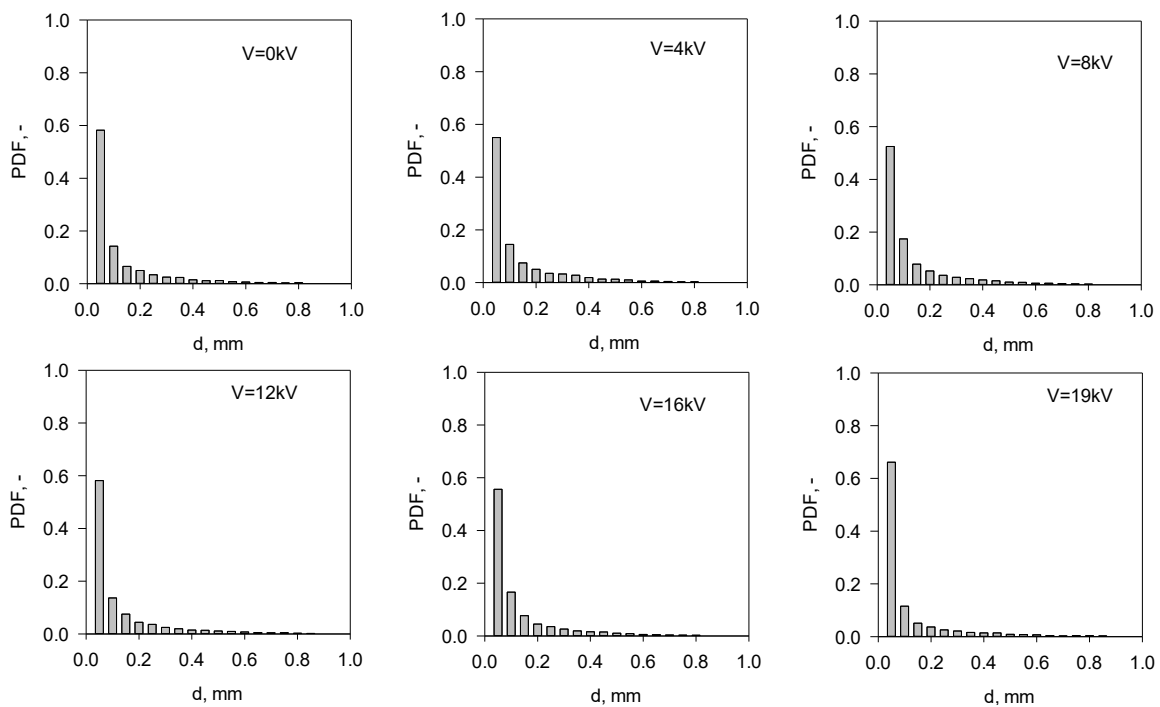


Figure 6-3- PDFs at different electric potentials for nozzle BD8 at P=3 bar

The PDFs were normalized on total number of droplets. The shape of each curve is the same at each electric potential and it seems that the presence of the electric field does not affect the droplets' size distribution.

Figure 6-4 graphs the Cumulative Density Functions of distributions showed in Figure 6-3.

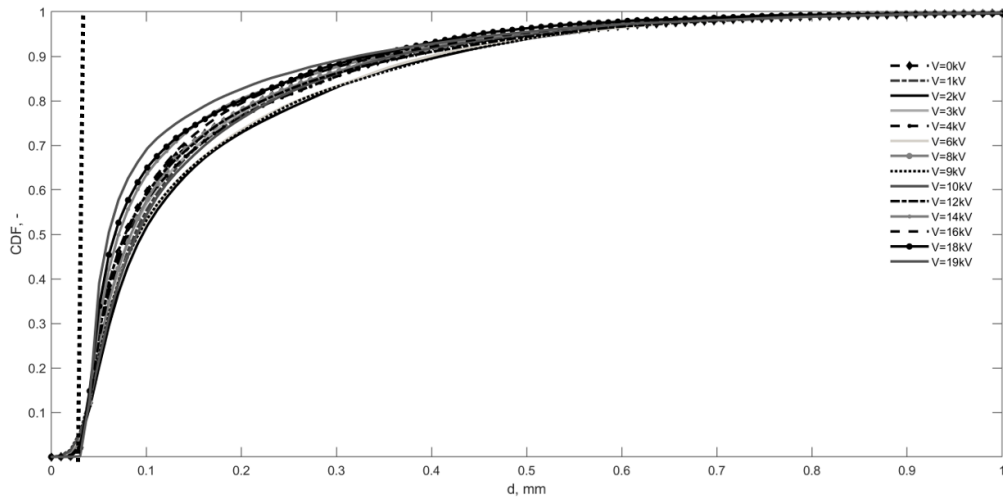


Figure 6-4- Cumulative Density Functions at different electric potentials for nozzle BD8 at $P=3\text{bar}$ and $Q_L=6.3\text{ L/min}$.

In Figure 6-4, it is reported the detection limit line of the high-speed camera used in this work and that is at $d=35\ \mu\text{m}$. In Figure 6-4, in CDFs curves the effect of electric potential comes out: as the electric potential increased, the curves shifted slightly towards smaller diameters.

If we would use the same experimental methodology used for the electrified water spray at low-flow rate [5], the percentile diameter, d_{50} , dependence on electric potential should be investigated, where the d_{50} represents the diameter at which corresponds the 50% of total distribution. It can be seen in Figure 6-3 that the reduction of d_{50} with potential is quite narrow. It decreased from 80 to 60 μm . It was mainly due to the fact that all curves were cut at $d=34\ \mu\text{m}$ and as consequence the shape of CDFs at small diameters is affected by an error.

To relate the electrification process with the atomization mechanism, the percental diameter d_{70} was considered because it covered a wider range of diameters. Figure 6-5 is the d_{70} percentile versus the electric potential.

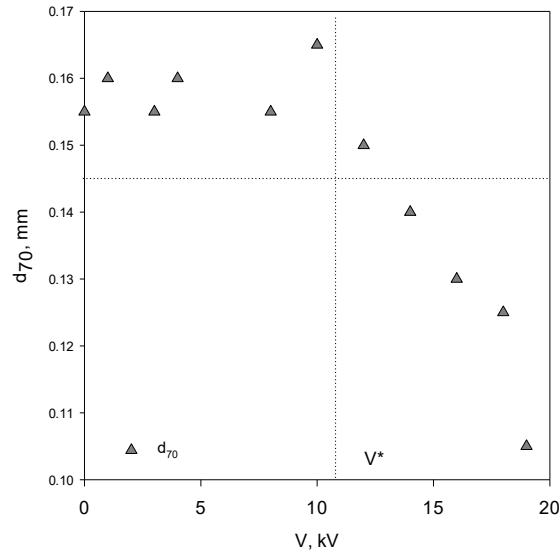


Figure 6-5- Diameter d_{70} versus electric potential for nozzle BD8 at $P=3\text{bar}$

The d_{70} oscillated around a value of 0.155 mm at electric voltages ranging from 0 kV and a certain value that we define V^* . As the electric potential reached V^* and became higher, the d_{70} reduced significantly and became 0.102 mm at $V=19$ kV.

Considering that this trend is the result of a combine process that is the electrified atomization mechanism, in Figure 6-6 the diameter d_{70} is plotted on same diagram with the electric current carried by water droplets. The droplets electric current, I_{drop} , was measured in a previous study [Chapter 3].

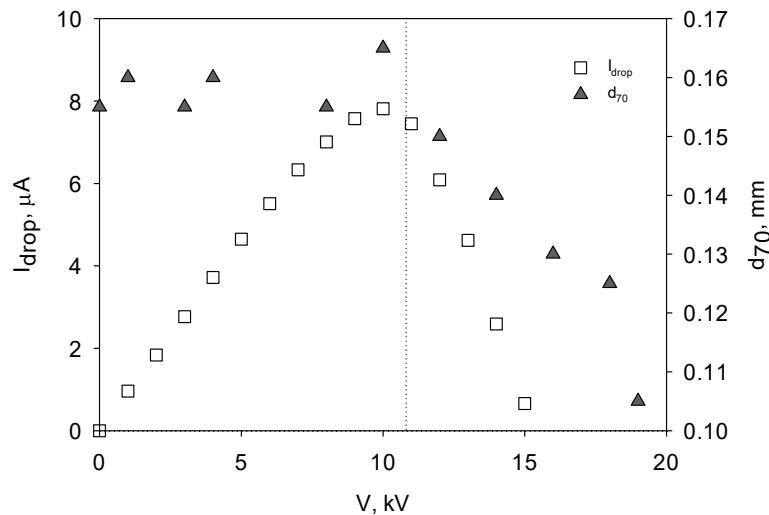


Figure 6-6 Droplets electric current, I_{drop} , and diameter d_{70} at different electric potentials for nozzle BD8 at $P=3$ bar.

The droplets electric current has a non-monotonic trend with applied potential: it increases linearly with voltage till the point V_{opt} at which the electric current has the highest value, then it reduces more and more and becomes almost zero at a point called *minimum potential* or V_{min} . The diameter d_{70} has its

highest reduction at voltages around V_{min} , as it is showed in Figure 6-5. This trend was observed in all operative conditions and for all the tested nozzle. In Table 6- 1, the d_{70} at $V=0kV$ and at $V=V_{min}$, the percentage of reduction Δd_{70} are listed.

Table 6-1- 70th percentile at $V=0kV$ and $V=V_{min}$, percentage of reduction for all tested nozzles. *Discharge occurring during the test

Nozzle	P, bar	Q_L , L/min	$d_{70 0kV}$, mm	$d_{70 V_{min}}$, mm	V_{min} , kV	Δd_{70} , %
BD5	2	3.2	0.171	0.15	19.5	12
BD5	3	3.9	0.19	0.171	19.5	10
BD5	3.5	4.2	0.165	0.13	19	21
BD5	4	4.6	0.162	0.115	16	29
BD8	1.5	4.6	0.176	0.148	16.5	16
BD8	2	5.2	0.144	0.123	19	15
BD8	3	6.3	0.145	0.104	19.5	26
BD10	1	4.6	0.269	0.232*	14*	14
BD10	2	6.4	0.227	0.19	17.5	16

The reduction of 70th percentile is on average around 10-20% and it increases with the liquid flow rate. The results showed in Figure 6-7 and Table 6-1 demonstrate that there is a correlation between the electric current measurements, which are index of how much the electric field is charging the liquid jet, and the atomization mechanism. To understand it, the ratio between the electrical and surface tension stresses was estimated. The ratio is expressed as in Eq. (6.6) that is here reported:

$$R = \frac{\pi \cdot I_{cone}^2 \cdot \langle a^2 \rangle \cdot L_b \cdot \cos\left(\frac{\theta}{2}\right)}{36 \cdot \epsilon_0 \cdot \gamma \cdot Q_L^2} \quad (6.6)$$

Figure 6-7 plots both the ratio R and the droplet electric current, I_{drop} , as function of electric potential for the nozzle BD8 at P=3 bar.

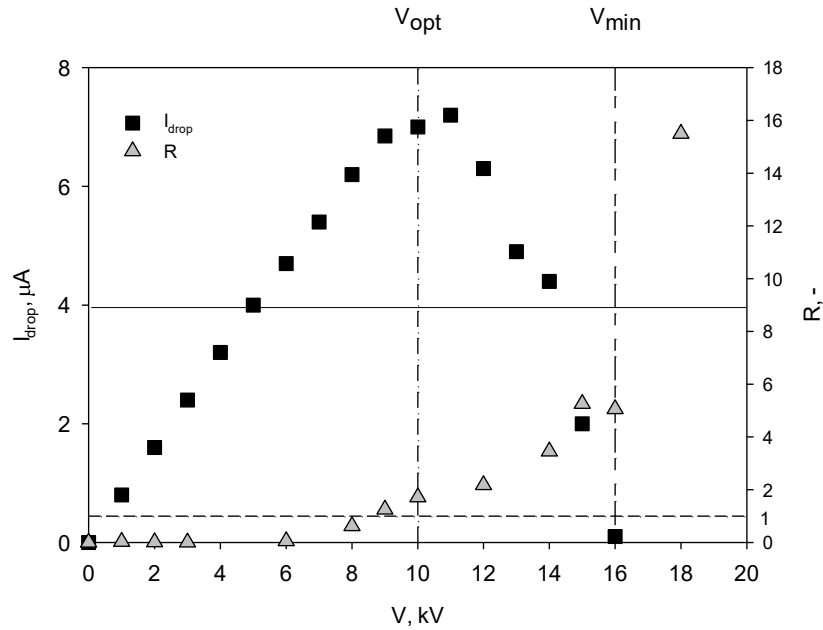


Figure 6-7- Ratio R and I_{drop} versus the electric potential for the nozzle BD8 at $P=3$ bar.

For an uncharged spray, the atomization mechanism is controlled by liquid inertia and its surface tension. Once an external electric field is applied, as in the induction charging used in this work, another force is acting on liquid jet destabilizing its equilibrium. In the ratio R, the surface tension stress is constant with the electric potential; the electrical stress, instead, represents how much the presence of an electric field influences the atomization mechanism of a liquid jet and changes it. What is expected is that the electrical stress added by polarization of liquid jet increases with the electric potential till reaching a new equilibrium of the system when by $R=1$. Above this level, the electrical stress is overcoming the surface tension stress. It happens at an electric voltage than is the point of maximum current carried by droplet, V_{opt} , with an error of ± 1 kV. For $V > V_{opt}$, the ratio R continues to increase, while the electric current starts to decrease. The ratio rises swiftly from 5.02 to 15.49 as soon as the electric current approaches at its minimum value at V_{min} .

In light of these observations, in Figure 6-8 the diameter d_{70} , the electric current I_{drop} and the ratio R are compared.

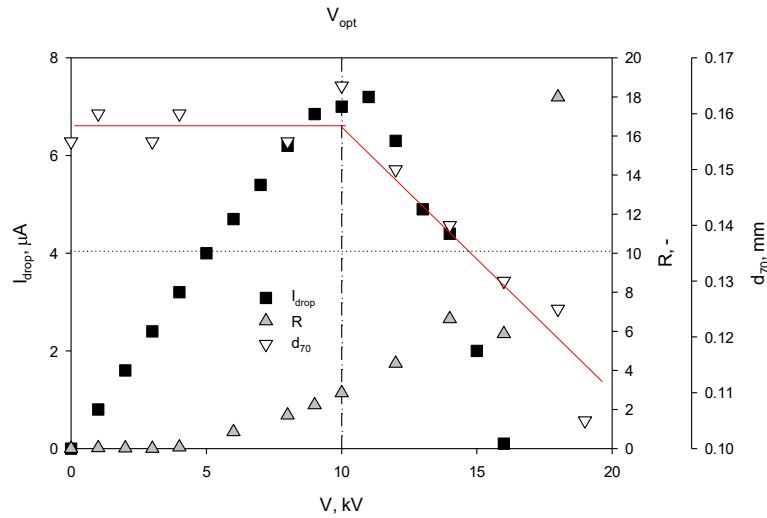


Figure 6-8. I_{drop} , R and d_{70} versus the electric potential for nozzle BD8 at $P=3$ bar

As soon as the electric voltage becomes larger than V_{opt} , the ratio R is larger than 1, and the droplets d_{70} starts to decrease and reaches the lowest value at $V > V_{min}$. The trend of d_{70} with the electric voltage is clarified by the two red lines in Figure 7-8.

Figure 6-9 is indicating that the points $V=V_{opt}$ and $V=V_{min}$ represent a change in the electrification process of the liquid jet and the diagram could be divided in three zones. For electric potentials between 0 kV and V_{opt} , the electrification mechanism is purely inductive. For V ranging between V_{opt} and V_{min} , the droplets electric current decreases, as the diameter, while the electrical stress increases becoming larger than 1. This suggests the occurrence of a new charging process.

Thanks to the experimental observations made on the water electro spray discussed in Chapter 5, the plausible explanation of results shown in Figure 7-8 is the occurrence of corona discharges on the liquid cone, which is competitive with the induction charging process.

6.4 Summary

In this study, the lab-scale electrified water spray was used to study the influence of the electric field on secondary atomization mechanism. Three hydraulic hollow cone sprays were tested by varying the liquid flow rate between 3.9 and 7 L/min, while the electric potential ranged from 0 to 20 kV.

From the experimental results, the droplets' size distributions were estimated. It was observed that the CDFs shifted smoothly towards smaller diameters as the electric potential increased. The percentile diameter d_{70} was chosen as target diameter to quantify the effect of the electric field on droplets' size.

The d_{70} oscillated around its value at $V=0$ kV with an error of 2-3%, related to imaging analysis process, until the electric potential V^* after which it started to reduce. The curve $d_{70}-V$ was compared with the measurements of droplets electric current, I_{drop} , at different voltages, in the same experimental

conditions. It came out that the potential V^* was the same potential at which the electrical current reached its maximum value, V_{opt} , with an error of ± 1 kV. It was verified for all tested nozzle.

To understand it, the ratio between the electrical and surface tension stresses was estimated. This ratio represents how the electrical stress added by polarization of liquid jet added a perturbation on liquid jet, and it appears as a continuous function of the applied electric potential. When the ratio R becomes larger than one, the electrical stress overcome the surface tension stress. This condition held close to V_{opt} and was accompanied by the assessment of stable conditions for the break-up length and the spray angle (Chapter 4) and the progressive reduction of droplet diameters, as shown, for example, in Figure 7-6 for the d_{70} diameter. Although further evidences are needed to support the development of a definite theory, the former indications on nozzle sprays in whipping regimes let us envisage that the experimental evidences can be explained considering the insurgence of corona discharges on liquid jet.

6.5 References

- [1] A. Krupa, A. Jaworek, A. T. Sobczyk, A. Marchewicz, M. Szudyga, and T. Antes, "Charged spray generation for gas cleaning applications," *J. Electrostat.*, vol. 71, no. 3, pp. 260–264, 2013.
- [2] L. Manna, F. Di Natale, C. Carotenuto, and A. Lancia, "Electrified water sprays generation for gas pollutants emission control," *CET*, vol. 52, no. 2003, pp. 421–427, 2016.
- [3] F. Di Natale *et al.*, "Water electrified sprays for emission control in energy production processes," *Int. J. Heat Technol.*, vol. 34, no. Special Issue 2, 2016.
- [4] L. Manna, C. Carotenuto, R. Nigro, A. Lancia, and F. Di Natale, "Primary atomization of electrified water sprays," *Can. J. Chem. Eng.*, vol. 95, no. 9, 2017.
- [5] L. Manna, F. Kariithi, F. Di Natale, A. Lancia, J. M. C. Marijnissen, and L. L. F. Agostinho, "Electrohydrodynamic atomization of water in the simple jet mode with whipping breakup," *Submiss.*, 2018.
- [6] L. Manna, F. Di Natale, C. Carotenuto, and A. Lancia, "Electrified water sprays generation for gas pollutants emission control," *Chem. Eng. Trans.*, vol. 52, 2016.
- [7] L. Manna, F. Di Natale, S. Caserta, and A. Lancia, "Induction Charging of Water Sprays," in *ILASS*, 2016, no. September, pp. 4–7.
- [8] L. D'Addio, F. Di Natale, C. Carotenuto, W. Balachandran, and A. Lancia, "A lab-scale system to study submicron particles removal in wet electrostatic scrubbers," *Chem. Eng. Sci.*, vol. 97, pp. 176–185, Jun. 2013.
- [9] F. Di Natale *et al.*, "Capture of fine and ultrafine particles in a wet electrostatic scrubber," *J.*

- Environ. Chem. Eng.*, vol. 3, no. 1, pp. 349–356, 2015.
- [10] W. Balachandran, A. Krupa, W. Machowski, and A. Jaworek, “Smoke precipitation by charged water aerosol,” *J. Electrostat.*, vol. 51–52, no. 1–4, pp. 193–199, 2001.
- [11] W. Balachandran, A. Jaworek, A. Krupa, J. Kulon, and M. Lackowski, “Efficiency of smoke removal by charged water droplets,” *J. Electrostat.*, vol. 58, no. 3–4, pp. 209–220, 2003.
- [12] A. Jaworek and A. Krupa, “Classification of the Modes of Ehd Spraying,” *J. Aerosol Sci.*, vol. 30, no. 7, pp. 873–893, 1999.
- [13] J. M. Grace and J. C. M. Marijnissen, “A review of liquid atomization by electrical means,” *J. Aerosol Sci.*, vol. 25, no. 6, pp. 1005–1019, 1994.
- [14] A. Jaworek and A. T. Sobczyk, “Electrospraying route to nanotechnology: An overview,” *J. Electrostat.*, vol. 66, no. 3–4, pp. 197–219, 2008.
- [15] G. N. Laryea and S. Y. No, “Spray angle and breakup length of charge-injected electrostatic pressure-swirl nozzle,” *J. Electrostat.*, vol. 60, no. 1, pp. 37–47, 2004.
- [16] J. A. Cross, J. C. W. Fowler, and G. Fu, “Electrostatic Enhancement of water sprays for coal dust suppression,” Sydney, Australia, 2003.
- [17] G. Artana, L. C. Bassani, and R. Scaricabarozzi, “Specific charge of induction electrified sprays,” *J. Electrostat.*, vol. 29, no. 2, pp. 127–145, 1993.
- [18] J. A. Marchant, A. J. J. Dix, and J. M. M. Wilson, “The electrostatic charging of spray produced by hydraulic nozzles. Part II. Measurements,” *J. Agric. Eng. Res.*, vol. 31, no. 4, pp. 345–360, 1985.
- [19] J. A. Marchant, A. J. Dix, and J. M. Wilson, “The electrostatic charging of spray produced by hydraulic nozzles: Part I. Theoretical Analysis,” *J. Agric. Eng. Res.*, vol. 31, no. 4, pp. 329–344, 1985.
- [20] N. Dombrowski and W. R. Johns, “The aerodynamic instability and disintegration of viscous liquid sheets,” *Chem. Eng. Sci.*, vol. 18, no. 3, pp. 203–214, 1963.
- [21] C. J. Clark and N. Dombrowski, “Aerodynamic Instability and Disintegration of Inviscid Liquid Sheets,” *Proc. Roy. Soc. Lond. A*, vol. 329, p. 467, 1972.
- [22] P. K. Senecal, D. P. Schmidt, I. Nouar, C. J. Rutland, R. D. Reitz, and M. L. Corradini, “Modeling high-speed viscous liquid sheet atomization,” *Int. J. Multiph. Flow*, vol. 25, no. 6–7, pp. 1073–1097, 1999.
- [23] N. Ashgriz, *Handbook of atomization and sprays: theory and applications*, vol. 1. 2011.

- [24] Levebvre, *Atomization and Sprays*. .
- [25] L. Manna, C. Carotenuto, R. Nigro, A. Lancia, and F. Di Natale, “Primary atomization of electrified water sprays,” *Can. J. Chem. Eng.*, vol. 95, no. 9, pp. 1781–1788, Sep. 2017.

Chapter 7. Conclusion

The present work had the purpose to study the influence of an electric field on the atomization mechanism of a liquid spray. Hydraulic hollow cone nozzles were tested at high-flow rate (\sim L/min). Our experimental findings suggested that the electric forces induced on the liquid sheet generated an increment of the wavy oscillations and deformed the sheet so to enlarge the spray angle. In light of the indications achieved with these experiments, we believed that a detailed electrohydrodynamic study was necessary. Indeed, we carried an experimental investigation on an electrified spray at low-flow rate (\sim mL/h) to better understand how the electric field influenced the liquid jet.

For both systems, the liquid was water and the electrification was obtained by induction charging: the liquid was pumped into a grounded nozzle and exposed to an external electric field generated by a toroidal counter-electrode connected to the high-voltage power supply.

The methodology was divided in two different experimental campaigns. The optical tests investigated the atomization mechanism to evaluate how the spray properties, as breakup length, spray angle and droplets' size distribution, were influenced by the applied electric field. The charging tests aimed to measure the electrical currents of droplets, nozzle and high-voltage power supply.

For the high-flow rate electrified spray, hydraulic hollow cone nozzles were tested. The liquid flow rate varied from 3 to 7 L/min and the electric potential from 0 up to 20 kV. The charging tests revealed that the electrical current carried by water droplets, I_{drop} , increased linearly with the electrical potential from 0 and V_{lin} , then it continued to increase with a lower slope until reaching the point of maximum current at V_{opt} . At electric potentials larger than V_{opt} , the electrical current started to decrease and at a voltage defined V_{min} , the current become almost zero. The droplets specific charge or Droplet Charge to Mass Ratio (D-CMR), which is the ratio between the current I_{drop} and the liquid flow rate, showed the same trend.

Considering that the electrification process was by induction, the electrical current measured on grounded nozzle, I_{nozzle} , was expected to be equal in module to droplets' current, and the electrical current emitted from the high voltage supply, I_{gen} , to be negligible. The expectations were verified at electric potentials between 0 and V_{opt} . As soon as the voltage become larger than V_{opt} , the currents I_{gen} and I_{nozzle} increased and become comparable. For $V < V_{\text{opt}}$, the induction charging model was used to describe data obtained from charging tests. It was found that the experimental data were well described by induction charging model and a corrective factor of 0.243 was necessary to have a perfect coincidence between them.

The optical tests confirmed the influence on the electric field on the atomization mechanism. Indeed, when the electric field was applied, the spray angle generally increased due to of the repulsion of the charged droplets while the breakup length reduced up to an asymptotic value L_{vs} . This effect severely

affect the charging efficiency of the spray and confirmed the observation of Laryea and No, in contrast with the results of Marchant et al.[21–24,26].

In terms of the droplets' size distributions, it was observed that the CDFs shifted smoothly towards smaller diameters as the electric potential increased. The percentile diameter d_{70} was chosen as target diameter to quantify the effect of the electric field on droplets' size.

The d_{70} oscillated around its value at $V=0$ kV with an error of 2-3%, related to imaging analysis process, until a potential V^* after which the d_{70} reduced significantly. The curve d_{70} - V was compared with the measurements of droplets electric current, I_{drop} , at different voltages, in the same experimental conditions. It came out that the potential V^* was the same potential at which the electrical current reached the maximum value, V_{opt} .

The experimental campaign on Electro-Hydro-Dynamic Atomization was made at liquid flow rate ranging from 450 to 1000 mL/h and electric potentials from 0 to 17 kV for three different nozzles. As the electrical potential was increased, the atomization mode changed and passed from the simple jet mode with varicose breakup to the simple jet mode with whipping breakup.

The optical tests showed that the droplets' size distributions were multi-modals with a predominant peak at a diameter similar to the nozzle outer one at low potentials. It shifted to about 0.05 mm when the electrospray mode was *the simple-jet mode with whipping breakup*. The droplets were much smaller than inner nozzle diameter and highly charged and deformed matching the needs of applications as electrified gas scrubbing.

The charging tests revealed that the electrical current slowly increased with the electric potential until the whipping instability took place on the liquid jet and at this condition the electric current rapidly increased.

The experimental evidences highlight that the electric stress acting on the liquid jet led to its stretching and to the whipping instability. This is the reason why we estimated the ratio R between the electric and surface tension stresses. The ratio showed the same trend of the electric current and, accordingly with previous experiments, it became larger than 0.3 ± 0.05 when the transition to the whipping breakup occurred. The ratio was larger than 1 when the whipping breakup mechanism become predominant.

The same ratio was calculated for the high-flow rate electrified spray. It was expected that the electrical stress caused by the polarization of the liquid jet added a perturbation on liquid jet and it increased with the electric potential till reaching a new equilibrium of the system ($R=1$). When the ratio R is larger than 1, it means that the electrical stress is overcoming the surface tension stress. The experiments showed that the ratio R increased smoothly with the electric potential until the point $R=1$. As soon as the ratio become larger than 1, it rose swiftly. R become larger than 1 at $V=V_{\text{opt}}$ with an error of ± 1 kV. It means that the electric potential $V=V_{\text{opt}}$ indicates a change in polarization process of the liquid jet.

We envisage that all the spray geometries observed for a given charging potential represented an equilibrium condition between the electric field effects, which tend to enlarge the spray and reduced the break up length, and the inertial forces, which acted to preserve its original shape. The explanation for this combined effect between the electrification and atomization process could be several. The former indications on low-flow rate sprays in whipping breakup let us envisage that the experimental evidences can be explained considering the insurgence of corona discharges on liquid jet. In fact, once the electric field approached a critical value, related to Townsend discharges, the energy provided by the HV supply is converted in ionic discharges and the actual forces exerted on the liquid sheet did not increase anymore, leading to the asymptotic values of L_{vs} and θ_{∞} . Indeed, it could justify the non-monotonic trend of droplets electrical current, the ratio $R > 1$ that influences the secondary atomization of liquid jet observed in the d_{70} reduction.

List of publications

- ❖ *“Electrified Water Sprays Generation for Gas Pollutants Emission Control”*- L.Manna, F. Di Natale, C.Carotenuto, A. Lancia, Chemical Engineering Transtaction, vol.52, 2016, pp. 421-426
- ❖ *“Water Electrified Sprays for Emission Control in Energy Production Processes”*, F. Di Natale, C. Carotenuto, L. Manna, L. D’Addio, A. Lancia, Internation Journal of Heat and Technology, vol. 34, 2016, pp-S597-S602
- ❖ *“Primary Atomization Of Electrified Water Sprays”* L.Manna, C. Carotenuto, R. Nigro, A. Lancia and F. Di Natale, Canadian Journal of Chemical Engineering, 2017, 95, pp. 1781-1788
- ❖ *“Capture of bacterial bioaerosol with a wet electrostatic scrubber”* F. Di Natale, L. Manna, F. La Motta, R. Colicchio, E. Scaglione, C. Pagliuca, P. Salvatore, Journal of Electrostatics vol. 93, 2018, pp-58-68
- ❖ *“Chemi-electro-hydrodynamic of sulphur dioxide absorption by electrified water drops”*- F. Di Natale, C. Carotenuto, L. Manna, A. Lancia, Chemical Engineering Transactions, vol. 69, 2018, pp- 685-690
- ❖ *“Secondary Atomization of Electrified Water Sprays”*- F. Di Natale, L. Manna, A. Lancia, 2018, (in submission)
- ❖ *“Electrohydrodynamic Atomization of water in the simple-jet mode with whipping breakup”*, - L. Manna, F. Kariithi, F. Di Natale, A. Lancia, J.C.M. Marijnissen, L.L.F. Agostinho (in submission)

Conference Proceedings

- ❖ *Wet Electrostatic Scrubber for Gas Pollutants Emission Control*”-M.Esposito, L.Manna, F. Di Natale. C.Carotenuto, A. Lancia- XXXIX Meeting of The Italian Section of The Combustion Institute 2016
- ❖ *“Influence of Electric Field On Breakup Length Of Water Spray”*- L.Manna, F. Di Natale. C.Carotenuto, A. Lancia -Gricu 2016
- ❖ *“Induction Charging of Water Sprays”*- L.Manna, F. Di Natale. C.Carotenuto, S. Caserta, A. Lancia- ILASS 2016
- ❖ *“Electrohydrodynamic of Water in the Simple Jet Mode with Whipping Breakup”*, L. Manna, F. Kariithi, F. Di Natale, A. Lancia, J.C.M. Marijnissen, L.L.F. Agostinho, AT2018, Bilbao

